SAND REPORT
SAND2004-0151
Unlimited Release
Printed January 2004

2004 Research Briefs: Materials and Process Sciences Center

Michael J. Cieslak

Prepared by
Sandia National Laboratories
Albuquerque, New Mexico 87185 and Livermore, California 94550

Sandia is a multiprogram laboratory operated by Sandia Corporation,
a Lockheed Martin Company, for the United States Department of Energy's
National Nuclear Security Administration under Contract DE-AC04-94-AL85000.

Issued by Sandia National Laboratories, operated for the United States Department of Energy by Sandia Corporation.

Available to DOE and DOE contractors from
U.S. Department of Energy
Office of Scientific and Technical Information
P.O. Box 62
Oak Ridge, TN 37831

Telephone: (865)576-8401
Facsimile: (865)576-5728
E-Mail: reports@adonis.osti.gov
Online ordering: http://www.doe.gov/bridge

Available to the public from
U.S. Department of Commerce
National Technical Information Service
5285 Port Royal Rd
Springfield, VA 22161

Telephone: (800)553-6847
Facsimile: (703)605-6900
E-Mail: orders@ntis.fedworld.gov
Online order: http://www.ntis.gov/help/ordermethods.asp?loc=7-4-0#online

SAND2004-0151
Unlimited Release
Printed January 2004

2004 Research Briefs: Materials and Process Sciences Center

Michael J. Cieslak
Materials and Process Sciences Center
Sandia National Laboratories
P.O. Box 5800
Albuquerque, NM 87185-0887

Abstract

This report is the latest in a continuing series that highlights the recent technical accomplishments associated with the work being performed within the Materials and Process Sciences Center. Our research and development activities primarily address the materials-engineering needs of Sandia's Nuclear-Weapons (NW) program. In addition, we have significant efforts that support programs managed by the other laboratory business units. Our wide range of activities occurs within six thematic areas: Materials Aging and Reliability, Scientifically Engineered Materials, Materials Processing, Materials Characterization, Materials for Microsystems, and Materials Modeling and Simulation. We believe these highlights collectively demonstrate the importance that a strong materials-science base has on the ultimate success of the NW program and the overall DOE technology portfolio.

Acknowledgment

First, we want to gratefully acknowledge the importance of our many customers who not only sponsor our work, but also provide valuable guidance, feedback, and programmatic motivation. In addition, we acknowledge the substantial and significant contributions of our co-workers from within many other organizations at Sandia, from universities, and from industry.

Editors:
C. L. Porter
J. W. Braithwaite

Introductory Message from the Center Director

The core responsibility of the Materials and Process Sciences Center is to provide materials-engineering support to Sandia's Nuclear-Weapons (NW) program. As a foundational Science and Technology organization for the Laboratories, the Center also performs R&D activities that are sponsored by the other laboratory business areas (Energy & Infrastructure Assurance, Nonproliferation and Assessments, Military Technologies & Applications, and Homeland Security). Importantly, our primary product is a science-based *knowledge* of material properties and behavior and the processes to more effectively produce, transform, and analyze them. Accordingly, our sponsors engage us in a broad range of research, development, and applications activities.

This report is the latest in a continuing series that contain highlights of recent specific accomplishments. These briefs are organized into sections that involve the Center's core capabilities: three prime thematic areas (Materials Aging and Reliability, Scientifically Engineered Materials, Materials Processing), and two of our three crosscutting areas (Materials Characterization and Materials for Microsystems). The goal of the work in *Materials Aging and Reliability* is to understand the chemical and physical mechanisms that cause materials properties to change and then develop mechanistic-based models to predict how these changes affect component reliability. Activities in the *Scientifically Engineered Materials* area focus on developing new and replacement materials with desired specific properties or performance characteristics through an understanding of how materials properties depend on composition, microstructure, and manufacturing processes. Within the *Materials Processing theme,* the knowledge base needed to understand, characterize, model, and ultimately control the materials fabrication technologies that are critical to hardware production is generated. Success with all of these activities requires the availability of effective tools and techniques to characterize materials. Thus, the focus of the crosscutting Materials Characterization area is to develop and apply analytical techniques to detect and measure chemical and structural information about materials at various temporal and spatial scales, down to the nanoscale. Our directed work to support Sandia's emerging microsystem initiative involves aspects of the other three thematic areas, but focused on the specific challenges associated with the inherently small-length scale of these devices. The third crosscutting Center capability involves the mathematical modeling and computational simulation of materials behavior and fabrication processes. Specific modeling accomplishments are described within the context of the other five topical sections.

Consideration of this entire set of highlights in conjunction with the needs of the non-nuclear aspects of the NNSA's NW program provides a sense of the importance that a strong materials-science base has on the program's ultimate success. These briefs also demonstrate the connections between materials science and the breadth of the overall DOE technology portfolio.

We welcome your questions and comments on the work being performed in the Materials and Process Sciences Center. Contact information along with additional organizational and technical descriptions of what we do can be found by visiting our website at http://www.sandia.gov/materials/science.

TABLE OF CONTENTS

MATERIALS AGING

MATERIALS CHARACTERIZATION

TABLE OF CONTENTS

MATERIALS CHARACTERIZATION, cont.

MATERIALS FOR MICROSYSTEMS

MATERIALS SYNTHESIS

TABLE OF CONTENTS

MATERIALS SYNTHESIS, cont.

MATERIALS PROCESSING

TABLE OF CONTENTS

MATERIALS PROCESSING, cont.

Atmospheric Corrosion of Microelectronic Packaging: Importance of Manufacturing Quality

N. R. Sorensen, J. W. Braithwaite

Motivation: Atmospheric corrosion of the metallic features used to package microelectronic devices is a degradation mode that often must be considered when assessing the reliability of electrical circuits. Corrosion of the prime susceptible material, aluminum, requires two conditions: the presence of moisture, and a halide contaminant (typically chloride ion) that causes localized breakdown of the oxide film. Because of availability and cost, plastic-encapsulated microelectronic (PEM) devices are now being used in place of ceramic hermetic packages (CHP) in high consequence military hardware. Contrary to CHP devices, the environment at the surface of a PEM die may not remain dry over long periods of time due to the inherently high moisture permeability of the plastic encapsulant. In addition, because the devices are unpowered during long-term dormant storage, a typical drying event (ohmic heating during active use) does not occur. Thus, concern exists that corrosion may reduce the reliability of PEM devices.

Historically, two types of corrosion-related phenomena have been observed in field returns: Au wire/Al bondpad interfacial degradation and distributed Al track corrosion. Track corrosion typically correlates with moisture penetration through defects in the passivation layer (e.g. SiN). Bondpads have no passivation treatment and are susceptible to accelerated attack due to galvanic coupling with the Au wire.

Accomplishment: The goal is to understand the risks associated with using PEM devices in long-term dormant storage military applications. Corrosion mechanisms are being investigated at Sandia in conjunction with a fielded dormancy storage study run by the U.S. Army's Redstone Arsenal. One notable aspect of this work involves our observation of how the manufacturing process can affect on of the two corrosion criteria: contamination. In practice, contamination is typically introduced during the manufacturing or packaging process. Tests have shown that halide contamination must be present to initiate corrosion of the Al bondpads. Figure 1 shows that chloride ions cannot be forced through the plastic.

For the dormant storage test, two parts have been deployed (LM-124 voltage reference device and CD-4011 quad NAND gate) in Hellfire missile containers at 4 Army locations. Annual electrical testing disclosed that electrical failures had indeed occurred. As shown in Figure 2, the LM-124 failed due to trace corrosion (passivation layer was damaged during wirebonding). The CD4011 failures were the result of bondpad corrosion. For the CD4011, failure occurred primarily at a single location (shipboard storage), confirming the strong influence of external environment (humidity & temperature) on the corrosion process. In some of the failed devices, all of the bondpads were attacked, while in others only one or two of the bondpads exhibited evidence of corrosion.

Significance: Based on the laboratory studies and failure analysis of dormantly stored parts, our finding is that, if PEM devices are manufactured using best commercial practices, they are very robust and resistant to corrosion. However, the introduction of defects (surface contamination, delaminations, etc.), that can occur during manufacturing and/or packaging, can result in significantly reduced resistance to corrosion.

Contact: Rob Sorensen, Corrosion, Electrochemistry & Cleaning Dept., 1832
Phone: (505) 844-5558
Fax: (505) 844-5558
Email: nrsoren@sandia.gov

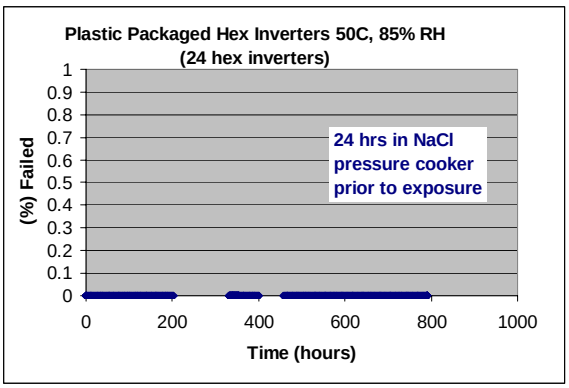

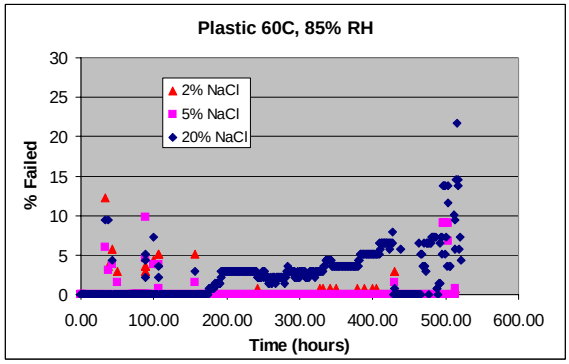

(a) (b)

Figure 1. Failure rate for PEM hex inverters. Undamaged parts were pressure cooked in NaCl in an attempt to force chloride through the plastic (a). For the parts represented in (b), physical defects were introduced, allowing the NaCl to contact the metallization features.

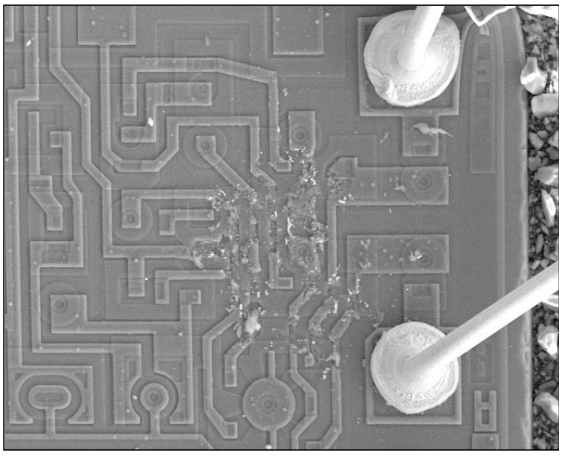

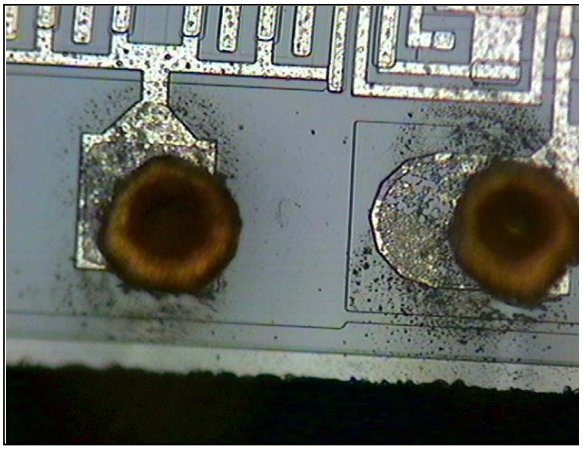

(a) (b)

Figure 2. SEM and optical images of corrosion of Al traces in the LM324 (a) and Al bondpads for the CD4011 (b) that failed during dormant storage.

Characterizing Atmospheric Corrosion Using High-Impedance Electrochemical Sensors

F.D. Wall

Motivation: Assessing the extent of metal corrosion under atmospheric conditions and predicting the effects on system-level performance requires the ability to accurately quantify metal oxidation rates. Traditional approaches typically rely on exposing metals to a highly aggressive environment followed by ex-situ examination. The pitfalls of this approach include (1) possibly altering the mechanism of corrosion due to the aggressive environment, (2) providing information that is more qualitative than quantitative, (3) lacking adequate sensitivity to instantaneous corrosion rates (e.g., the measurement represents the average behavior over the duration of the exposure). The goal of this project is to develop an in-situ, quantitative and highly sensitive technique for assessing atmospheric corrosion rates under low humidity environments which represent actual storage and service environments. The approach being taken is to develop high-impedance sensors that place co-planar materials in close physical proximity such that traditional electrochemical measurements can be used to directly measure metal oxidation and to characterize the adsorbed electrolyte.

Accomplishment: Dissimilar metal electrodes such as aluminum-copper galvanic couples have proven to be extremely sensitive to corrosion even at low humidity and low contaminant concentration. Figure 1 demonstrates the ability to measure corrosion rate (galvanic current) at low humidity and with sub-pA resolution. The shaded region on the plot represents the range of humidity and current resolution typically reported in the literature for these types of measurements. Our ability to make more sensitive measurements stems from micron-level control over electrode separation and state-of-the-art electrochemical instrumentation.

The galvanic corrosion sensors are also extremely sensitive to localized degradation (e.g., pitting attack) as seen in Figure 2. The electrochemical transients shown correspond to nanoscale processes that are not discernable using other analytical tools and would go undetected in a typical atmospheric exposure study.

It is also possible to extract information about the resistivity of the adsorbed water layer by carefully designing and constructing the sense electrodes to have high impedance across a wide frequency range. A gold thin film electrode was constructed in such a manner and used to characterize the electrolyte resistivity (R_E) and corrosion resistance (R_P) as a function of humidity level (Figure 3). The RE parameter is a function of adsorbed electrolyte thickness and levels of ionic contamination, both critical to understanding mechanisms of atmospheric corrosion.

Significance: The techniques developed in this work will enable collection of kinetic data that is critical to continuum level modeling of degradation processes in microelectronics under dormant storage conditions. The same techniques are currently being used to evaluate a new class of electrodeposited (LIGA) materials under atmospheric conditions. Finally, this approach is applicable to addressing material response under deliquescent salts, an environment anticipated in the Yucca mountain nuclear waste storage facility.

Contact: Doug Wall, Corrosion, Electrochemistry & Cleaning Dept., 1832
Phone: (505) 844-6904
Fax: (505) 844-7910
Email: fdwall@sandia.gov

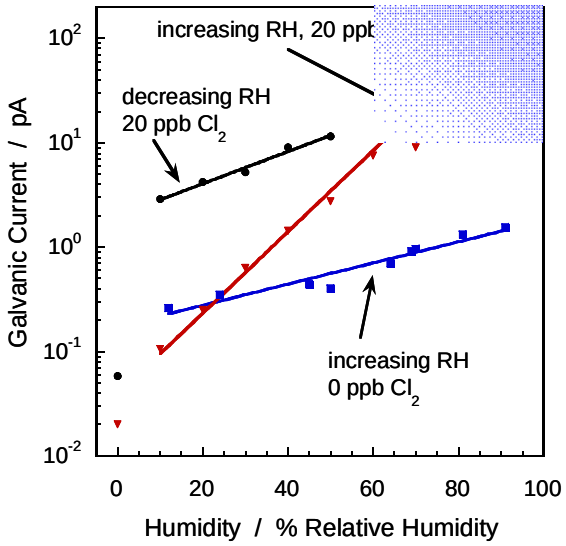

Figure 1. Corrosion rate (galvanic current) of an aluminum-copper couple as a function of relative humidity and contaminant concentration. The measurement is sensitive to the presence of $Cl_{2(g)}$ and to the manner in which the experiment was performed: increasing RH which is sensitive to adsorption rates vs. decreasing RH which is sensitive to desorption rates. The shaded region shows the range of measurements typically reported in the literature.

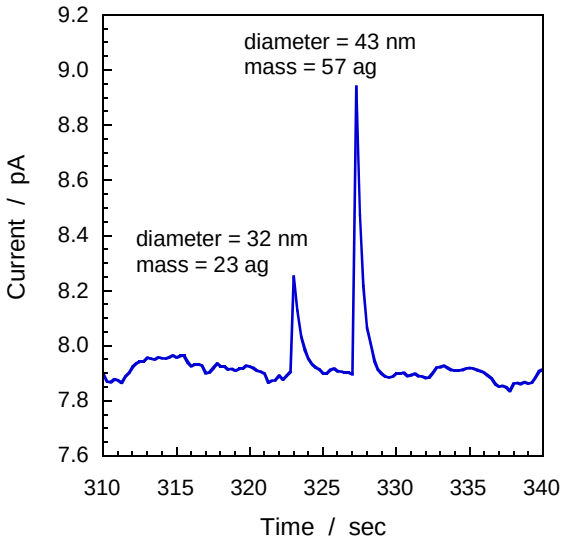

Figure 2. Corrosion behavior for an aluminum-copper galvanic couple exposed to 85%RH and 20 ppb $Cl_{2(g)}$. The current transients correspond to break-down and repassivation on the aluminum electrode. The magnitude of the first transient is on the order of 300 fA, demonstrating the high level of sensitivity achieved using these techniques.

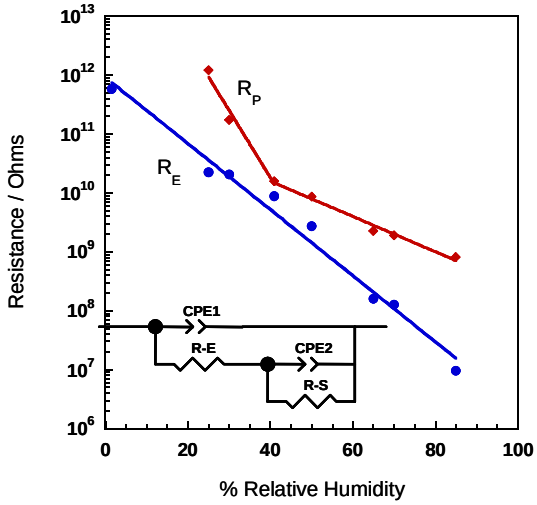

Figure 3. Electrolyte resistance (R_E) and polarization resistance (R_P) values extracted from raw impedance data using the electrochemical model shown as an inset. The raw data were collected using a high-impedance thin film gold electrode. These data demonstrate the ability to resolve both material behavior and environmental characteristics from a single experiment.

Corrosion in Strategic Petroleum Reserve Oil Coolers

D.G. Enos, B.L. Levin, T.E. Hinkebein

Motivation: At each Strategic Petroleum Reserve site, oil is stored in massive underground storage caverns mined into salt domes. As it is removed, the oil is cooled via tube-sheet heat exchangers prior to being placed in above ground storage tanks for distribution (Figure 1). The oil passes through the shell of the exchangers and is cooled by untreated site water flowing through the tubes. The current heat exchanger tube bundles, constructed of plain carbon steel, have exhibited a higher than expected failure rate due to corrosion and fouling. Preliminary research and analyses were conducted to determine a course of action that would halt this corrosion and fouling, ensuring that a full-rate drawdown (i.e., constant, maximum output for 180 days) could be performed.

Two potential solutions were identified, including; (1) the use of an alternative material for the heat exchanger tube bundles, and (2) the implementation of a water treatment system. The prime alternative material is SeaCure®, a super-ferritic stainless steel designed for high chloride environments. The water treatment solution consists of two chemicals which are added directly to the cooling water prior to its entry into the oil cooler - a phosphate-based corrosion inhibitor and a polymeric deposit control agent.

Accomplishment: A laboratory scale flow-loop system was designed and constructed. This system allows the simulation of both the thermal and hydrodynamic environment within the oil coolers, while allowing the solution chemistry, corrosion behavior, and thermal performance of the materials within the heat exchanger to be monitored (shown schematically in Figure 2). The system consists of 14 individual flow loops. Two of the loops serve to control the shell side conditions (allowing simultaneous simulation of the hot and cold side of the oil coolers), while the remaining 12 permit the cooling water chemistries to be evaluated. Each of these 12 loops expose 3 to 6 tube segments to the cooling water. Solution chemistry is controlled and monitored in the stabilization tank for each flow loop. Electrochemical sensors employing the linear polarization technique were inserted in each of the 12 chemistry loops, allowing the corrosion performance of the tube sections to be monitored.

Exposure to the test solutions resulted in significant pitting, wall recession, and corrosion product buildup within all of the carbon steel tubes (Figure 3). The degree of attack was such that a carbon steel system will be unable to contain the range of internal pressures associated with a full-rate drawdown. The SeaCure®, however, was not significantly affected. The reduction in heat transfer efficiency and restriction of fluid flow were determined for each system. Reductions of up to 40% in flow rate and over 50% in thermal performance were calculated for carbon steel loops containing untreated water, based upon the data for a 60 day exposure. Similar, though slightly less severe, reductions in heat transfer and flow rate were obtained for loops which contained treated water.

Significance: This study verified field observations which suggested that the existing oil coolers would not survive a full-rate drawdown. Furthermore, this study established the inappropriateness of a water treatment solution and demonstrated that the use of an intrinsically resistant material is the most effective solution to this particular corrosion and fouling problem.

Contact: David Enos, Corrosion, Electrochemistry & Cleaning Dept., 1832
Phone: (505) 844-2071
Fax: (505) 844-7910
Email: dgenos@sandia.gov

Figure 1. Oil coolers located at each SPR site

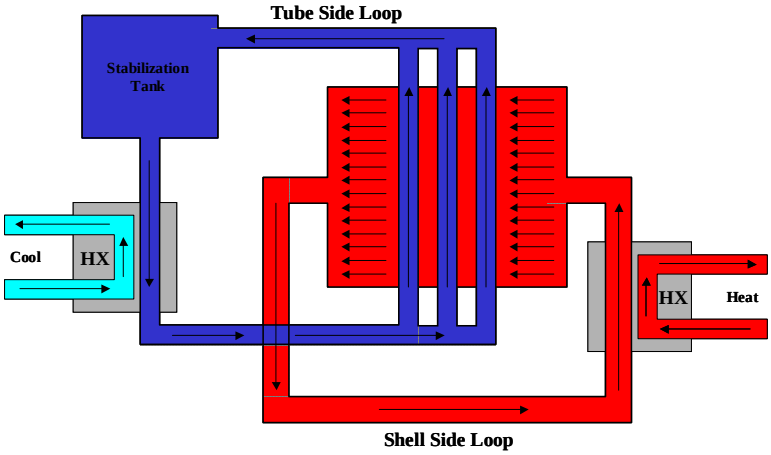

Figure 2. Schematic representation of flow loop system (only one of each type of loop is shown)

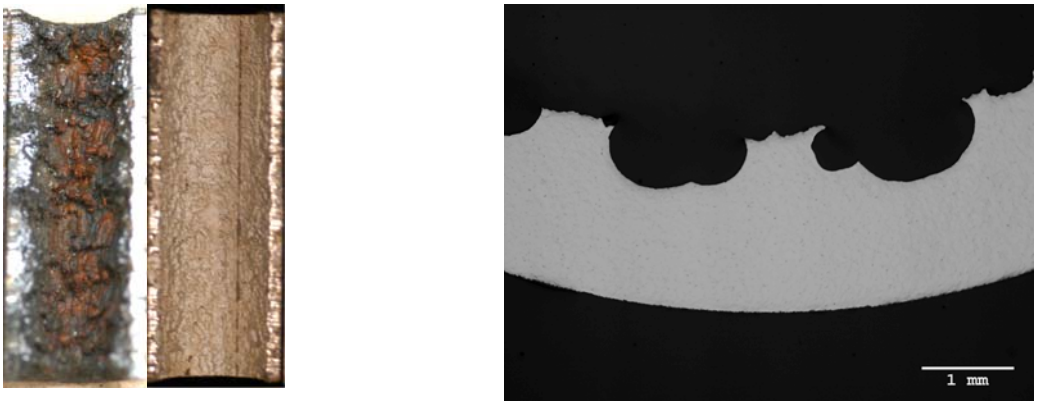

(a) (b)

Figure 3. Corroded tube wall before and after removing corrosion product, illustrating the extent of corrosion and fouling. (a) Cross section of a corroded tube section illustrating the depth of localized attack which was observed. (b)

Electrochemically Induced Nanoscale Void Nucleation and Growth at the Aluminum/Oxide Interface

K.R. Zavadil, P.G. Kotula, J.A. Ohlhausen

Motivation: The leading models for localized corrosion (pitting) of aluminum invoke the presence and specific roles of nanoscale voids at the metal/oxide interface. To date, no direct observation of or measurements have been made on these nanostructures, and their presence has only been inferred based on the eventual appearance of microscopic features. Our goal in this work is to identify if nanoscale voids are a predominant structural feature in the passive oxide and to study whether they play a deterministic role in pit initiation.

Accomplishment: Our team is the first to experimentally validate that nanometer-sized voids do exist within the passive oxide on aluminum under pre-pitting electrochemical conditions. A combination of electrochemical, SEM and TEM techniques show that these voids are one of several dominant nanostructural features that evolve in the oxide during electrochemical exposure prior to pit initiation. These voids nucleate at and grow from the Al/oxide interface, as shown in the transmission electron micrograph of Figure 1. Voids have an oblate hemispherical shape and do not appear to penetrate into the Al. We find that these voids are generalized to both bulk Al and Al thin films capped with both dry and solution-derived oxides.

We have completed void-growth kinetic studies. We find that void growth correlates with the quantity of passive charge density generated with polarization (Fig. 2a). Anodic polarization produces a continuous process of void nucleation and growth up to the point of pit initiation (Fig. 2b). We find that Cl^-, an aggressive pitting agent, is not necessary for void formation and does not incorporate within the voids or the oxide. Comparison of the pitting potential as a function of void density shows that an increased density does not influence pitting (Fig. 3).

Our results show that nano-voids are a predominant structural feature in the passive oxide but their characteristics do not match required elements of the leading pit initiation models. Constraint of the voids to the oxide eliminates the possibility that they represent the chloride-filled precursor sites proposed necessary for pit initiation in the Electrokinetic Model. The occurrence of vertical growth in these voids argues against a Point Defect Model-based view of initiation of 2-dimensional void formation, oxide detachment, and oxide thinning. Finally, we have demonstrated that the voids are not sufficient alone to induce stable pitting in Al, arguing that the eventual rupture of the oxide is not the sole event that dictates localized corrosion.

Significance: We have defined a predominant nanostructural feature proposed to be the key constituent of the two leading models that attempt to describe pit initiation. Our work is providing new knowledge to aid in the refinement of these corrosion stability models. The resulting enhanced understanding we provide will allow the corrosion community to identify the exact ways in which a passive oxide is deterministic toward localized corrosion.

Contact: Kevin Zavadil, Corrosion, Electrochemistry & Cleaning Dept., 1832
Phone: (505) 845-8442
Fax: (505) 844-7910
Email: krzavad@sandia.gov

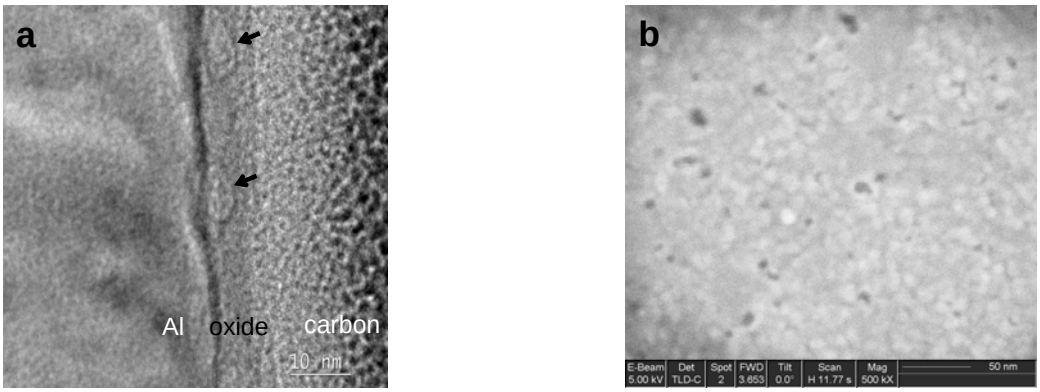

Figure 1. a) Cross-section TEM image of the passive oxide on Al(110) after polarization to -518 mV (vs. SCE) producing 4.2 mC•cm^{-2} of passive charge density (arrows indicate locations of voids) and b) SEM image of an Al thin film after polarization to -305 mV (vs. SCE) producing 2.5 mC•cm^{-2} of passive charge density (dark spots correspond to voids)

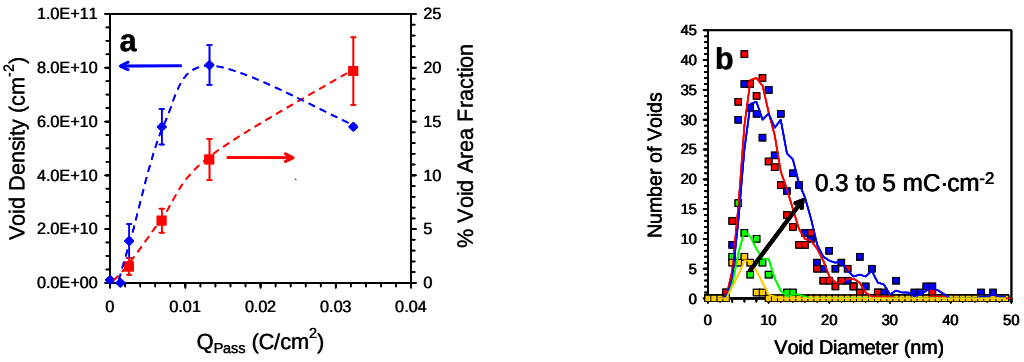

Figure 2. a) Variation in void density (blue) and area fraction (red) with passive charge density and b) the distribution in void size as a function of passive charge density showing that void nucleation and growth are continuous processes with anodic polarization.

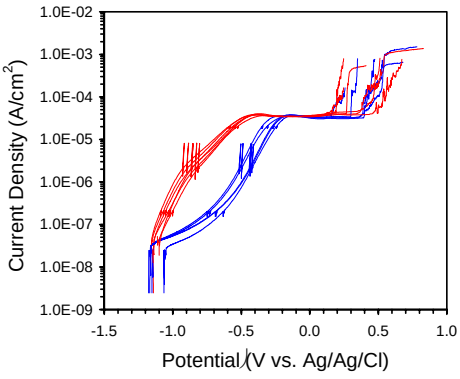

Figure 3. Variation in stable pitting susceptibility with rapid anodic polarization for two sets of samples: red – no pre-existing voids present, and blue – a pre-existing void density of 7x10^{10} cm^{-2}. The sudden increase in current density above the 40 µA•cm^{-2} plateau signals stable pitting.

Characterization, Performance and Optimization of PVDF as Piezo-electric Films for Adaptive Optics Applications

M. Celina, T. R. Dargaville, R. A. Assink. J. W. Martin, R. L. Clough

Motivation: Novel large-aperture adaptive optics systems providing improved sensitivity and ground resolution for future space-based remote sensing systems require thin piezoelectric polymer films based on polyvinylidene fluoride (PVDF). Key challenges are development of charge deposition control feedback loops and understanding how PVDF materials will perform or change their characteristics when exposed to vacuum UV irradiation, thermal cycling, atomic oxygen and other environmental factors in low earth orbit space environments. Materials performance will depend on primary polymer properties (polymer manufacturer), thermal and processing history (film producer), and molecular orientation, morphology and poling technologies (piezoelectric optimization). There is currently no commercial material available that is optimized for the intended application. We are investigating the various features of PVDF copolymers and the accelerated degradation of these polymers to understand the fundamental dependence of piezo properties on molecular structure, morphology and damage accumulation in radiation and temperature environments.

Accomplishment: An extensive range of PVDF copolymers, manufactured films and piezo sensors has been obtained, their chemical and physical properties characterized (Figure 1), and their sensitivity to γ-radiation evaluated. Initial studies on piezo phase changes and detailed chemical/morphology analysis using X-ray diffraction and nuclear magnetic resonance have been conducted providing interesting results by showing temperature dependent piezo phase conditions (Figure 2). All PVDF property data have been correlated and assessed to develop the most sensitive approaches to monitor the aging of PVDF. Access to a NASA materials selector database in space environments has been granted and will allow for better prediction of damage variables under different orbital conditions. We have used the advanced equipment of a piezo film manufacturer and measured fundamental piezo d_{33} characteristics. Initial data on the d_{33} piezoelectric coefficients (a measure of the change in polarization of the polymer in the thickness direction) for a series of commercially poled PVDF homopolymers and a TrFE copolymer aged using radiation, thermal treatment or a combination of the two are intriguing. When samples were annealed at elevated temperatures (>80°C) the depolarization process was found to be very rapid (<4 hours), after which, the d_{33} coefficients remained constant for months at elevated temperatures. Surprisingly, the TrFE copolymer had higher retention of the d_{33} coefficient compared with the homopolymers, completely unexpected when considering that the TrFE copolymer has a Curie temperature some 50°C lower than the homopolymers. Electron beam irradiation of the homopolymers and TrFE copolymer resulted in only a small decrease in the d_{33} coefficients. After thermal annealing of the irradiated samples there was slight but consistent improvement in d_{33} retention. This result is consistent with crosslinking of the amorphous regions and hindered depolarization of the crystallites.

Significance: These fundamental studies represent a sound foundation to select a suitable material and provide feedback on expected long-term performance criteria. The large variability and complexity in a compromise of polymer chemistry/physical property/piezo-performance has been demonstrated and will be used to develop material optimization strategies.

Contact: Mat Celina, Organic Materials Dept., 1811
Phone: (505) 845-3551
Fax: (505) 844-9781
Email: mccelin@sandia.gov

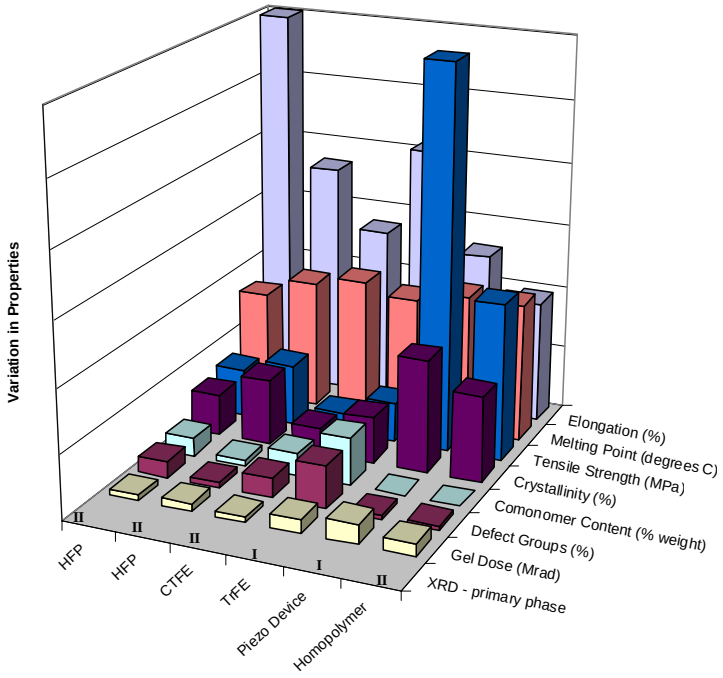

Figure 1. Property variation in a range of PVDF polymers

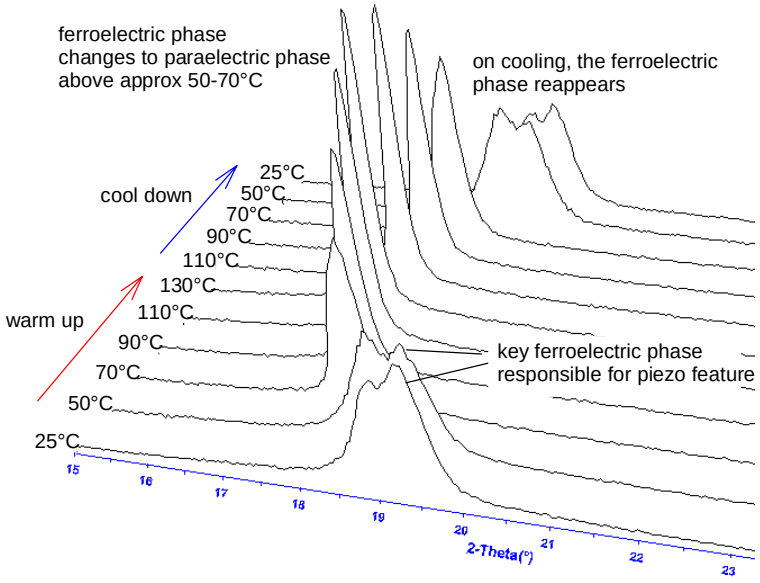

Figure 2. Temperature dependent phase changes in PVDF copolymer (50/50% trifluoroethylene)

Electrical Breakdown of GMB-Filled Epoxy in a Radiation Environment

R. A. Anderson, J. L. Schroeder

Motivation: Glass-microballoon (GMB) filled epoxy is a lightweight, mechanically compliant composite dielectric material that is used for encapsulating Sandia high-voltage components to protect against failure from electrical breakdown. This encapsulant can withstand surprisingly high pulsed electric fields, in light of the fact that nearly half of its volume is microballoon voids. However, ionizing radiation that is synchronized with the electrical stress triggers gas discharges in the voids and lowers the breakdown strength. Because a radiation-hard substitute is not currently available for GMB-filled epoxy, the ability to make quantitative predictions of electrical breakdown in a radiation environment is of high importance.

Accomplishment: Our existing non-radiation, statistics-based predictive model of electrical breakdown in GMB-filled epoxy has been reevaluated by using data obtained with synchronized pulsed electrical stress and ionizing radiation.

This investigation involved four different tasks: (1) Radiation-induced void polarization characteristics were extracted from test data at electrical stress levels below breakdown. This information is needed for calculating the electric fields near sharp geometrical features, where spatial gradients in void polarization (see Fig. 1) can give rise to substantial electric field screening. (2) Model parameters were derived from test results involving electrode geometries that did not produce strong field concentration. (3) Rectangular-corner electrodes (having tips as shown in Fig. 2), were fabricated. These represented rectangular geometrical features often found in actual components. The field distribution near these electrodes was computed and was found to be approximately similar to the field distribution near geometrically simpler conical-tip electrodes. (4) Validation tests were performed with both types (rectangular and conical) of sharp-tipped electrodes, and comparable breakdown voltages were obtained with either electrode type.

Our radiation-environment breakdown model was found to be consistent with experimental results when the encapsulant electric field is roughly uniform, but it predicted breakdown voltages substantially below experimental results in the case of sharply pointed, field-enhancing electrodes. This discrepancy has revealed issues arising from the very brief, 20-ns, radiation pulse that is available for our tests, and these issues could be resolved by using longer radiation pulses. A radiation facility with this capability may become available in the near future.

An alternative method for predicting encapsulant breakdown is also being pursued. It exploits the power-law behavior of electric fields near sharp electrode features and is intended to be compatible with the limited mesh resolution in present full-component modeling. Completion of this predictive method also awaits data from tests employing longer radiation pulses.

Significance: Past experience has provided limited guidance for designing to prevent electrical breakdown of GMB-filled epoxy in radiation environments. In particular, no validated breakdown-predictive model is currently available for the typical situation of highly nonuniform electric fields. A practical computational tool that accommodates field concentration, and could be applied during the design phase, would be of great value in reducing costly build-and-test cycles.

Contact: Bob Anderson, Ceramic Materials Dept., 1843
Phone: (505) 844-7676
Fax: (505) 844-7910
Email: raander@sandia.gov

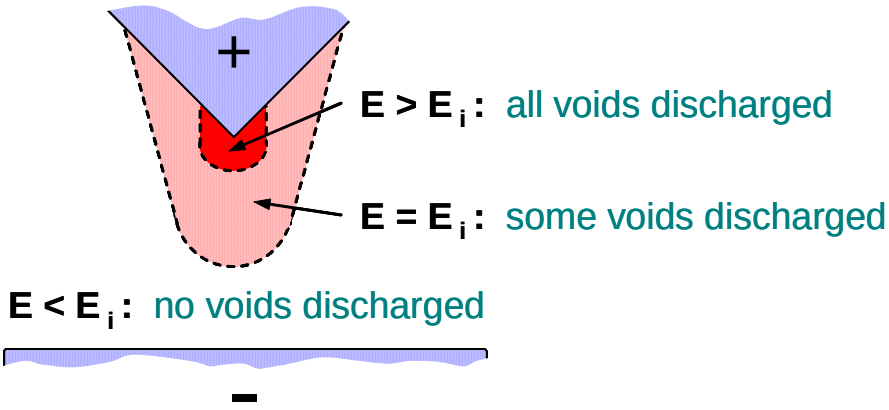

Figure 1. Electric field screening from radiation-induced void discharges. Fields very near a sharp electrode tip are above the discharge inception field, E_i, of a microballoon void and all voids become discharged. The greater void-discharge polarization near the tip reduces the size of the field at the tip, but the void discharges also reduce the encapsulant dielectric strength there. Both effects must be taken into account.

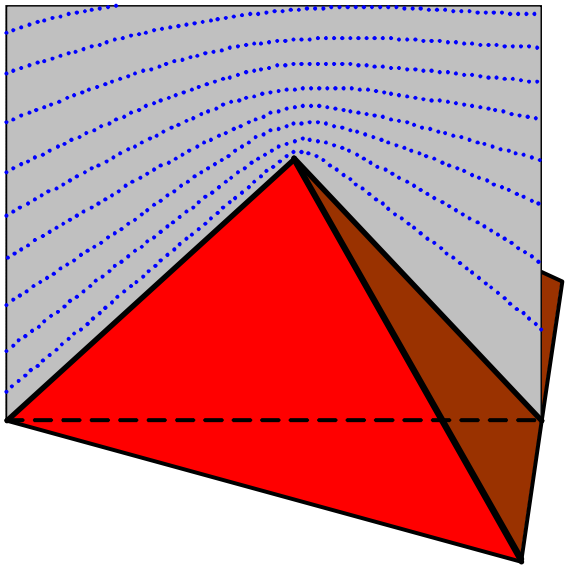

Figure 2. Section through equipotential surfaces near a rectangular electrode corner. A test-sample electrode incorporating this geometry at its tip has the shape of a cylinder that is cored from a solid cube, with the cylinder axis centered on a cube body diagonal.

Nonlinear Viscoelasticity of Polymers

D. Adolf, R. Chambers, J. Caruthers

Motivation: Rubbery polymers are unarguably viscoelastic, but extending this mathematical framework to glassy polymers to predict yield and aging phenomena has proven difficult historically. While the glass transition itself arises from polymer viscoelastic relaxations, yield has typically been predicted by postulating a separate mechanism using a plasticity approach. We have chosen to describe all phenomena through a thermodynamically consistent, nonlinear viscoelastic framework.

Accomplishment: Through the "Rational Mechanics" framework, the Helmholtz free energy provides a potential for deriving all thermodynamic quantities including the stress. The equilibrated free energy was expanded in a Taylor series about an arbitrary reference state, and the decaying free energy was expanded in a Frechet series about this underlying equilibrated material.

While this approach provides a consistent formulation of viscoelasticity, the physics required to capture yield, aging, and the glass transition reside in an accurate description of how polymer relaxations depend on the thermodynamic state. The historical "WLF" equation seems to reproduce the dependence of relaxations on temperature in the equilibrated material, but we require a much broader relationship. From both the results of molecular dynamics and agreement of theoretical stress/strain predictions with experimental data, it appears that the relaxations depend on the potential energy of the system.

Using this potential energy "material clock" and the thermodynamically consistent framework, we have developed a constitutive equation that accurately predicts the diverse phenomena observed in glassy polymers. Temperature-dependent mechanical yield in different modes of deformation, enthalpy relaxation, physical aging, volume recovery, and creep can be consistently predicted with one physically-based set of input parameters.

Seven different unfilled polymers have now been characterized: 6 epoxies and polycarbonate. The theoretical inputs are linear viscoelastic quantities (shear and bulk moduli, heat capacity, and coefficient of thermal expansion), so all nonlinear predictions arise from the structure of the equations. Enthalpy relaxation peaks, changes in the viscoelastic shift factor with aging time, and mechanical yield are examples of validated predictive capabilities. Figure 1 shows an example of the level of quantitative agreement achieved with this approach.

We have even characterized four filled polymers (epoxies up to 50vol% filler) as homogenized continua and achieved quantitative agreement between predictions and data. An example is shown in Figure 2.

Significance: Not only can stresses and strains be accurately predicted in the polymers we use, but there is a clear and consistent interpretation of the underlying physics. Additionally, this approach has enabled us to attack such problems as quantitative prediction of cohesive and adhesive failure, nonlinear response of orthotropic polymer composites, and the behavior of polymers at high rates.

Contact: Doug Adolf, Organic Materials Dept., 1811
Phone: (505) 84-4773
Fax: (505) 844-9624
Email: dbadolf@sandia.gov

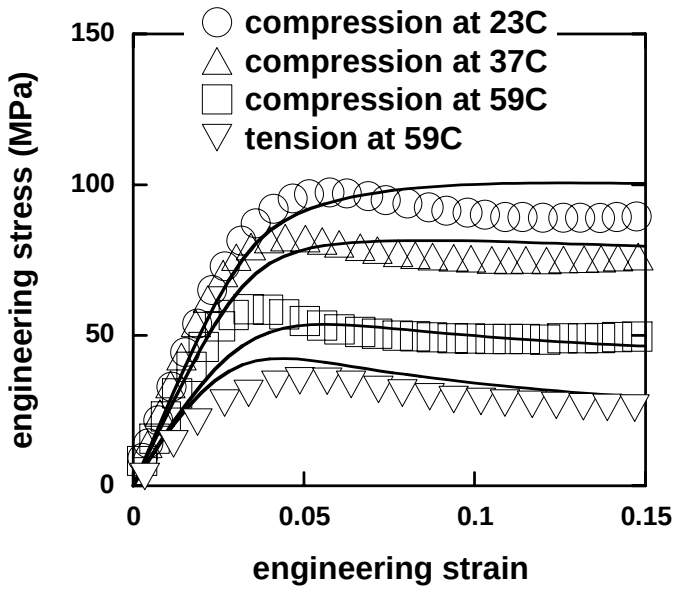

Figure 1. Comparison of predictions and data for the temperature-dependent yield of an epoxy.

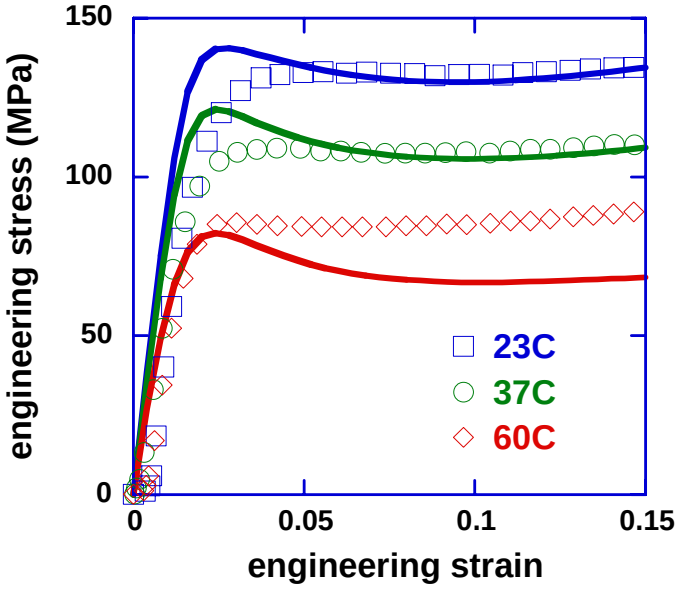

Figure 2. Comparison of predictions and data for the temperature-dependent yield of an epoxy filled with 40vol% glass spheres.

Parachute Aging Studies

R. Bernstein, K.T. Gillen

Motivation: Organic materials, more specifically polymers, are often the 'weakest' part of any component. Devices made of polymers age, thus time may have a dramatic effect on the chemical and therefore physical properties. Understanding how these polymers age, along with predictions of 'lifetimes' and real world analysis of aged polymers are important aspects in the determination of the reliability and life expectancy of any system.

Accomplishment: Utilization of our radiation and thermal aging facilities allows us the ability to better extrapolate lifetimes by performing accelerated aging under various aging conditions over extended time periods. This ranges in time from days to months/years. The ability to cover many temperatures for long times allows dramatically enhanced lifetime predictions. The classical application of the Arrhenius equation involving a few high temperature short time experiments can lead to highly misleading predictions of room temperature real world aging.

We use classical as well as highly specialized techniques to measure both bulk and localized properties of the polymer. New techniques/approaches are constantly being sought to monitor/predict polymer aging behaviors that are applicable to a variety of different polymers, and/or broaden our current techniques to examine polymers previously not amenable to analysis. Our research involves examining polymers from various components/devices. Current projects are examining Nylon and Kevlar from parachutes.

A specific example focuses on the degradation of Nylon used in parachutes. Thermal accelerated aging studies as well as innovative humidity studies are being performed to better understand and separate the role of thermal oxidation and hydrolysis mechanisms in the degradation of Nylon. From the tensile strength data obtained thus far it is apparent that a synergism exists between molecular dioxygen and water leading to an enhanced amount of degradation when both are present (Figure 1). Physical properties are monitored, as well as chemical properties. A correlation is being sought between these properties with the goal of this work to predict the service lifetime of the Nylon, and to perform condition monitoring of the Nylon in the field. The latter involves removal and testing of small samples of Nylon from parachutes to determine the overall condition and remaining lifetime.

An example of a condition monitoring technique is Ultra-Violet Visible (UV-VIS) spectroscopy. This technique involves dissolving the Nylon and quantifying the wavelength specific absorptivity as a function of aging. This can then be compared to the tensile strength remaining, providing a link between the chemical and physical properties. UV-VIS works quite well for thermal-oxidative aging, but becomes complicated when humidity degradation pathways are involved (Figure 2). The complication stems from absence of any chromophore formation from a pure hydrolysis degradation, and a synergism between molecular dioxygen and water in the formation of the chromophore when both species are present.

Significance: This study has revealed a previously unknown synergism in the degradation of Nylon. When both water and oxygen are present, the rate of degradation is dramatically increased more than the expected linear sum of the two pathways. Use of UV-VIS spectroscopy as a condition monitoring technique was shown to be misleading because of the importance of the hydrolysis mechanism of degradation.

Contact: Robert Bernstein, Organic Materials Dept., 1811
Phone: (505) 284-3690
Fax: (505) 844-9624
Email: rbernst@sandia.gov

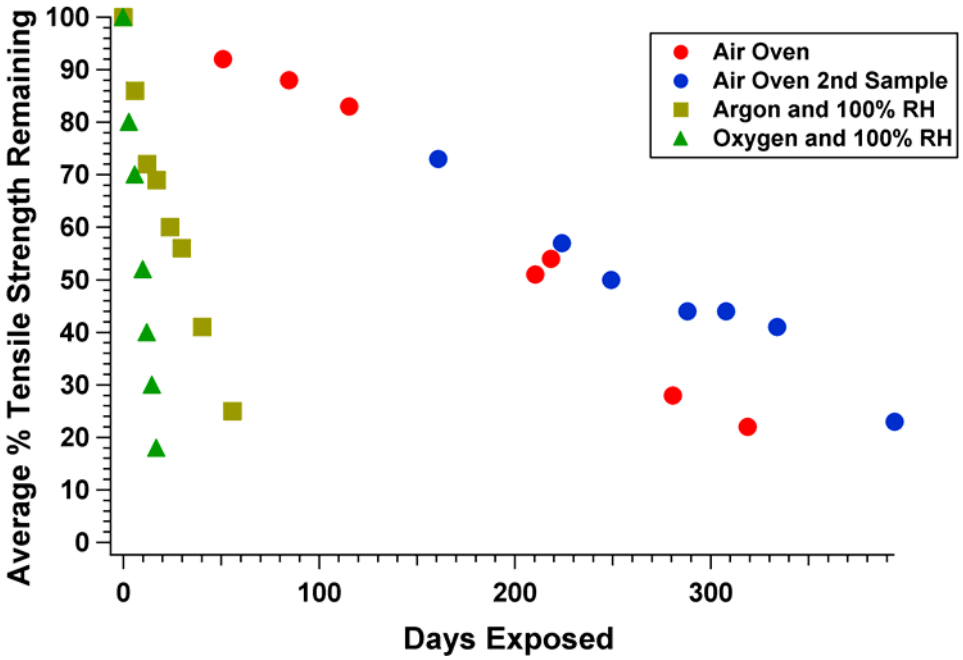

Figure 1. Nylon percent tensile strength remaining as a function of days exposed to 125°C: Air (circles), Argon and 100% RH (squares), and Oxygen and 100% RH (triangles).

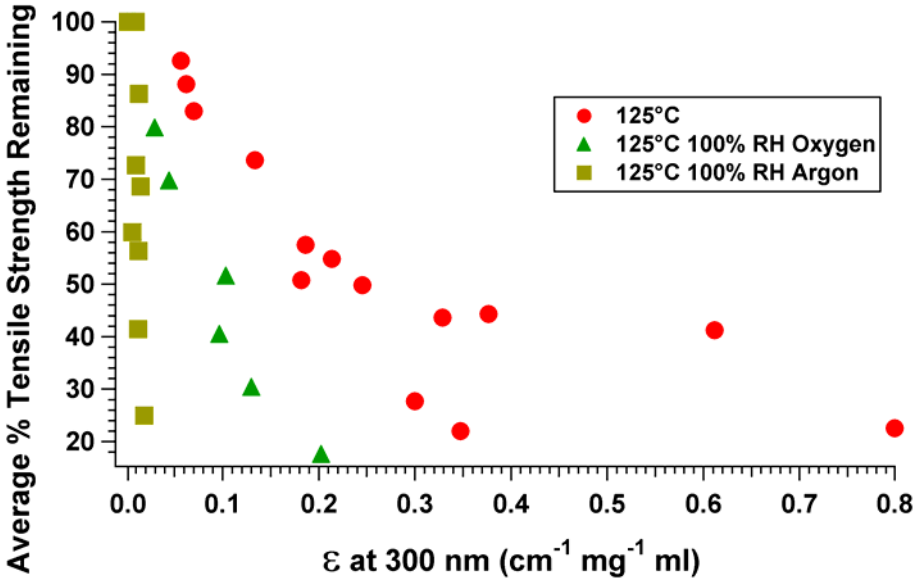

Figure 2. Extinction coefficient (Absorptivity) vs. average percent tensile strength remaining at 125°C under various environments; in an air circulating oven (circles), 100% RH with an argon atmosphere (squares), and 100% RH with an oxygen atmosphere (triangles).

Prediction and Validation of O-Ring Lifetimes

K. T. Gillen, M. Celina, R. Bernstein

Motivation: O-rings are used in many critical long-term applications, thus requiring accurate lifetime predictions. However, such predictions involve understanding and extrapolating a complex combination of mechanical stress decay and the aging environment. Our goals were to improve on past attempts that have focused on and implicitly trusted Arrhenius extrapolations of high-temperature stress-relaxation results.

Accomplishment: Since compression stress-relaxation (CSR) experiments follow the sealing force decay under compression (an ideal parameter for following o-ring degradation), our initial goal was to derive superior methods for carrying out such experiments. We first determined that diffusion-limited oxidation (DLO) effects often lead to anomalous CSR results. By modeling DLO effects in terms of O_2 permeability and consumption and by making experimental measurements of these two parameters versus temperature, we were able to determine the sample geometries required to eliminate DLO-caused errors. This allowed valid CSR results to be generated versus aging.

As an example, we carried out accelerated temperature (80°C to 110°C) CSR experiments on two important butyl o-ring formulations (labeled Butyl-A and Butyl-B) under conditions where DLO effects are unimportant and then time-temperature superposed the results at the lowest aging temperature of 80°C; the results are shown in Figs. 1 and 2. The superposed results at 80°C (bottom x-axes) indicate that Butyl-B reaches 50% force decay in ~50 days versus ~120 days for Butyl-A. However, the larger shift factors for the Butyl-B CSR results versus those of Butyl-A (shown on figures) lead to a much higher Arrhenius E_a for the former (~102 kJ/mol) versus the latter (~80 kJ/mol). Conventional Arrhenius extrapolation from 80°C to 23°C leads to the conclusion that Butyl-A will reach 50% force decay after ~63 years at 23°C versus ~150 years for Butyl-B.

Our second goal was to increase confidence in such Arrhenius extrapolations by obtaining aging results correlated to the degradation of interest in the low temperatures extrapolation regime. Since oxidation drives the chemistry responsible for the force decay, we have developed ultrasensitive oxygen consumption measurements that can be made at low temperatures (down to 23°C for the current butyl materials). Superposition of the O_2 consumption results from 23°C to 110°C leads to O_2 shift factors that allow us to confirm the correlation of O_2 consumption with CSR at high temperatures and to more confidently extrapolate the CSR results below 80°C. The shift factors for the two butyl materials, shown in Figs. 3 and 4, indicate that significant curvature to lower E_a occurs for Butyl-B but not for Butyl-A. Using the E_a values derived from O_2 consumption to extrapolate the 80°C CSR results down to 23°C leads to the top x-axes shown in Figs. 1 and 2. In contrast to the earlier conventional extrapolation, the time to 50% force decay for Butyl-B drops from ~150 years to ~ 20 years. This prediction compares favorably with observed compression set results of 50±20% for Butyl-B seals after ~20 years at 23°C (20 year compression set values for Butyl-A are ~20±10%).

Significance: We have made important improvements to the methodology needed to predict the lifetime of o-rings in air environments by understanding the importance of DLO effects and deriving an approach (ultrasensitive O2 consumption) that results in more confident lifetime predictions. By applying these techniques to two butyl materials, we were able to show that our predictions were consistent with 20-year field results.

Contact: Ken Gillen, Organic Materials Dept., 1811
Phone: (505) 844-7494
Fax: (505) 844-9781
Email: ktgille@sandia.gov

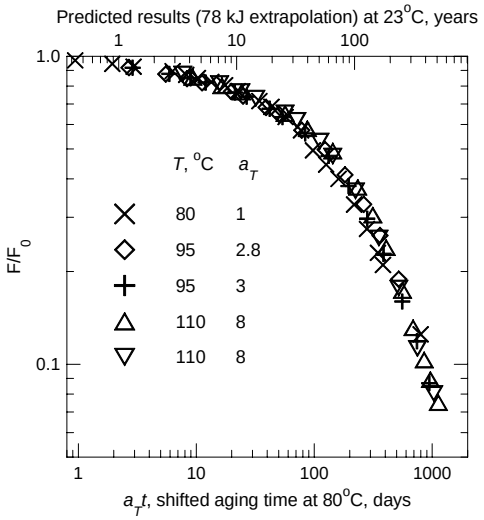

Figure 1. Time-temperature superposed force decay results at 80°C (lower x-axis) for Butyl-A. The shift factors a_T used are indicated. The top x-axis shows the extrapolated prediction at 23°C derived from the ultrasensitive oxygen consumption results.

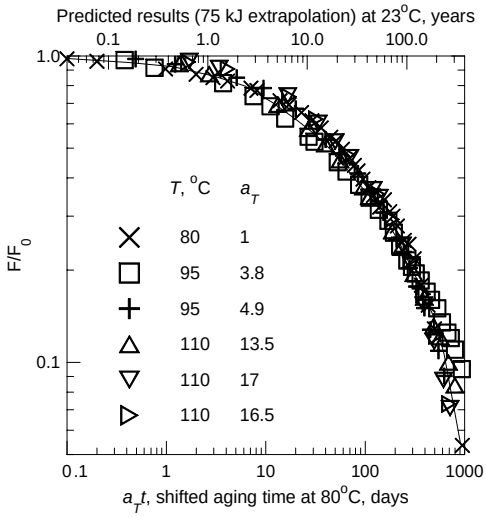

Figure 2. Time-temperature superposed force decay results at 80°C (lower x-axis) for Butyl-B. The shift factors a_T used are indicated. The top x-axis shows the extrapolated prediction at 23°C derived from the ultrasensitive oxygen consumption results.

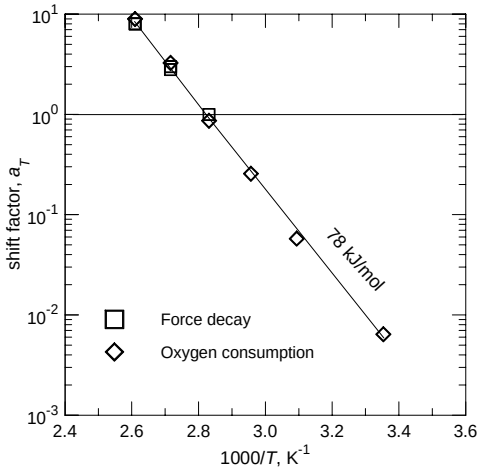

Figure 3. Arrhenius plot of the shift factors for the Butyl-A material.

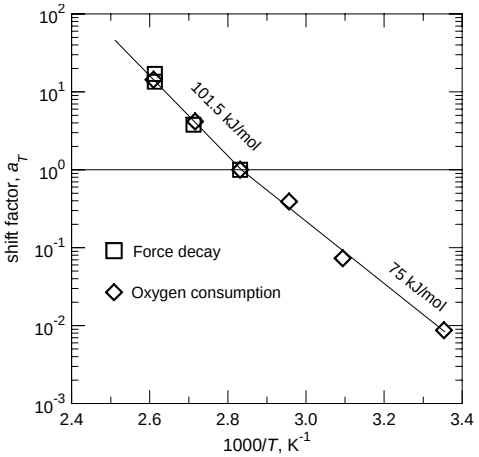

Figure 4. Arrhenius plot of the shift factors for the Butyl-B material.

Quantitative Prediction of Polymer Adhesive Failure

D. Adolf, R. Chambers

Motivation: Studies of polymer adhesion have typically followed two approaches. The goal of the first lies in developing methods to improve adhesion, while the second focuses on methods to predict adhesive failure. Both can lead to better "understanding" of the mechanism of adhesion and delamination. We have focused on developing a computational technique that enables accurate prediction of the initiation of polymeric adhesive failure at interfaces of arbitrary geometry for any temperature or rate.

Accomplishment: Instead of ignoring the high stresses in the bulk polymer as is typically done in fracture mechanics type approaches to adhesive failure, we calculate them accurately for a specific, experimental, interfacial failure test. High fidelity stress predictions are only possible with a consistent, accurate constitutive equation, and such capability has only recently been developed at the Labs. The stresses, or more precisely the interfacial tractions, at the experimentally observed initiation of adhesive failure can be predicted for various modes of deformation, test temperature or rate, and sample geometry. The simplest picture arising from an examination of these data would result in one critical traction that defines failure. A constant number of bonds between the polymer and substrate could be a physical basis for such a result.

Unfortunately, complications arise in typical experimental lap shear and butt tensile characterization tests. Failure always initiates at the air-polymer-substrate corner, which is ill-defined geometrically. While this corner may be typically drawn as a 90° angle, surface tension, thermal stresses, and cure shrinkage all conspire to create a curved, temperature-dependent interfacial profile. Since the stress intensity is directly related to this curvature, accurate stress predictions are impossible if the geometry is unknown or changing. We designed a new test geometry (Figure 1) for which (1) failure initiates away from an air interface, (2) different modes of deformation (e.g., shear, tension, and combined loadings) can be examined in one fixture, (3) stresses at the initiation site are fairly spatially uniform, and (4) the effects from coefficient of thermal expansion mismatch are minimized.

Using this new fixture and the SNL nonlinear viscoelastic theory for predicting stresses in glassy polymers, the critical traction was extracted from one test and applied to all others that probed different temperatures and modes of deformation. Figure 2 shows the agreement between theory and data for temperature-dependent tensile failure. Model computational simulations demonstrated that surface roughness produces a slightly smaller apparent shear critical traction as compared to that in tension. Experiments validated this prediction.

Significance: We have used the capability for quantitative prediction of stresses and strains in polymers to define a method for predicting adhesive failure in different modes of deformation at different temperatures and rates. Without such quantitative failure metrics, computational simulations of component stresses can only predict trends associated with design or material changes. With these metrics, lifetime reliability estimates and design margins are enabled.

Contact: Doug Adolf, Organic Materials Dept., 1811
Phone: (505) 84-4773
Fax: (505) 844-9624
Email: dbadolf@sandia.gov

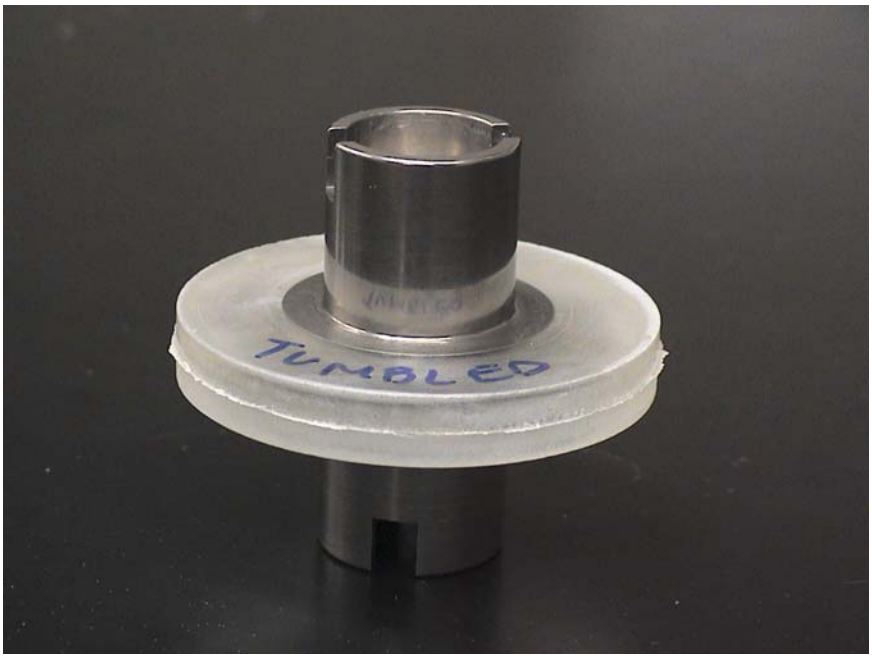

Figure 1. A new test geometry for measuring the adhesive strength in polymers.

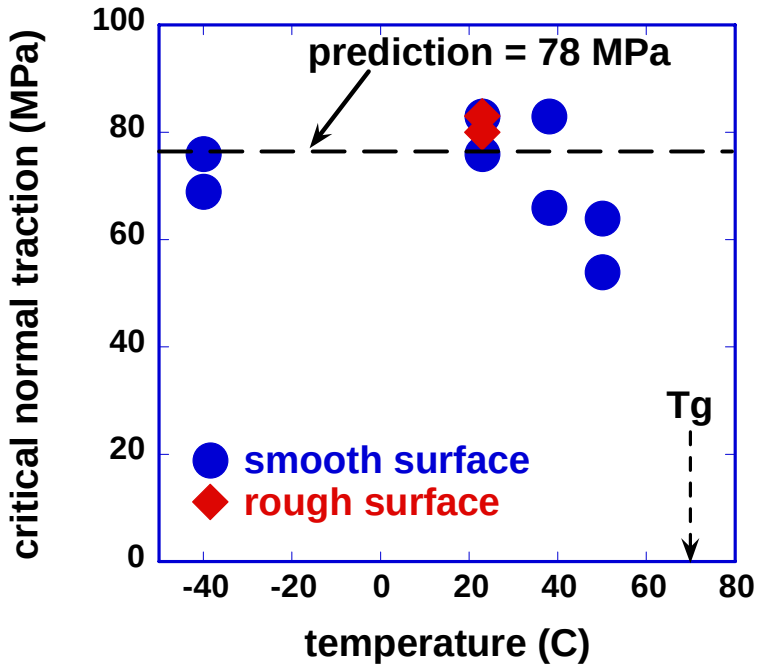

Figure 2. Comparison of predictions and data for the temperature-dependent tensile adhesive failure of an epoxy to stainless steel.

Electrochemical Oxidation of Carbohydrates for Fuel Cell Applications

M. Kelly, D. Ingersoll

Motivation: Autonomous, distributed power systems are required for cooperative microsensor networks being developed for a number of applications, including battlefield management, border management, and surveillance, monitoring, and intelligence gathering scenarios. Many research institutions are developing higher energy density power sources with improved operational lifetimes and reduced size and weight. As part of a Grand Challenge LDRD project, Sandia is developing micro fuel cells that employ carbohydrate fuels (e.g., sucrose and glucose) that can be derived from biological sources (e.g., plants and animals). The combination of the inherent high energy density associated with fuel cells and the potential to "harvest" fuel for dramatically extended operation is being studied in a multidisciplinary project encompassing integration of advanced catalysts, membranes, current collectors, flow fields, harvesting implements, and other associated fuel cell hardware into advanced design concepts.

Accomplishment: The catalysts under consideration for the fuel cell anode include noble metals (e.g., Pt), noble metal alloys (e.g., Pt-Ru), other metal alloys (e.g., Pt-Co, Pt-Zn, Pt-Sn, Pt-Bi), and enzymes (e.g., glucose oxidase). We have used cyclic voltammetry to electrochemically evaluate glucose and sucrose under a variety of relevant conditions. In Figure 1, the voltammograms for a polycrystalline Pt electrode in a pH 7 phosphate buffer (red curve) and in a buffer solution containing 50 mM glucose (blue curve) is shown. The background voltammogram contains all the well-known features for Pt electrochemistry: hydrogen adsorption and desorption peaks (between ~ –300 and –500 mV vs. Ag/AgCl), oxidation of the platinum surface at anodic potentials (~ +1100 mV), and reduction of the surface oxide at ~ +80 mV. When glucose is added to the supporting electrolyte, significant oxidation currents are evident in some 5-6 anodic peaks between –400 and + 600 mV. Further, there is strong evidence in the voltammogram for poisoning of the electrode surface (presumably by adsorption of gluconolactone, an oxidation product of glucose oxidation). In alkaline solutions, significantly increased currents are observed for glucose oxidation. In Figure 2a, the background-corrected voltammogram for glucose in 0.1 M NaOH (pH 13) is shown. The larger set of peaks represent oxidation of glucose during anodic scans, while the smaller set of peaks are due to oxidation of glucose during cathodic scans. During the cathodic scans, the adsorbed gluconolactone is removed ("electrode depoisoning"), thereby allowing glucose oxidation to occur at an appreciable rate. The electrochemical behavior of sucrose in alkaline solutions is rather similar to that of glucose (Figure 2b).

Significance: The dramatic increase in oxidation currents for glucose at high pH has influenced Sandia's prototype micro fuel cell designs in that strong consideration is being given to including a solid chemical reagent in the flow field that will buffer the carbohydrate fuel to an optimal pH. We are also evaluating carbohydrate oxidation at noble metal and noble metal alloy nanoclusters being synthesized by other Sandia researchers as part of research into improved anode catalysts for hydrogen fuel cells. Here, potentially dramatic changes in cluster surface chemistry may lead to improved electrocatalytic properties for glucose and sucrose oxidation.

Contact: Mike Kelly, Materials Characterization Dept., 1822
Phone: (505) 844-4031
Fax: (505) 844-2974
Email: mjkelly@sandia.gov

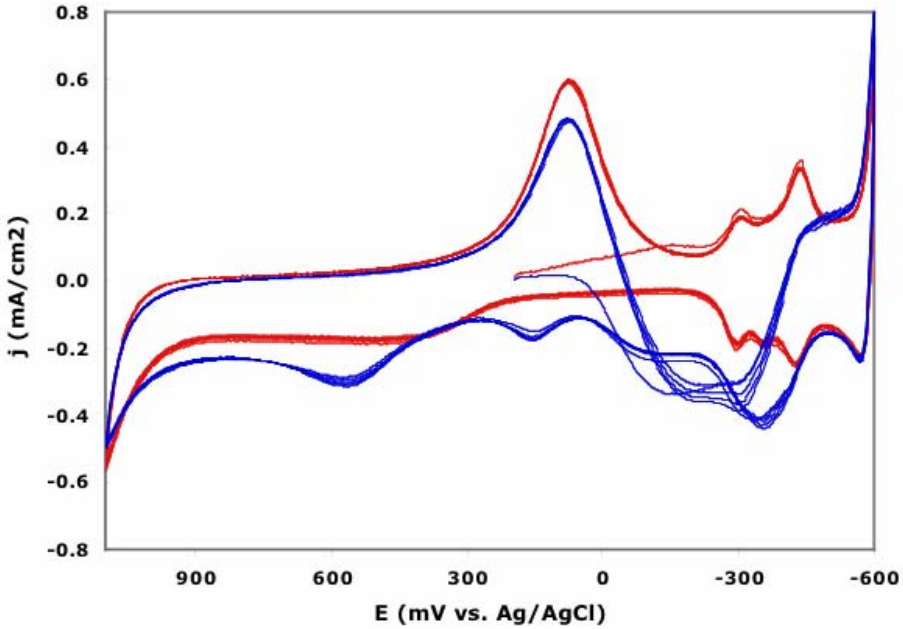

Figure 1. Cyclic voltammetry of 55 mM glucose at Pt working electrode at neutral pH. Supporting electrolyte: 0.05 M phosphate buffer, pH 7. Red – background voltammogram obtained in absence of glucose. Blue – glucose voltammogram..

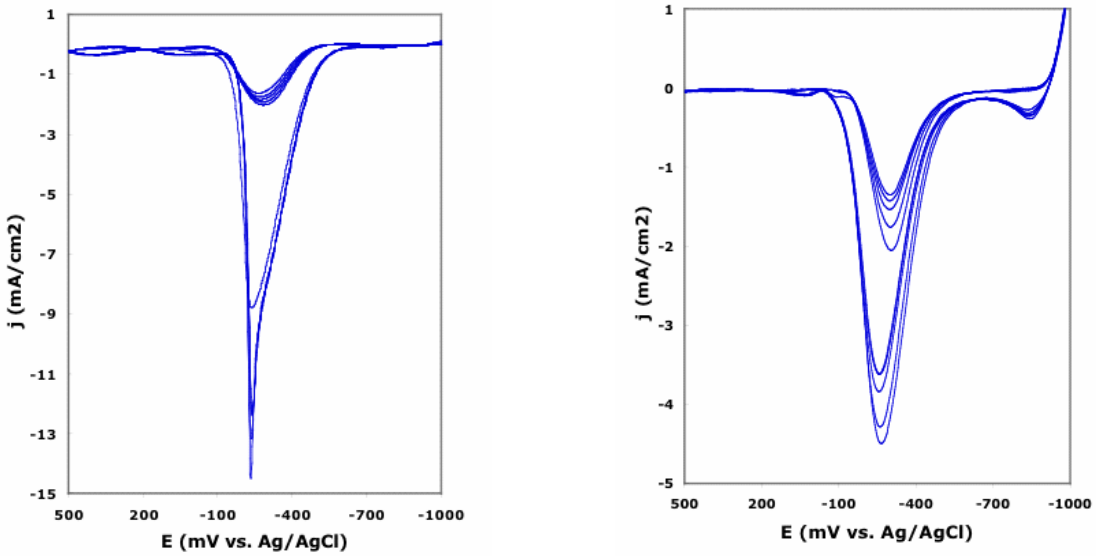

(a) (b)

Figure 2. Background-corrected voltammograms of glucose and sucrose at Pt working electrode at alkaline pH. Supporting electrolyte: 0.1 M NaOH. (a) 55 mM glucose. (b) 58 mM sucrose.

Insights into the Molecular Mechanisms of Membrane Fusion

M. J. Stevens

Motivation: The molecular detail of the fusion between two lipid bilayers is one of the most vexing problems in membrane biophysics today. The process of membrane fusion is central to biology, and plays a role in events such as vesicular trafficking, fertilization, viral entry and mitosis. Fusion models based on continuum mechanics predict initial fusion of the outer leaflets to form a stalk-like structure, and the subsequent merger of the two sides. However, the molecular apects of membrane fusion are not treated by the continuum models and have yet to be determined experimentally.

Accomplishment: We have performed molecular dynamics (MD) simulations that suggest new processes in membrane fusion and reveal novel molecular details of lipid movement.

In a typical fusion simulation, the process begins with the formation of a flattened contact between the liposomes. This causes membrane bending at the contact edge bringing two strained points on the membranes into close proximity. Fusion between the outer membrane leaflets initiates at the edge of the contact surface (Fig. 1). There are several factors that promote fusion at the contact edge, including strain that is relieved by fusing with the neighboring liposome and an increase in area per lipid giving more mobility to molecules in this region. While this finding of edge originated fusion is intuitive, it offers a contrasting view to that described in existing models. The applied force causes membrane bending at the contact edge bringing two strained points on the membranes into close proximity where fusion initiates. Hence the point of fusion can be significantly distal to the initial point of closest approach.

The simulations also provide direct insight into the dynamics of individual lipids during the early stages of fusion. To begin with there is a tilting of the lipids at the presumptive point of fusion, similar to that proposed for the modified stalk model which appears to be facilitated by the local increase in the area per lipid. The first exchange between the membranes occurs when an aliphatic tail rotates out of the parent membrane and inserts into the opposing membrane, resulting in a tilted lipid with the aliphatic tails in a splayed (trans) conformation that is shared between the two fusing bilayers (Fig. 2). This immediately suggests a mechanism for accommodating curvature strain on a molecular level. The possibility of splayed lipid conformations has been considered in some models for membrane fusion however the picture that emerges here is distinctly different. In our simulations the splayed lipids tend to orient such that their aliphatic tails contact each other, thus creating the beginnings of a new hydrophobic core. As additional (tilted) lipids associate with the splayed bridging lipids, the aliphatic tails of these molecules extend into a more cis-like conformation, establishing a hydrophobic core and eventually forming a classical stalk.

Significance: While many of the general features of our simulations agree well with models based on a continuum mechanics framework, the present work offers significant new insights into the molecular details of the early stages of fusion. In particular the simulations suggest a model for specific molecular rearrangements that result in the formation of a stalk. In addition, a number of interesting considerations arise from these results, including new ways in which proteins might mediate the fusion process.

Contact: Mark Stevens, Materials & Process Modeling & Computation Dept., 1834
Phone: (505) 844-1937
Fax: (505) 844-9781
Email: msteve@sandia.gov

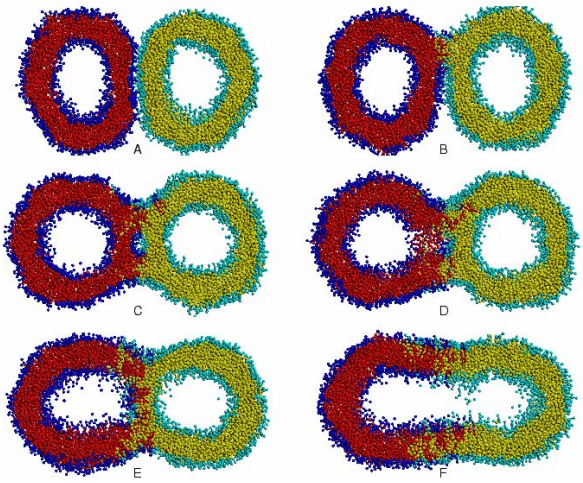

Figure 1. Cross sections (5 nm thick) of fusing liposomes showing sequence of events to complete fusion. (A) flat interface at t = 55 μs (B) initial stalk at t = 94 μs (C) growth of stalk to other side with solvent cavity at t = 140 μs (D) dissolution of one connector and solvent cavity t = 149 μs (E) intermediate fusion state at t = 204 μs (F) complete fusion at t = 231 μs. The nonspherical shape of the fused liposome is a consequence of geometric constraints on the surface area and volume of the fused liposome (25). Coloring scheme: right (left) liposome has H blue (cyan) and T red (yellow). Solvent is not displayed. The system is under osmotic pressure with internal solvent density 20% larger than external density.

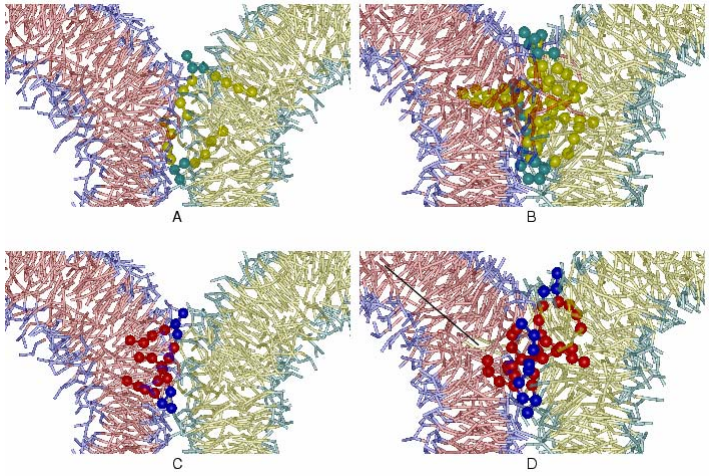

Figure 2. Lipid conformations and associations in the early stages of fusion. System and coloring scheme is same as in Fig. 1. The left side is at t = 58 μs and right side at t = 66 μs. A) and C) show splaying of lipids that often bridges the two outer leaflets. There is a tendency for the aliphatic tails of the splayed lipids to oppose each other. B) and D) show association of splayed lipids and the beginning of a hydrophobic core that spans the space between the two liposomes. These lipids have typically rotated or one of the tails has rotated so that the orientation better matches the stalk structure. The line in D) is a guide to the eye to indicate the ordering of the upper bilayer to become part of the stalk. For evolution beyond t = 66 μs the external force was turned off; the subsequent dynamics is shown in Fig. 1.

Protein Interactions with Lipid Membranes by Neutron Reflectivity

M. Kent, H. Yim, D. Sasaki

Motivation: We used neutron and X-ray reflection to study protein adsorption to Langmuir monolayers of metal-ion-chelating lipids. The adsorption of proteins to surfaces, and especially lipid membranes, plays a critical role in biochemical processes within living systems, toxin assault on cell membranes, biosensor strategies, and in directing the formation of protein complexes and supramolecular structures in nanoscience initiatives. The use of metal ion coordination to target the adsorption of proteins to lipid membranes has been studied extensively by others [1]. This method utilizes coordination interactions between divalent metal ions and naturally occurring histidine units, genetically engineered metal-ion binding sites, or polyhistidine units inserted at either the N or C terminus of proteins. Particularly useful is the fact that the interaction energy between histidine and the chelated metal ion varies greatly depending upon the nature of the metal ion. For example, the interaction energy for Cu^{2+}/IDA with histidine is 15 times greater than that for Ni^{2+}/IDA with histidine. Our goals are to understand how to target adsorption of specific proteins, manipulate the orientation and density of adsorbed proteins, determine the time scale of adsorption, determine conditions for which proteins penetrate into the lipid membranes, and understand the conditions for denaturation.

Accomplishment: We prepared Langmuir monolayers of 100% DSIDA (metal ion - chelating synthetic lipid) spread onto the surface of H_2O subphases[2]. With the surface area held constant, we obtained the reflectivity of the lipid monolayer with adsorbed metal ions (Cu^{2+} or Ni^{2+}) and then after injection of myoglobin (dimensions: 44 Å x 44 Å x 20 Å). Data were obtained as a function of time until no further variation was detected (after ~ 14 hrs). Reflectivity data are shown in Figure 1 for Cu^{2+} loaded into the DSIDA. These data reveal for the first time detailed structural characteristics of a protein layer as a function of time during the adsorption process. Results for both Cu2+- and Ni^{2+}-loaded DISDA are shown in Figures 2 and 3. Both the thickness and the average segment volume fraction are consistent with a nearly end-on orientation throughout the adsorption process for Ni^{2+}, but a transition from side-on to an end-on orientation with increasing protein surface density in the case of Cu^{2+} ions. This is illustrated in Figure 4.

Significance: These results suggest that it may be possible to design systems for which certain useful activities, such as enzymatic reactions, could be regulated by controlling the orientation of the adsorbed protein through the bulk protein concentration or the nature of the chelated metal-ion.

[1] Maloney, K. M.; Shnek, D. R.; Sasaki, D. Y.; Arnold, F. H. Chemistry & Biology, 1996, 3, 185
[2] Kent, M.; Yim, H.; Sasaki, D.; Satija, S.; Majewski, J.; Gog, T. JACS, under review

Contact: Mike Kent, Microsystem Materials, Tribology & Technology Dept., 1851
Phone: (505) 845-8178
Fax: (505) 844-9781
Email: mskent@sandia.gov

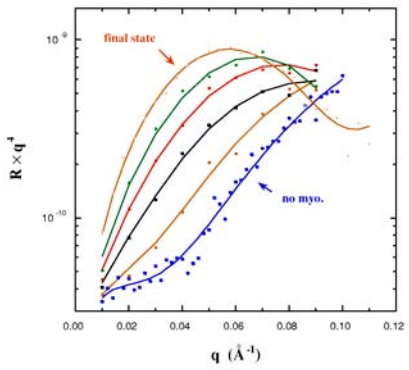

Figure 1. Reflectivity as a function of time during the adsorption process for Cu^{2+}-loaded DSIDA. The bulk concentration of myoglobin was 10 μM. Curves were obtained at 30 minute intervals. Only a few select curves are shown.

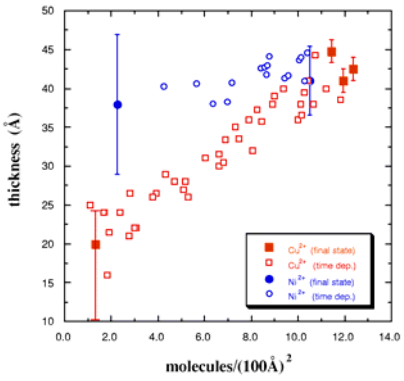

Figure 2. Evolution of the thickness of the adsorbed protein layer as a function of time during the adsorption process for Cu^{2+}-loaded and Ni^{2+}-loaded DSIDA. The filled symbols represent the final state for bulk myoglobin concentrations of 10 and 0.1 μM in the case of Cu^{2+}-loaded DSIDA and 50 and 10 μM in the case of Ni^{2+}-loaded DSIDA. The open symbols represent the time dependent values for bulk myoglobin concentrations of 10 μM in the case of Cu^{2+}-loaded DSIDA and 50 μM in the case of Ni2+-loaded DSIDA.

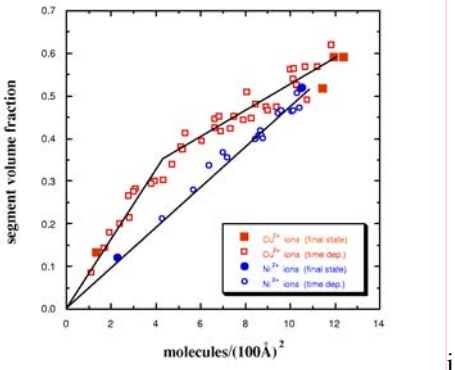

i

Figure 3. Evolution of the average segment volume fraction of the adsorbed protein layer as a function of time during the adsorption process for Cu^{2+}-loaded and Ni^{2+}-loaded DSIDA. The filled symbols represent the final state for bulk myoglobin concentrations of 10 and 0.1 μM in the case of Cu^{2+}-loaded DSIDA and 50 and 10 μM in the case of Ni^{2+}-loaded DSIDA. The open symbols represent the time dependent values for bulk myoglobin concentrations of 10 μM in the case of Cu^{2+}-loaded DSIDA and 50 μM in the case of Ni^{2+}-loaded DSIDA.

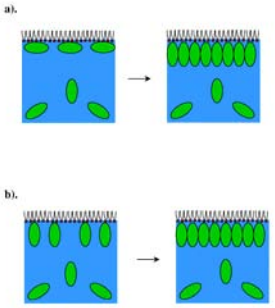

Figure 4. Schematic representation of the evolution of the adsorbed protein layer as a function of time for a) Cu^{2+}- and b) Ni^{2+}- loaded DSIDA.

Understanding Complex Biological Systems with Hyperspectral Imaging

J. Timlin, M. Sinclair, D. Haaland

Motivation: A significant limitation of commercial fluorescence imaging systems for biological applications is their inability to discriminate photons by source. These systems are univariate, filter-based instruments and thus require multiple scans of spectrally distinct fluorescent labels to produce images. Images of complex biological systems are often contaminated by emissions from species other than the fluorescent labels and improvements to the technology in order to understand and minimize the effect of these unwanted emissions are needed to provide accurate, reliable data.

Accomplishment: We have designed, constructed, and characterized a state-of-the-art hyperspectral fluorescence-imaging microscope that collects a full emission spectrum (500-900 nm) at each image pixel. With the use of multivariate data analysis we can discover and quantitate the emissions from the spectral data with little information a priori. The benefits of hyperspectral imaging and multivariate data analysis include the ability to identify and model unknown emissions, accommodate multiple (3-8) spectrally overlapped labels in a single scan, and increased sensitivity, accuracy, and reliability.

Our original hyperspectral system is optimized for scanning DNA microarrays. DNA microarrays are critical tools for biologists to understand differential gene expression due to treatment and disease, but unfortunately the largest sources of variance in microarray experiments is often not the biology of interest. Using hyperspectral imaging we have identified a spot-specific emission that would be confounded with the green DNA label in current microarray scanners. This contaminant was present in slides from commercial suppliers and in-house printed Multivariate analysis of a hyperspectral image of a microarray w/ contaminant generates pure component emission spectra (Fig 1a) and concentration maps. Using the concentration maps we can obtain a correct ratio image of the DNA labels (Fig 1b) and assess the effect of contaminant on background subtraction, normalization procedures, and the red/green ratios used for diagnostics. We have also used hyperspectral imaging to understand anomalous microarray features such as dye-separation, black holes, and background smears.

The benefits of hyperspectral imaging are not limited to DNA microarrays; any biological imaging application can potentially benefit from the ability to identify and quantitate overlapping spectral emissions in a single scan. We have begun to image multiple in situ labeled targets in brain tissue (Figure 2) to elucidate neuronal signaling and live cells expressing multicolor fluorescent proteins. These applications benefit from the ability of hyperspectral imaging to remove the effect of cellular autofluorescence on the images and increase the multiplexing capabilities. Currently we are constructing a high resolution, 3-dimensional diffraction-limited imaging system to understand even the most challenging bioimaging applications.

Significance: The biology and biomedical science communities rely on fluorescence imaging to answer important questions in cell & molecular biology, histology, and gene expression. The significant biological relationships cannot be uncovered in these complex, multicomponent systems without a detailed understanding of emissions that only hyperspectral imaging and multivariate data analysis can provide.

Contact: Jeri Timlin, Chemical and Biological Sensing, Imaging and Analysis Dept., 1812
Phone: (505) 844-7932
Fax: (505) 844-2974
Email: jatimli@sandia.gov

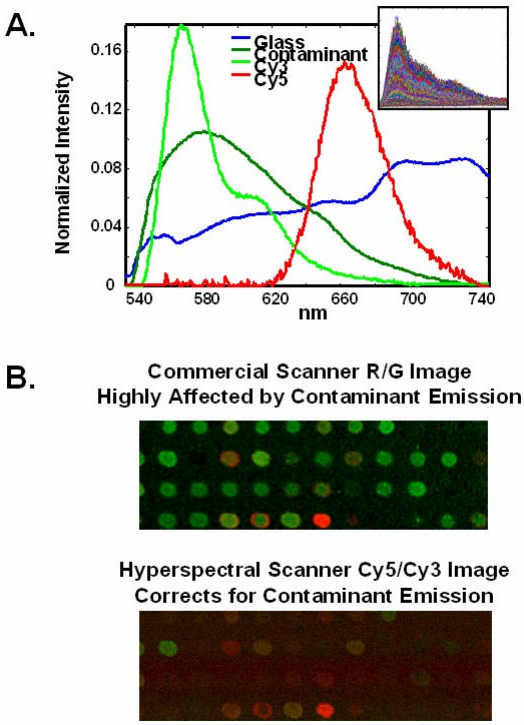

Figure 1. Hyperspectral scanning of DNA microarray with contaminant. A) Extracted pure component spectra. Inset shows 30,000 raw spectra that are input into the multivariate data analysis. B) Comparison of commercial scanner and hyperspectral scanner images. In this case, 75 % of the spots had red/green ratios in errors by a factor of 2 or more. Hyperspectral image has been scaled appropriately to match the commercial scan ratio image. Spatial resolution = 10 microns.

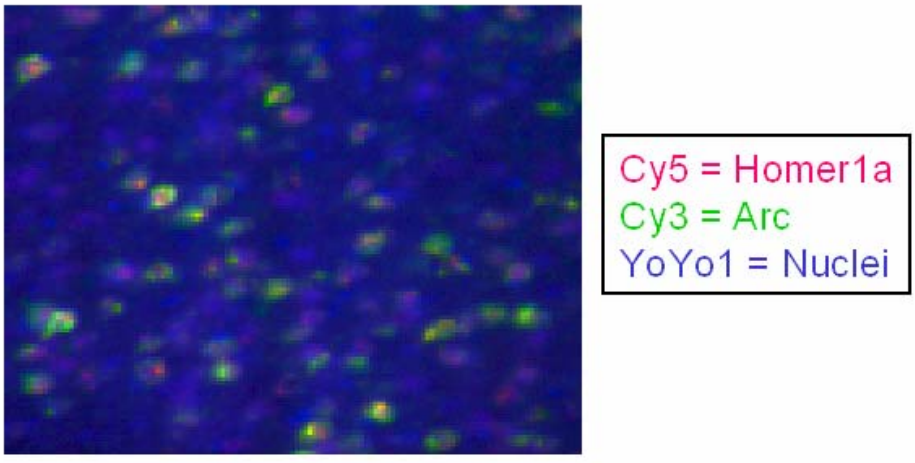

Figure 2. RGB composite image of Cy3, Cy5, and YoYo-1 label concentration maps extracted from hyperspectral image of brain tissue section. Tissue labeling was accomplished via catFISH technique and highlights cell nuclei and the ARC and Homer gene expression. Samples courtesy of J. Guzowski, UNM Department of Neurology. Spatial resolution = 5 microns.

High-Resolution Mass Spectroscopic Studies of Silica Cluster Generation from Beta Zeolite and Solvent-Modified Beta Zeolite

S. M. Thornberg, I. C. Abraham, D. E. Hunka

Motivation: Understanding the processes of cluster generation from laser ablation of materials is the first step in developing a fundamental understanding of material formation at the nanoparticle level. This project strives to develop a knowledge base for cluster generation from zeolite materials, such that the chemical properties of these clusters may then be investigated. Some work in this area has been attempted by groups without high-resolution mass capability.

Accomplishment: Formation of distinctly different cluster series from zeolite and solvent-modified zeolite has been successfully demonstrated. Negative ion cluster series have been generated through laser ablation of beta zeolite. The cluster series that are generated are highly dependent on the method of preparation given the sample prior to testing by high resolution mass spec. The two methods for plain beta zeolite sample introduction are a) a pellet of the pure zeolite pressed under ~ 100 bars of pressure, and b) to create a suspension of beta zeolite in acetone that would subsequently be adhered to a stainless steel target. The second method of preparation may serve to increase the surface silanol concentration, while the first should give a baseline spectrum for the pure, dry species.

Although the generation of the cluster series is straightforward, the identification is much less so. The complexity of the spectra is reduced when the realization is made that each series is based on increasing numbers of the SiO_2 unit. The high resolution of the Fourier transform ion cyclotron resonance mass spectrometer allows for exact mass determination and therefore absolute identification of the empirical formulas can be determined.

This exact formula identification has led to the discovery of alternate cluster formation processes. For the pure zeolite, the main cluster series produced in most abundant to least abundant order are: $[(SiO_2)_nAlO_2]^-$, $[(SiO_2)_nOH]^-$, $[(SiO_2)_nAlO]^-$, and $[(SiO_2)_nAl_3O_5]^-$, where *n* can equal 2 up to 16 for the largest cluster series (Fig. 1). Although the AlO_2^- series has been proposed in the literature, the studies that suggest such a series did not have the resolution to confirm its existence. The high-resolution capability of this laboratory has allowed the indisputable identification of the AlO_2^- series. Further, neither the AlO^- nor the $Al_3O_5^-$ cluster series have been identified in the literature previous to our studies.

For the zeolite sample that was suspended in acetone, the relative abundance of the two main cluster series is reversed (Fig. 2). The OH^- clusters are more abundant than AlO_2^- cluster series. Neither of the other aluminum-containing series $[(SiO_2)_nAlO]^-$ or $[(SiO_2)_nAl_3O_5]^-$ are produced from the ablation of this sample. However, the new series $[(SiO_2)_nH_3O_2]^-$, $[(SiO_2)_nH]^-$, and $[(SiO_2)_nH_5O_3]^-$ are generated from this preparation method. The $H_3O_5^-$ series has also been heretofore undiscovered.

Significance: These studies demonstrate that the generation of clusters from beta zeolite can be influenced by the modification of the zeolite. Perhaps by surface changes or solvent encapsulation in the zeolite that alters the type of cluster formation. The differences seen in the types of clusters generated will significantly change all succeeding experimental results and open the possibility of designer clusters created for specific studies using different zeolite-solvent ablation interactions.

Contact: Steve Thornberg, Chemical & Biological Sensing, Imaging, & Analysis Dept., 1812
Phone: (505) 844-8710
Fax: (505) 844-2974
Email: smthorn@sandia.gov

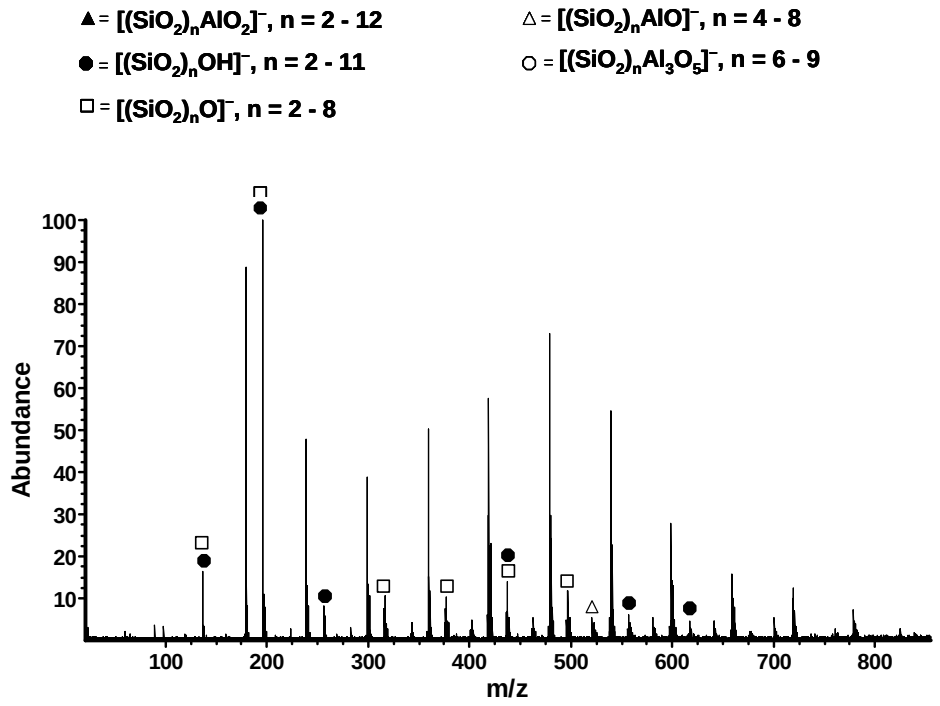

Figure 1. Mass Spectrum for pure beta zeolite

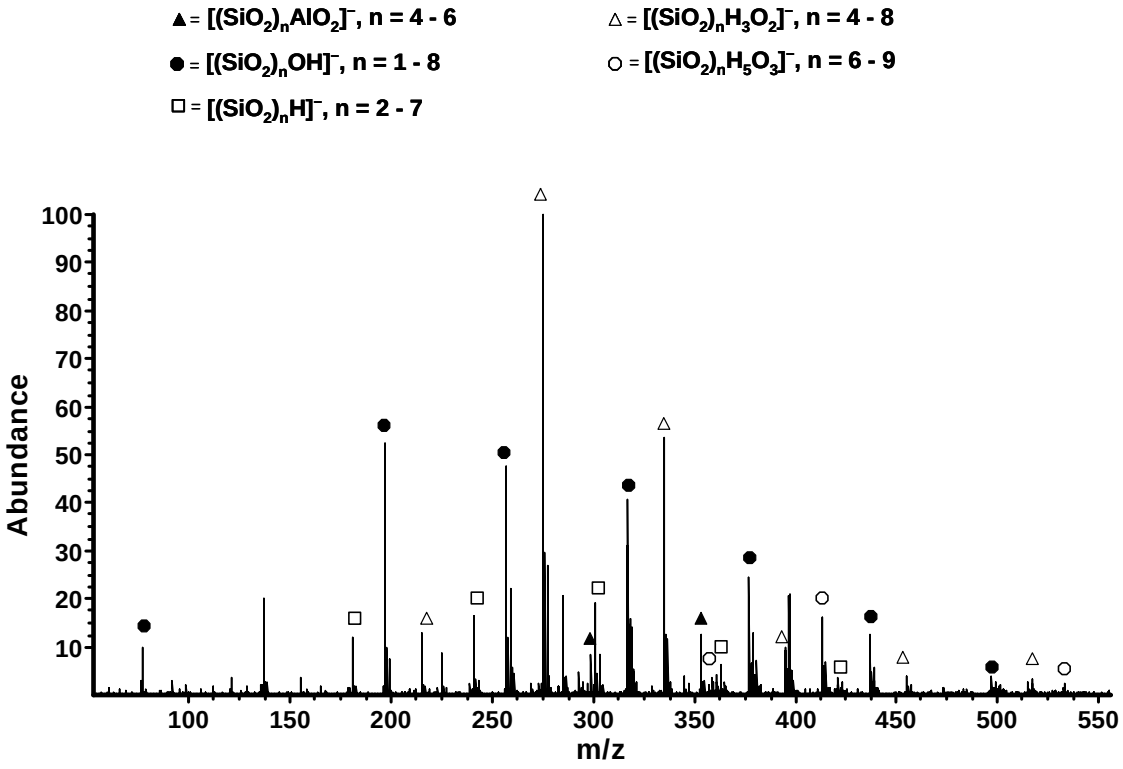

Figure 2. Mass spectrum for solvent-modified beta zeolite sample

Quantitative Stereology of Porous 95/5 Lead Zirconate Titanate (PZT)

D.F. Susan, A.C. Kilgo, C.S. Watson, R.H. Moore, B.A. Tuttle

Motivation: Porous 95/5 lead zirconate titanate (PZT) has a complex microstructure containing the following features (Figure 1): PZT grains, ferroelectric domains within the PZT grains, "intrinsic" (sintering) porosity, second phase particles such as zirconia (ZrO2), "extrinsic" porosity, and other defects. To produce extrinsic pores, polymer spheres (PMMA or polystyrene) are added to the green body and burned out during sintering to reduce the density. The amount and morphology of pores and other constituents have important effects on mechanical and electrical properties. In this study, quantitative image analysis (QIA) techniques were used to characterize the structure of PZT materials. The parameters analyzed included PZT grain size, volume percent of intrinsic and extrinsic porosity, and pore size distribution. The QIA results show good agreement with independent density and particle size measurements.

Accomplishment: Figure 2 displays results of extrinsic porosity measurements. PMMA pore-former was added at two different loading levels of 0.9 wt. % and 1.38 wt. %, corresponding to theoretical volume percent levels of ~5.8% and ~8.8%, respectively. With image analysis, it was possible to distinguish between these two extrinsic porosity levels. Also, when polystyrene (PS) is added (with slightly lower density than PMMA) on an equivalent weight percent basis, a slightly higher porosity volume percent is obtained (Figure 2). Density can be estimated based on the combined amounts of intrinsic and extrinsic porosity and fairly good agreement was found between density values calculated from QIA data and results obtained by bulk density measurements.

Stereology techniques were used to determine pore size distributions in samples with different pore formers. Figure 3 shows examples of pore-former size distributions obtained by laser scattering on two different powders. Laser scattering results were compared with pore sizes obtained by image analysis of final sintered ceramics to show the amount of pore shrinkage during sintering (Figure 3).

Since the pores are spherical, the Schwartz-Saltykov technique was performed to correct the raw data for 2-D sectioning effects [1-4]. Figure 4 summarizes the initial pore-former size and the final sintered pore sizes by comparing the histogram modes from materials with five different pore-formers. The results indicate pore shrinkage during sintering and the amount of pore shrinkage compares fairly well with the predicted value based on overall density measurements.

Significance: Prior to processing PZT materials, the ceramic powder and pore-former amounts and size distributions can be characterized using image analysis and other techniques. However, predicting the final morphology of porous PZT materials based on the starting powders is not straightforward due to complex changes in the microstructure during sintering. A detailed understanding of pore content and pore-size distributions is important since these parameters may affect mechanical and electrical properties and failure modes in PZT. The results of this study, considering the inhomogeneity of the microstructure and the limited sampling of polished cross-sections, show the usefulness of image analysis techniques for understanding processing-microstructure relationships in complex PZT materials.

Contact: Donald Susan, Materials Characterization Dept., 1822
Phone: (505) 284-4951
Fax: (505) 844-2974
Email: dfsusan@sandia.gov

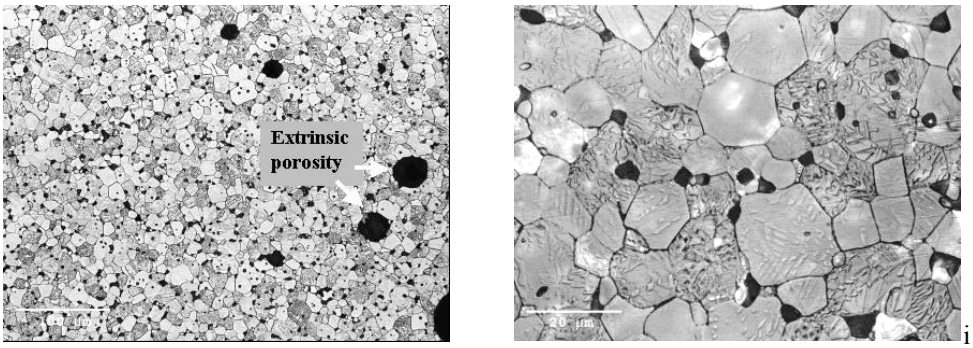

(a) (b)

Figure 1.(a) Etched microstructure of PZT with extrinsic pores (original magnification 100x). (b) Higher magnification image of grain structure and intrinsic porosity. Sample was more deeply etched to show domain structure within the grains (original magnification 1000 times).

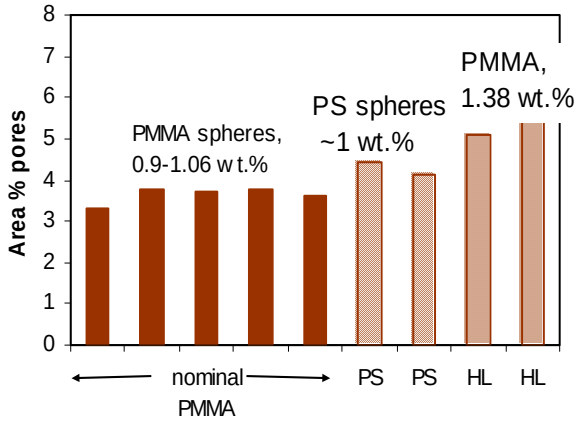

Figure 2. Extrinsic porosity content in PZT with different processing conditions.

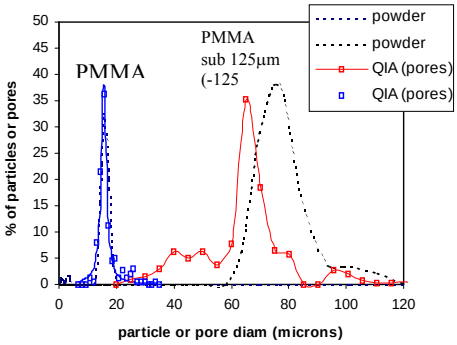

Figure 3. Pore size distributions obtained by image analysis (with stereological correction for sectioning effects) and corresponding pore-former distributions obtained with laser diffraction particle size analyzer.

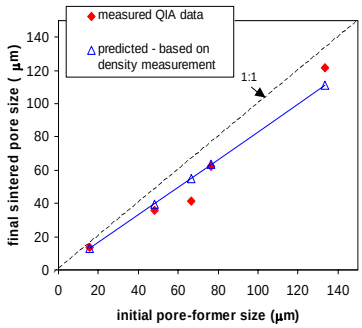

Figure 4. Summary of initial pore-former and final sintered pore sizes (data points represent histogram modes) for PZT materials produced with five different pore-formers.

Analyzing Spectral Images by Maximizing Spatial Simplicity

M. R. Keenan, P. G. Kotula

Motivation: Several full-spectrum imaging techniques have been introduced in recent years that promise to provide rapid and comprehensive chemical characterization of complex samples. These new spectroscopic imaging systems enable the collection of a complete spectrum at each point in a 1-, 2- or 3-dimensional spatial array. One of the remaining obstacles to adopting these techniques for routine use is the difficulty of reducing the vast quantities of raw spectral data to meaningful chemical information. Multivariate factor analysis techniques have proven effective for extracting the essential chemical information from high dimensional data sets into a limited number of components that describe the spectral characteristics and spatial distributions of the chemical species comprising the sample. It is well known, however, that factor-based methods suffer from a "rotational ambiguity", that is, there are an infinite number of factor models that will describe the data equally well. The key to deriving easily interpretable components is to constrain the factor solutions to conform to physical reality. Alternating Least Squares-based Multivariate Curve Resolution (MCR-ALS), for instance, may force spectra and concentrations to be non-negative. There are many cases, however, in which these constraints are not effective and where alternative approaches may provide new analytical insights.

Accomplishment: Principal Component Analysis (PCA), used either by itself or to preprocess data, is the most ubiquitous tool of factor analysis. The constraints imposed by PCA are that the spectral and concentration factors must contain orthogonal components and that the components serially maximize the variance in the data that each accounts for. Neither constraint has any basis in physical reality; thus, the factors obtained via PCA are abstract and not easily interpreted. Figure 1 shows a simple sample consisting of six different types of wires embedded in an epoxy block. This sample was imaged by energy dispersive X-ray spectroscopy (EDS) and the concentration maps derived from PCA are shown in Figure 2. These results are quite complex and no simple picture of the composition emerges either in terms of elemental distributions or alloys. We have discovered that by "rotating" the spatial and spectral component vectors, we can relax the orthogonality constraint in either the spectral or spatial dimension. While pure spectral components are rarely orthogonal, it is often the case that samples are approximately orthogonal in a spatial sense. A sample consisting of spatially discrete chemical phases, for instance, would fall in this category. Figure 3 shows the composition maps for the wires example after rotating the corresponding vectors in a way designed to maximize the simplicity of the spatial representation. In contrast to PCA, each set of wires is clearly separated by alloy, and an examination of the corresponding pure-component spectra (not shown) allows a quantitative identification of each alloy.

Significance: Many spectroscopic techniques involve spectral pure components that are highly overlapped or entail small signals superimposed on large backgrounds. In these cases, standard PCA and MCR-ALS analyses yield less than satisfactory results. The approach based on maximizing the spatial simplicity of the concentration vectors obtained via PCA solves this problem for the commonly encountered class of samples consisting of spatially discrete chemical phases. Excellent results have been achieved by applying this new algorithm to difficult-to-interpret XPS and EELS spectral image data sets.

Contact: Mike Keenan, Chemical & Biological Sensing, Imaging & Analysis Dept., 1812
Phone: (505) 844-2190
Fax: (505) 844-2974
Email: mrkeena@sandia.gov

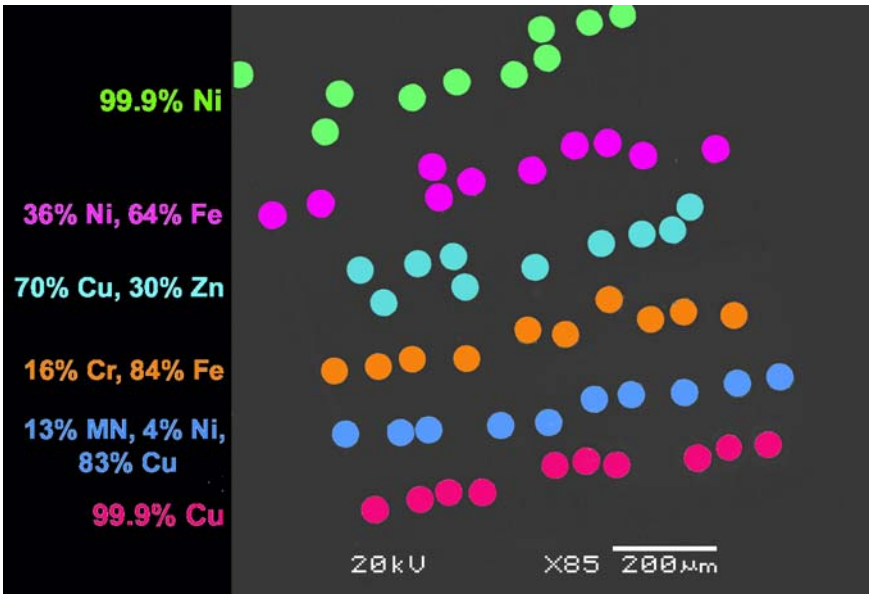

Figure 1. Composition key for an EDS data set in which 6 different alloy wires are embedded in an epoxy block.

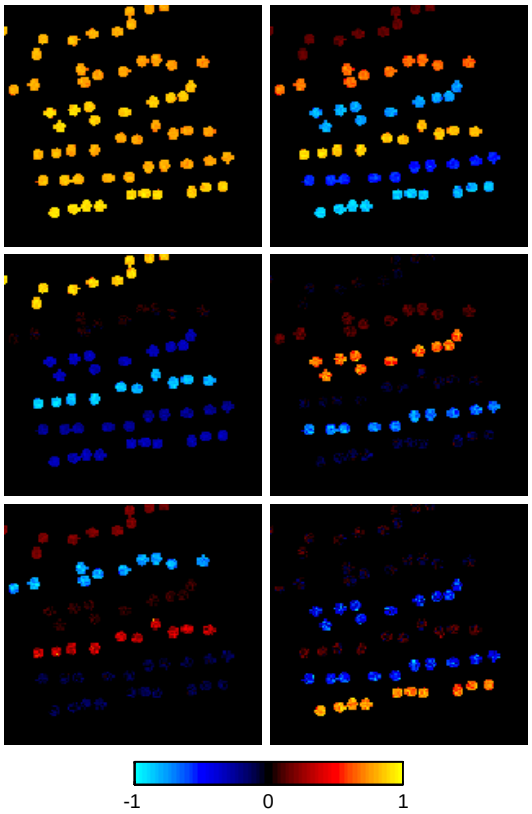

Figure 2. Normalized score images from a principal component analysis of the wires data set

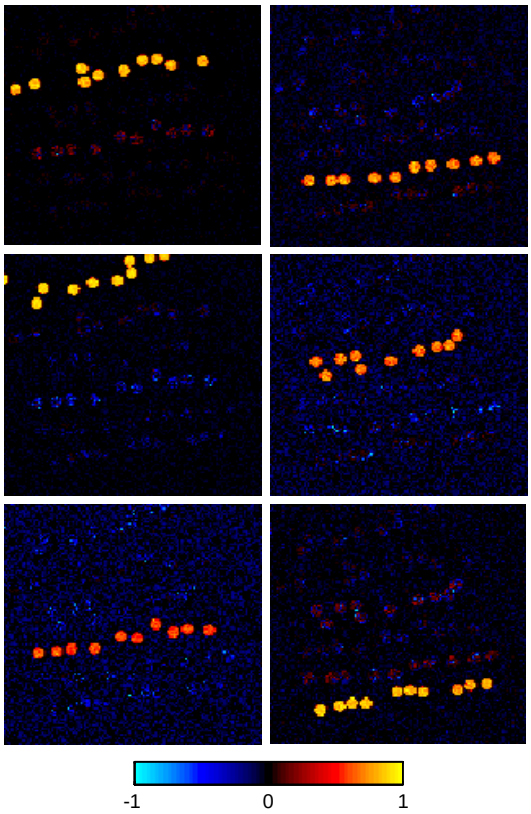

Figure 3. Composition maps obtained by maximizing the spatial simplicity of the score images in Figure 2.

Data Compression Methods for the Analysis of Hyperspectral Images

D.M. Haaland, M. R. Keenan, J.A. Timlin, M.B. Sinclair

Motivation: Hyperspectral imaging is an important new analytical tool where a full spectrum is obtained at each pixel in a 2D or 3D image. Almost any type of analytical spectroscopy can be adapted to spectral imaging. Multivariate analysis methods known as multivariate curve resolution (MCR) are used to greatly enhance the information that can be obtained from the spectral images. For example, MCR can be applied to a spectral image to obtain the pure component spectra from all spectrally active species in the image and can yield relative concentration maps even for those components for which we have no a priori knowledge. However, the hyperspectral imaging systems can generate enormous quantities of data (many gigabytes) that can rapidly overwhelm modern laboratory PCs. Therefore, efficient methods of data compression are required to be able to handle these large data sets in reasonable times.

Accomplishment: We have developed and explored spatial and spectral data compression methods applied to the hyperspectral images and have implemented the MCR algorithms to operate directly on the compressed data. Principal component spectral compression and wavelet spatial compression have been implemented in order to compress the spectral images to manageable sizes. We have demonstrated total data compressions approaching factors of 200,000 without loss of spectral or spatial resolution. Data compressions of this magnitude coupled with efficient programming techniques have greatly improved analysis speed so that computation times are limited primarily by the time required to read the data. The data compression also serves to dramatically reduce core memory and data storage requirements. When MCR is applied to the compressed data, pure spectra of each spectral component in the image are derived from the spectral images. Once these pure-component spectra are available, we project the original data into the space spanned by the pure component spectra using classical least squares predictions to obtain component concentration maps at the high spatial resolution of the original data. Our group has applied these compression techniques to a wide variety of hyperspectral image data, but they are demonstrated here for hyperspectral images obtained from microarray samples (see Figure 1). Microarray technology is a relatively rapid, high-throughput method that allows the analyst to simultaneously monitor relative expression levels for thousands of genes from cells in two different states. As can be seen in Figure 1, the high spatial compression with wavelets has caused the loss of spatial resolution required to quantitatively determine gene expression levels for individual spots (i.e, genes). Yet the MCR-derived concentration maps obtained from the compressed results are indistinguishable from those obtained from the full uncompressed data. The data presented in Figure 2 further demonstrate that the Cy3 and Cy5 fluorophore concentrations that are related to gene expression levels are comparable independent of whether MCR is applied to the data compressed at the highest levels (>190,000x) or to the uncompressed data.

Significance: Hyperspectral image data sizes have outstripped our ability to analyze the data directly. We have shown that we can accomplish rapid multivariate data analysis on data that is highly compressed in both the spectral and spatial dimensions. Thus, we can now analyze spectral images of multiple GB in size rapidly without loss of information content.

Contact: David Haaland, Chemical & Biological Sensing, Imaging and Analysis Dept., 1812
Phone: (505) 844-5292
Fax: (505) 844-2974
Email: dmhaala@sandia.gov

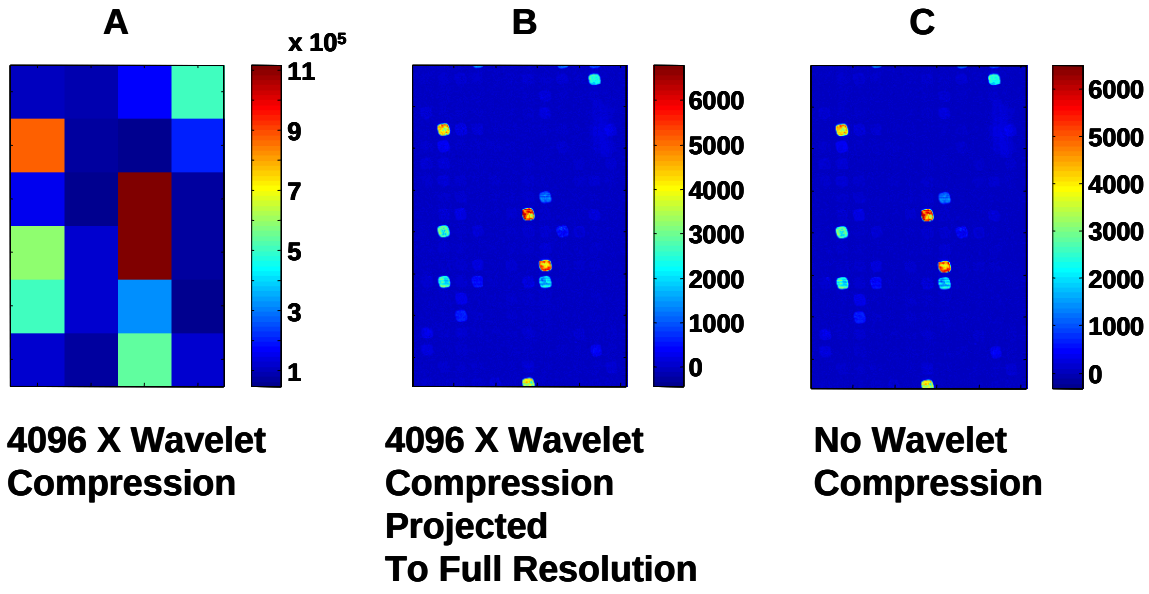

Figure 1. Concentration maps of the Cy5 fluorophore: A) MCR results applied to the data compressed to 24 spectra by 4096x wavelet compression (total spectral and spatial compression is >190,000x). B) Concentration Cy5 map after projecting the MCR pure-component spectra obtained from the compressed data onto the original uncompressed image spectra. C) Comparable Cy5 map obtained from MCR applied to the original uncompressed data.

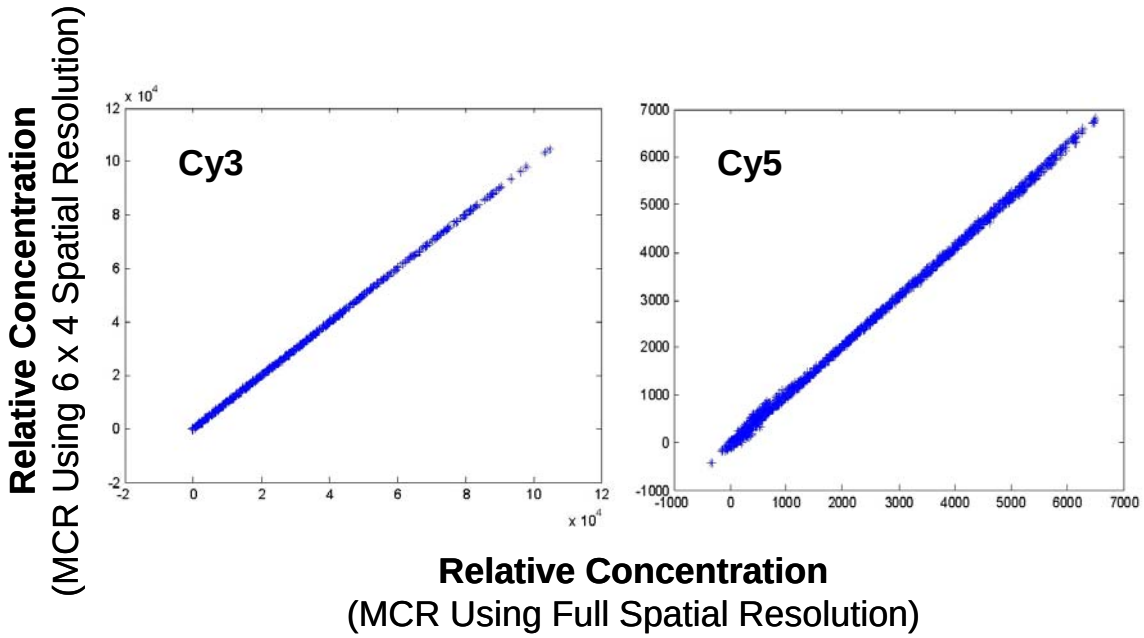

Figure 2. Comparison of the estimated Cy3 and Cy5 concentrations after applying MCR to the fully compressed data or the uncompressed data.

Hyperspectral Microarray Scanner

M.B. Sinclair, J.A. Timlin, D.M. Haaland, M. Werner-Washburne

Motivation: Changes in gene expression, resulting in the production of protein, are significant components of an organism's response to factors such as environmental perturbations or disease. With the advent of DNA microarray technology, gene expression measurements can be performed in a highly parallel fashion, leading to greatly increased experimental throughput. However, this technology is still relatively young and there are many aspects that can be improved. For example, current generation microarray scanners measure the band-integrated emission corresponding to each of the fluorescent tags utilized. This measurement approach restricts to two the number tags that can be used in a single experiment. In addition, due to the univariate nature of the measurement, there is no reliable mechanism to determine if the recorded data have been corrupted by extraneous emission sources.

A hyperspectral microarray scanner overcomes these limitations by measuring the entire emission spectrum for each pixel of the microarray. Full spectral information, when combined with multivariate data exploitation, allows for accurate determination of the contributions of multiple, spectrally overlapping tags. This leads directly to the ability to probe more than two tags, using a single laser, within a single scan. In addition, the multivariate analysis can identify and remove all extraneous emission from the array data, even in cases where the extraneous emission exhibits large spatial variations (for example, emissions from spot - localized impurities).

Accomplishment: We have developed and applied a hyperspectral microarray scanner (see Figure 1) that records the entire emission spectrum (490 – 900 nm) for each pixel of the microarray. Multiple laser sources may be coupled to the instrument for excitation of a wide range of fluorescent tags. The hyperspectral scanner features the use of line-focused laser illumination and "push broom" data acquisition for fast scanning. Sensitivity at high data rates is maximized through the use of an electron multiplying CCD detector array. The scanner is currently capable of sustained acquisition at a rate of ~1.5 Mbytes/s, and will soon be upgraded with a faster detector allowing a tenfold increase in the acquisition rate.

Significance: Application of the new scanner to microarray analysis has emphatically demonstrated the benefits of the hyperspectral approach. To illustrate, the results obtained from one scan are shown in Figure 2. Extraneous emission from the glass microarray substrate and a spot-localized impurity is clearly observed, along with the expected emission from the Cy3 and Cy5 fluorescent tags. Conventional scanners are not able to distinguish this spectrally overlapping, spot-localized emission, and would produce erroneous results for this microarray.
Recent experiments have also demonstrated the potential for increased experimental throughput, by separating the contributions of four spectrally overlapping tags, recorded with a single scan. In addition, the scanner has been used to characterize Green Fluorescent Protein (GFP) expression of yeast cells. In this case, the hyperspectral advantage enables the quantitative observation of the GFP emission, even in the presence of strong, overlapping autofluorescence from the cells and growth medium.

Contact: Mike Sinclair, Microsystems Materials, Tribology, & Technology Dept., 1851
Phone: (505) 8445506
Fax: (505) 844-9781
Email: mbsincl@sandia.gov

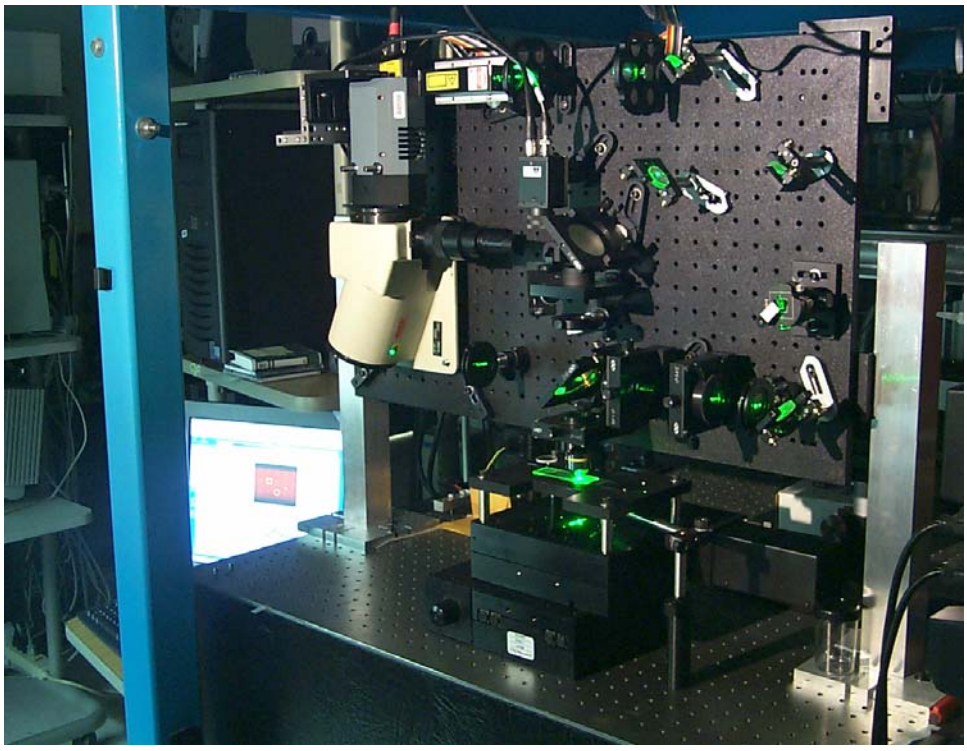

Figure 1. A photograph of the hyperspectral microarray scanner.

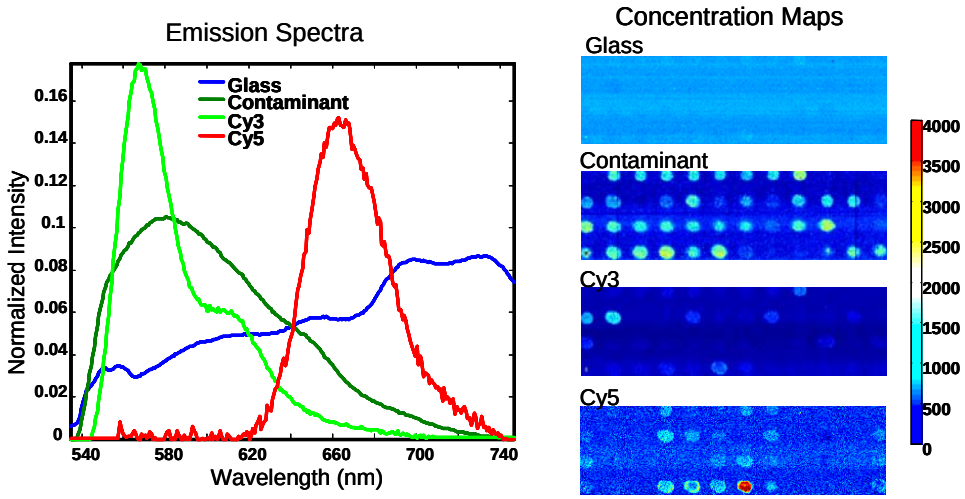

Figure 2. The emission spectra extracted from a hyperspectral scan of a portion of a DNA microarray. (left) In addition to the expected Cy3 and Cy5 emission, significant emission is observed from the glass substrate and a spot-localized impurity. The concentration maps obtained for each of the emitting species. (right)

Multivariate Analysis of Vibrational Spectra Applied to Materials Processing, Aging and Discrimination

D. R. Tallant, M. J. Garcia, R. L. Simpson

Motivation: Vibrational spectra from infrared (IR) and Raman spectroscopy are rich in features (and therefore in information content) and are well known for their ability to characterize molecular species. The downside of the complexity of vibrational spectra is that the spectroscopic consequences of low level chemical changes are often obscured by dominant, unchanging features. A data manipulation technique that enhances the ability to detect subtle variations in vibrational spectra provides a means to discriminate between compositionally similar materials, to identify and quantify trends in the reactions associated with curing of polymers and to identify aging reactions in polymers.

Multivariate spectral analysis focuses on variations between spectra and, thus, makes subtle differences apparent. It uses matrix regression techniques to "reduce the dimensionality" of large sets of spectra. In essence, these techniques generate a set of "factors" (which can be thought as components of the spectra), which, suitably scaled by "scores" and summed, reproduce all the spectra in the set. A score is the relative contribution of a factor to a spectrum. Thus, there is one set of factors for the entire set of spectra, and a score for each factor and each spectrum. Examination of a factor reveals the chemical species associated with it. The factor's scores chart the changes, from spectrum to spectrum, in the amount of the component associated with the factor.

Accomplishment: We have applied multivariate spectral analysis of vibrational spectra to materials of interest to both weapons and other applications. We have used it to investigate the rate and mechanism of curing of polymers (especially the new removable formulations) being developed for adhesive and encapsulant applications and to study gel formulations intended for use in a new type of capacitor. We have also identified the rates and mechanisms of chemical reactions leading to strength degradation in nylon fibers used in parachute yarn.

A simple example of the use of multivariate spectral techniques is the identification of compositional differences in two lots of InGaAlAs in an electrooptic device. One lot (Ew1044) performed well and the other (Ew1092) poorly. Multiple Raman spectra were obtained of well layers from the two lots, and the spectra were analyzed by multivariate techniques. The scores from factor 3, plotted versus factor 1 (which corresponds to the average of the spectra) in Figure 1, show the most discrimination between the two lots. Lot Ew1092 has consistently higher factor 3 scores. Factor 1 (again, the average of the spectra) and factor 3 are shown in Figure 2. The negative-pointing bands of factor 3 correspond to a deficiency in GaAs and AlAs vibrations in the spectra. Thus, the higher factor 3 scores for lot Ew1092 (Figure 1) indicate that it is relatively deficient in Ga and Al. From the actual intensities of the factors, we determined that the difference in Ga and Al contents between the two InGaAlAs lots is on the order of a few percent. Subsequent modeling confirmed that this compositional variation might result in the observed performance differences.

Significance: The enhanced understanding of polymer curing from this work has improved the formulation and processing of materials intended for weapons applications. Enhanced understanding of nylon degradation is improving our ability to predict aging and its effect on the strength of nylon yarns in stockpile.

Contact: Dave Tallant, Materials Characterization Dept., 01822
Phone: (505) 844-3629
Fax: (505) 844-9781
Email: drtalla@sandia.gov

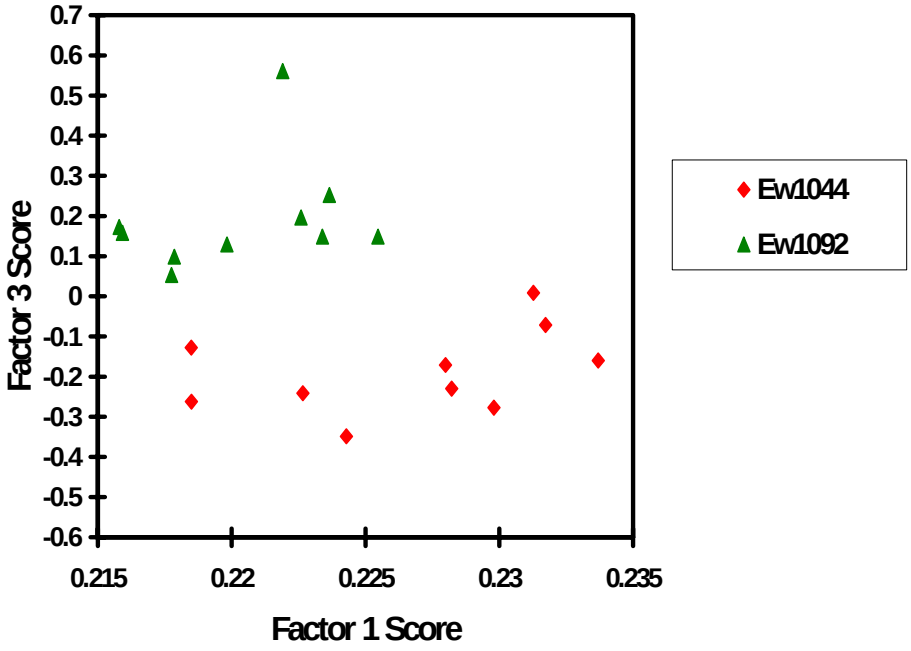

Figure 1. Factor 3 Scores versus Factor 1 Scores from multivariate analysis of Raman spectra from InGaAlAs well layers

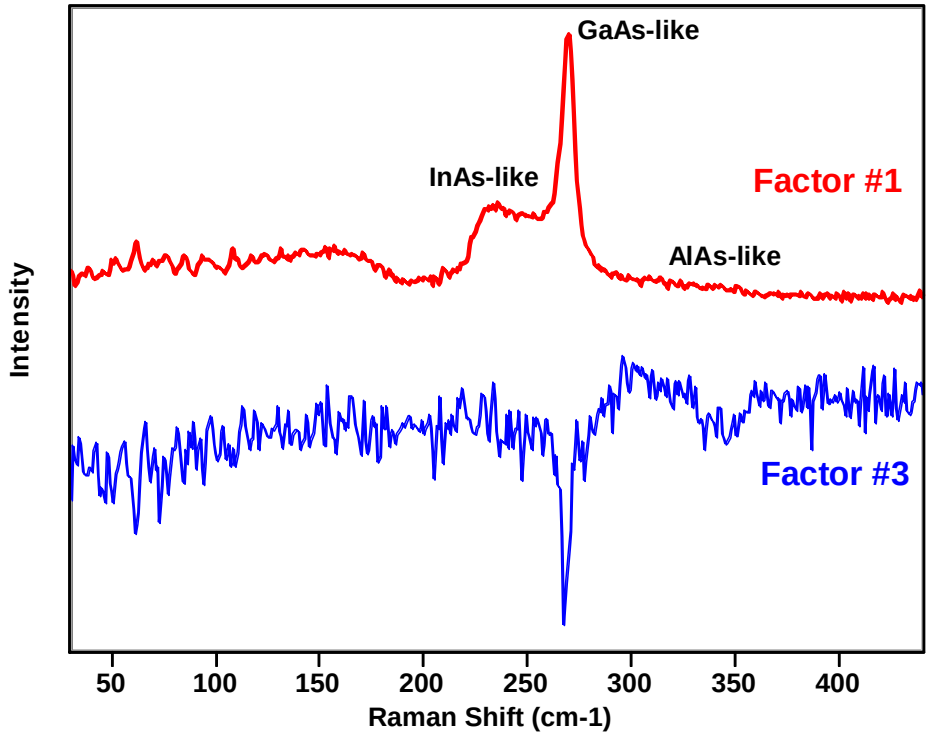

Figure 2. Factors 1 and 3 from multivariate analysis of Raman spectra from InGaAlAs well layers

Multivariate Analysis of X-ray Photoelectron Images

D. E. Peebles, J. A. Ohlhausen, M. R. Keenan, P. G. Kotula

Motivation: Recent generation X-ray photoelectron spectroscopy (XPS) instruments have significantly advanced the capability of rapidly and routinely acquiring images of the variations in surface composition and chemical state. The extraction of photoelectron spectra from a series of images at selected binding energies opens up the possibility of creating spectral image data sets. Processing the spectral image data sets with multivariate statistical analysis (MSA) provides the ability to extract the most important information from this large data set rapidly and without operator bias.

Accomplishment: The sample used for this demonstration was a Cu transmission electron microscopy (TEM) grid pressed into a piece of Al foil. XPS images were acquired on a Kratos AXIS Ultra photoelectron spectrometer using the new delay line detector at the Kratos Applications Laboratory (Manchester, UK). Images were acquired from the sample at binding energy increments of 0.15 eV from 83.5 eV to 70 eV, for a total of 91 images. This binding energy range covers the overlapping Cu 3p and Al 2p spectral lines. Each image was acquired from the same 200 μm area of the sample at an acquisition time of 3 minutes each with an analyzer resolution of 40 eV.

Figure 1 shows the resulting peak-minus-background images for peak binding energies of 78.1 eV (red) and 73.0 eV (green), using a background image at 70.0 eV for both. These peak binding energies correspond roughly to the Cu $3p_{1/2}$ and Al 2p (metal) peaks. The image shows the Cu grid and Al background, but the contrast is weak and the line separation is poor. Figure 1 also shows the spectra taken at a single pixel in the Cu grid (red) and one in the background Al (green). The spectra have a very poor signal-to-noise ratio and do not clearly separate the peak contributions. In the figure, the vertical lines show the energies used for the peak images for each elemental region.

The individual images taken at each energy were combined into a spectral image and processed with a new MSA algorithm based on maximizing spatial simplicity, as described elsewhere in these research briefs [1]. The results are shown in Figure 2. The image is now clearly resolved into Cu (red) and Al (green) components, with excellent image contrast. The resulting component spectra for Cu (red) and Al (green) show an amazing improvement in the signal-to-noise ratio and in the ability to separate out the peak contributions. The Cu spectrum clearly shows both of the unresolved Cu $3p_{3/2}$ and $3p_{1/2}$ contributions, while the Al spectrum clearly shows contributions from the surface oxide and the underlying Al metal peaks.

Significance: The application of MSA to spectral imaging has been shown to be extremely successful at enhancing component image distributions, clarifying co-varying species, and finding small contributions that may or may not have been expected. This work shows that all of these advantages are also observed for XPS spectral imaging. However, because of the slow data acquisition times typical for XPS, this technique also shows an enormous enhancement of signal-to-noise in the component spectra and spatial resolution and contrast in the images. These advantages allow the rapid acquisition of spectra from x-ray or contamination sensitive samples, while still allowing precise determination of chemical state and quantitative composition information.

[1] M. R. Keenan and P. G. Kotula, "Analyzing Spectral Images by Maximizing Spatial Simplicity," these Research Briefs.

Contact: Diane Peebles, Materials Characterization Dept., 1822
Phone: (505) 845-8087
Fax: (505) 844-7425
Email: depeebl@sandia.gov

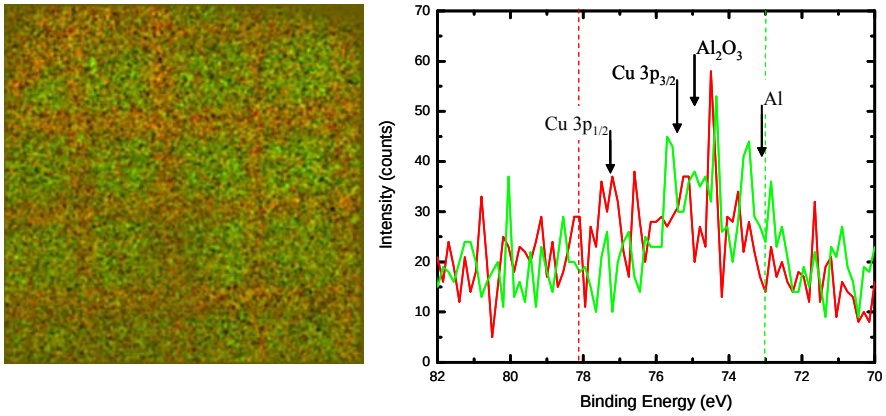

Figure 1. Peak-to-background image overlay and single pixel spectra of the Cu grid (red) and the Al foil background (green)

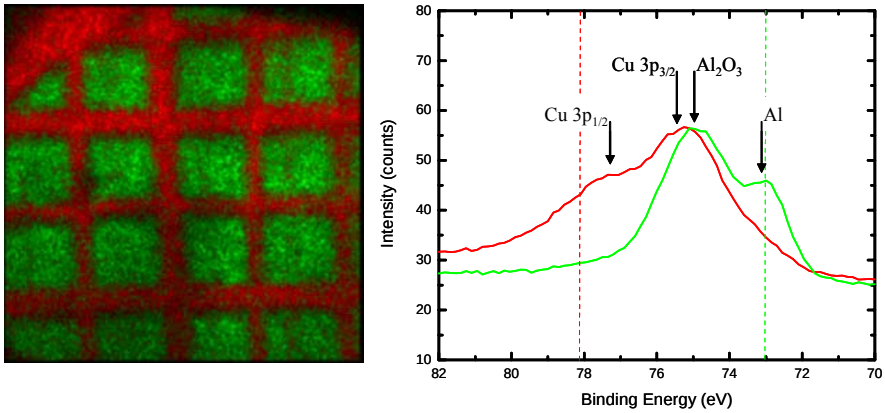

Figure 2. Multivariate component image overlay and component spectra of the Cu grid (red) and the Al foil background (green).

Routine Application of Multivariate Statistical Techniques to Time-Of-Flight Secondary Ion Mass Spectrometry

J. A. Ohlhausen, M. R. Keenan, P. G. Kotula, D. E. Peebles

Motivation: Time-of-Flight Secondary Ion Mass Spectrometry (TOF-SIMS) by its parallel nature, generates complex and very large datasets quickly and easily. An example of such a large dataset is a spectral image where a complete spectrum is collected for each pixel. Unfortunately, the large size of the data matrix involved makes it difficult to correlate the many signals present in the data using traditional techniques. Simple mass window analysis provides useful information, but suffers from signal-to-noise limitations and the possibility of confounding information from multiple materials phases. For example, a surface containing spatially resolved organic species can be difficult to image due to the similar nature of the fragments contained within each material's spectral fingerprint. Consequently, unique or parent ions must be used to identify the different species present. Correlation of single mass images can be cumbersome and some correlated peaks can easily be missed. Ideally, the complete spectral image would be used to provide a comprehensive materials characterization based on full spectral signatures.

Accomplishment: We have successfully applied Sandia's multivariate statistical analysis toolkit AXSIA (Automated eXpert Spectral Image Analysis) to TOF-SIMS. These algorithms are routinely used to aid in interpretation and analysis of simple to complex datasets. Two examples illustrate the benefits of using this technique for routine analysis. Figure 1 shows the results from the analysis of a Sn/Pb eutectic metallization. Expected Sn and Pb components are present and shown as red and blue respectively in Figure 1. Size and distribution are easily seen in this analysis. Unexpected phases were also automatically discovered. The cyan component (Sn +alkali contaminants) was found in one spot, so is probably a contamination particle of little interest. On the other hand, a collection of smaller particles shown as yellow in Figure 1 are primarily comprised of Cu and were not expected. This discovery would have been difficult to find without the aid of the multivariate technique.

In Figure 2, the positive ion analysis of a silicon wafer with unknown particulate contamination is seen. From this raw data, the identity and location of the particles is still unknown. A lengthy and difficult manual interrogation is necessary to identify the particles.

With the aid of AXSIA the location, size and identity of the particles is easily seen. Figure 3 shows the particle components from both positive and negative secondary ion AXSIA analyses. Using these plots, complete particle identification was formulated within a couple of minutes.

Significance: Because AXSIA is capable of separating unique chemical signatures in complex datasets quickly, the time it takes to generate a complete answer is much less than using conventional techniques. In addition, the full spectral results provide a more complete answer. Unambiguous answers and full spectral separation leads to efficient, complete results for both simple and complex datasets.

Contact: Tony Ohlhausen, Materials Characterization Dept., 1822
Phone: (505) 845-9510
Fax: (505) 844-77425
Email: jaohlha@sandia.gov

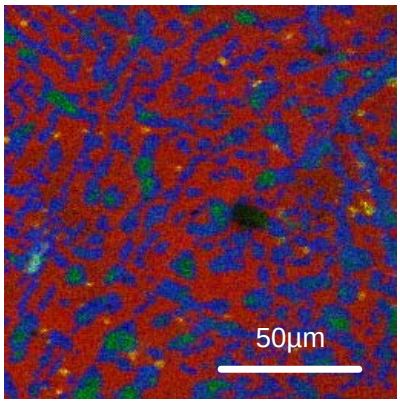

Sn/Pb Eutectic Analysis

Red: Sn

Blue: Pb + PbO

Green: Pb + Hydrocarbons

Cyan: Sn + Alkali Contaminants

Yellow: Cu

Figure 1. AXSIA TOF-SIMS analysis of Sn/Pb Eutectic showing sensitivity to small features such as the Cu inclusions.

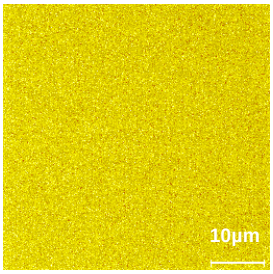

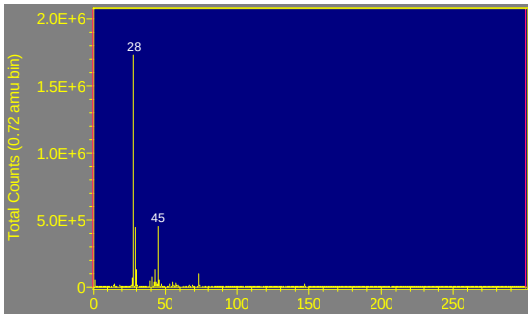

Positive Total Ion Image **Positive Total Ion Spectrum**

Figure 2. Particle Analysis: Raw TOF-SIMS positive secondary ion total ion image and spectrum. Note that the particles are not visible in the image or the spectrum.

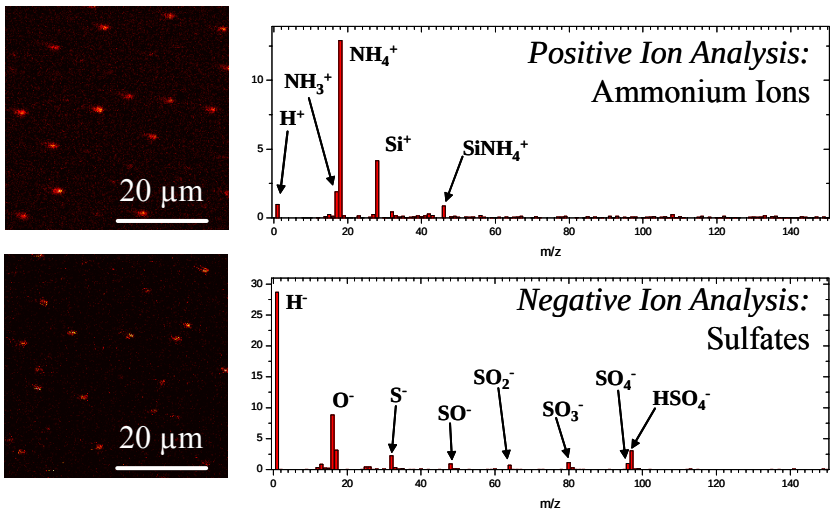

Figure 3. Particle Analysis: AXSIA TOF-SIMS positive and negative secondary ion analysis providing unambiguous separation and identification of the particles.

Tomographic Spectral Imaging: Microanalysis in 3D

P.G. Kotula, M.R. Keenan, J.R. Michael

Motivation: Microanalysis, or the chemical characterization of small features in microstructures, has typically been limited to 2D or just the surface of a material. Quite often, however, there is chemical information in the third dimension that is also of interest but inaccessible by conventional analysis approaches. In this work, 3D chemical characterization has been combined with spectral imaging and multivariate statistical analysis with the result being a comprehensive and unbiased chemical analysis of a volume of material at sub-micron resolution.

Accomplishment: We present the results of comprehensive 3D microanalysis performed via serial sectioning in the focused ion-beam (FIB) tool combined with spectral imaging for each slice–tomographic spectral imaging (TSI). The entire 4D (*x, y, z, E*) spectral image data set was automatically analyzed utilizing a modified version of our award winning and patented Automated eXpert Spectral Image Analysis (AXSIA) software based on multivariate curve resolution [1,2]. The result was a compact, easily interpreted solution that, as with previous applications of the technique [2], is far more straightforward to interpret than the raw data itself or by using other conventional approaches.

The TSIs were acquired in a FEI DB-235 focused ion-beam tool (FIB)/scanning electron microscope (SEM) equipped with an energy-dispersive x-ray spectrometer and spectral imaging hardware. Firstly, a trench was milled to expose the initial analysis surface, then an additional trench was milled perpendicular to the first allowing the x-ray detector to 'see' the analysis surface. In addition, fiducial markers were milled into the original surface for slice-to-slice alignment. In serial-sectioning fashion then, each sub-micron slice with the FIB revealed another analysis surface that was then probed with the electron beam, with the resultant x-ray spectral image acquired at each slice.

A micron-sized corrosion product on an accelerated aging specimen was analyzed. The sample was a gold- and nickel-plated copper coupon that was subjected to a corrosive environment resulting in localized sulfide blooms on the specimen surface. TSI analysis was made from a region including one such bloom. The data set analyzed was 128x128 pixels x10 slices by 512 energy channels per pixel. AXSIA automatically identified six components shown together in Figures 1a and b in two different views. Figures 1c and d show the spatial relationship between the unexpected contaminant (silicon oxide) and resulting corrosion product (copper sulfide) while figures 1e and f show just the gold film and the pinhole that allowed localized corrosion to proceed.

Significance: The capability described above illustrates the power of comprehensive 3D microanalysis (TSI), combined with advanced data analysis algorithms (AXSIA). This approach successfully found that an unexpected impurity from processing was the locus of corrosion in an accelerated aging environment. This unbiased approach to microanalysis will more generally impact our understanding of aging mechanisms in materials.

[1] M.R. Keenan and P.G. Kotula, US Patent #6584413

[2] P.G. Kotula, M.R. Keenan and J.R. Michael, *Microsc. Microanal.* 9[1] (2003)1-17.

Contact: Paul Kotula, Materials Characterization Dept., 1822
Phone: (505) 844-8947
Fax: (505) 844-2974
Email: pgkotul@sandia.gov

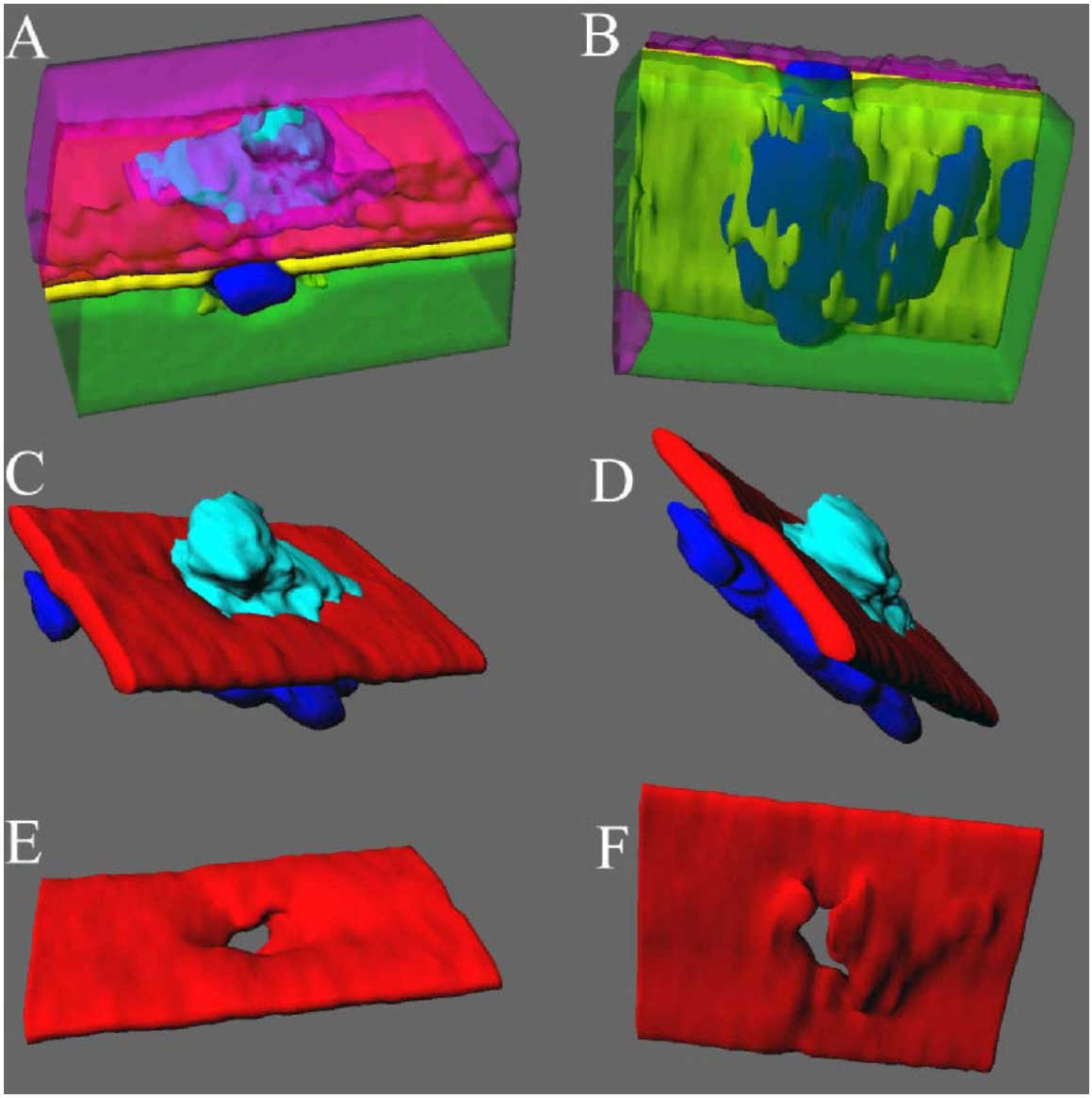

Figure 1. Three dimensional component images from the automated spectral image analysis. Gold is red; copper is translucent green; the unexpected silicon oxide is blue; the copper sulfide corrosion product is cyan; platinum (from the FIB system) is translucent magenta; and nickel is yellow. Figures A and B, show all of the components together while in C and D just the silicon oxide, gold and copper sulfide component images are shown. Figures E and F, show just the gold component image and the pinhole that allowed rapid corrosion to occur.

Aerosol Distribution from Surrogate Nuclear Fuel Rod Sabotage

T. Borek

Motivation: There is international interest in the distribution of aerosolized radioactive species from a shape-charge impact on spent fuel. In the event of a terrorist attack on a spent fuel element, authorities would need to know the most likely dispersal scenario and source term for uranium, plutonium, and fission products. Sandia National Laboratories has the lead test role in this investigation, as part of the International Working Group on Sabotage Concerns of Transport and Storage Casks. This work is funded by both the U.S. DOE and NRC, with additional participation by organizations in Germany, France, and the UK.

Accomplishment: In an effort to quantify spent fuel aerosol particle formation and then model radiological consequences for this scenario, impact experiments were conducted using a surrogate spent fuel element constructed of cerium oxide pellets in Zircaloy 4 tubes. Cerium oxide was selected due to its chemical and physical similarity to uranium and plutonium oxides.

A shape charge was fired at a surrogate fuel element in an aerosol containment vessel (Figure 1). The aerosols generated from the impact were sampled using 3-stage aerosol collectors. The 3-stages of this device represent particles of <4μm, <10μm, and all others. These fractions represent the respirable (deep lung), thoracic, and inhalable portions of the solids dispersed (Figure 2).

After impact, the filters are weighed for solids captured, are then acid-digested, and analyzed by inductively coupled plasma/mass spectrometry. The cerium observed for a typical experiment is shown in Table 1. A majority of the cerium from this test is found in the inhalable fraction collected.

Significance: The success of the surrogate tests conducted to date have lead to the incorporation of surrogate fission product dopants in current tests, with the ultimate goal of testing spent fuel.

Contact: Ted Borek, Materials Characterization Dept., 1822
Phone: (505) 844-7758
Fax: (505) 844-2974
Email: ttborek@sandia.gov

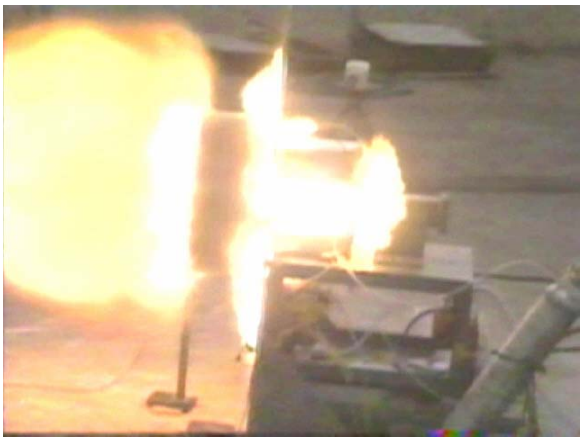

Figure 1. Shape charge detonation in test fixture.

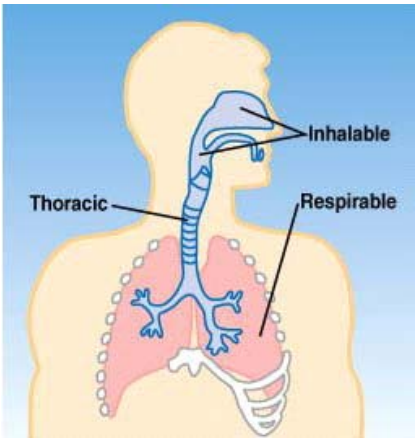

Figure 2. Inhalable, Thoracic, and Respirable Aerosols Deposition

Table 1. Distribution of Cerium on Aerosol Filters

	Respirable	Thoracic	Inhalable	
	Top	Middle	Bottom	Total
	milligrams			
K	2.436	3.364	4.608	10.408
L	3.011	3.84	7.026	13.877
	wt%			
K	23.4	32.3	44.3	
L	21.7	27.7	50.6	

An Ion Mobility Spectrometer Mass Spectrometer for Trace Detection and Identification of Controlled Substances

D. Austin, D. Hunka, C. Rhykerd

Motivation: Ion mobility spectrometry (IMS) is a highly sensitive method for separating and detecting trace components from a complex mixture. Sandia has developed several IMS instruments for such applications as explosive detection at airports and chemical agent detection on the battlefield. Although these instruments exhibit high sensitivity to target molecules, the complex chemical environments of these locations produce numerous interferences, resulting in a high level of false positives and unidentifiable spectral peaks. In order to improve the reliability and selectivity of Sandia's IMS systems, we have been modifying a triple quadrupole mass spectrometer to readily interface with various IMS systems and provide positive chemical identification of the species detected by the IMS. The ideal interface will allow sufficient ion transmission into the mass spectrometer, reduce or prevent ion clustering, and allow the mass spectrometer to operate at high vacuum while the IMS operates at atmospheric pressure. In addition, an ideal interface would be capable of rapid and simple connection to any of Sandia's IMS systems, without disruption of either the ion focusing properties of the interface or the pressure of the mass spectrometer.

Accomplishment: During the first year of this project (FY 2003) we selected and purchased an appropriate mass spectrometer system equipped with all the features needed for compatibility with the interface and the IMS. We performed several SIMION simulations of ion behavior in both the IMS and the interface region in an effort to understand the factors that need to be addressed in the design of the interface. These simulations focused on optimization of the ion optics needed to maximize ion focusing and transmission into the mass spectrometer. We also completed the design of the modifications to the IMS chamber, the IMS detector, and the interface itself. All of the components of the interface either have been or are currently being built, and final assembly of the interface is expected soon. Figures 1 and 2 show renderings of the IMS chamber adaptation and the IMS/MS interface, with the interface shown to the upper left in Figure 1, at the top in Figure 2. Additional electrostatic lenses within the ceramic interface are not visible.

Significance: The design of the interface is such that any of Sandia's IMS systems can readily be connected to the triple quadrupole mass spectrometer. The mass spectrometer has several capabilities, such as tandem MS, that will be useful in identification of a wide range of contaminants and interferents, allowing more reliable and thorough results from IMS instruments. We expect that this instrument will become a resource for the Sandia IMS community for testing and improvement of both current and future ion mobility spectrometers.

Contact: Daniel Austin, Chemical & Biological Sensing, Imaging, and Analysis Dept., 1812
Phone: (505) 284-9852
Fax: (505) 844-2974
Email: deaust@sandia.gov

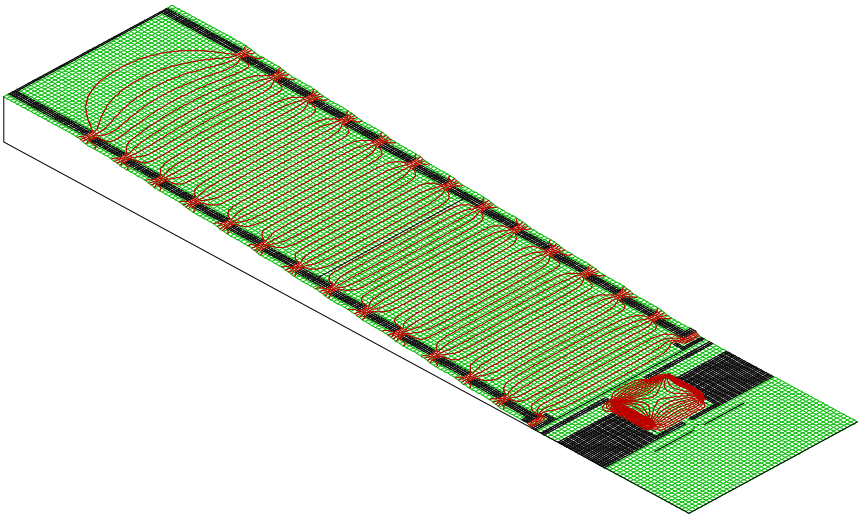

Figure 1. Simulation of ion trajectories in the IMS and interface.

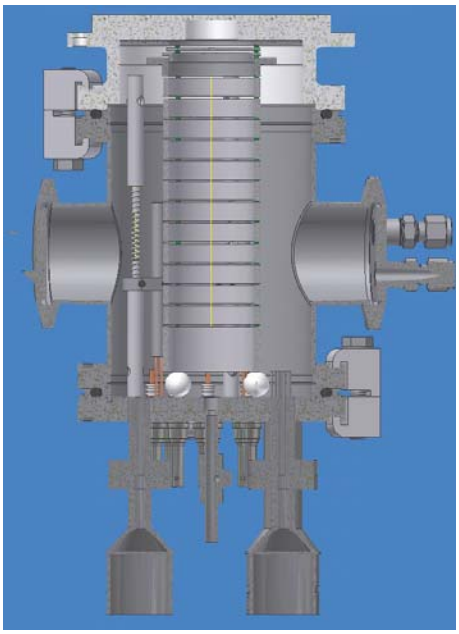

(a)

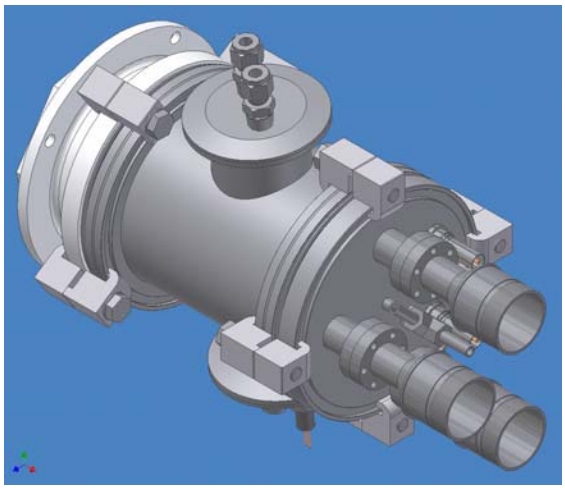

(b)

Figure 2. Design of ion mobility spectrometer and interface to mass spectrometer (a) cross section view (b) isometric view

Indentation Techniques used as a Sensitive Microprobe for Stress

R. Tandon

Motivation: Residual stresses are ubiquitous in brittle materials, their composites, and at and around an interface where one or more brittle material is present. In non-cubic polycrystalline materials, residual stresses exist at the grain boundary level due to a thermal expansion mismatch. Crack path selection through or around the grain is influenced by this stress. In particulate, whisker or fiber composites residual stresses, over ten to hundreds of grains, play a significant role in determining the effectiveness of the reinforcement. At interfaces, stresses may occur over tens of thousands of grains due to elastic and thermal mismatches, and are crucial in determining the practical work of adhesion of the interface, the strength of the adhered layers, and even the wear and friction behavior. For some engineering applications, residual stresses are deliberately introduced in order to strengthen the material and suppress crack initiation. It is therefore evident that characterization of the magnitude and extent of the stress is crucial in understanding the mechanical response of the material, and assessing the reliability of the system.

Accomplishment: We are utilizing indentation with a sharp Vickers indenter and with an axi-symmetric conical indenter to ascertain the magnitude and extent of the stress profiles in materials. Fig. 1a is a schematic of an insulator used in the neutron tube production. The ceramic is an AD96 alumina material with through holes. Two polymer lines (feet) are on the far face, and the far face is bonded to a metal during assembly. The bonding process produces tensile stress in the ceramic. It was postulated that the properties of the polymer influenced the magnitude of the stress. Sharp Vickers' indentations (50N load) were performed on the near face on the ceramic bonded to three different polymeric materials (Materials 1, 2 and 3). The resulting cracks are shown in Figs. 1b-d. In Fig, 1b, the cracks from the indentation in directions parallel and perpendicular to the polymer line are nearly equi-sized, indicating that significant stresses do not develop using Material 1. Fig. 1d (with Material 3) shows the cracks parallel to the polymer feet extending significantly, indicating high tensile stress perpendicular to the line. Material 2 exhibits intermediate stresses. Our results are being used for validating FEA analyses and in material selection. Fig. 2 shows indentations placed at different distances from the center of a metallic via in a LTCC substrate. Cracks close to the via interact strongly with the thermal expansion mismatch stress field, and changes in crack trajectories provide an opportunity to map the stress fields around the via.

Significance: Complete understanding of the stress fields around sharp indentations in a brittle material will allow us to predict the mode of cracking around the site, and the crack trajectories. When the indentation is placed in a material with a prior stress field, either on a surface that possesses a residual stress, or near a dissimilar microstructural feature, the crack patterns are altered. This alteration can be used to map the prior stress state. This stress state along with other material properties serves to validate FEA calculations, as a measure of the impact of processing changes, and as input into reliability analyses.

Contact: Raj Tandon, Ceramic Materials Dept., 1843
Phone: (505) 844-1187
Fax: (505) 844-7910
Email: rtandon@sandia.gov

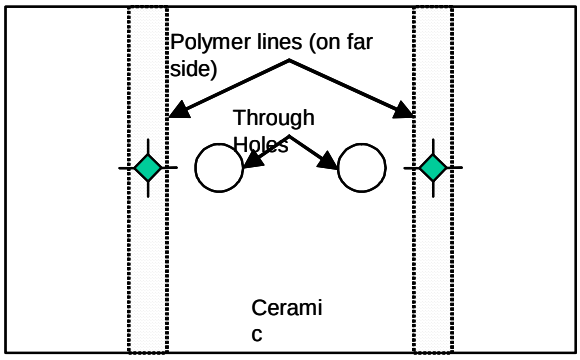

(a)

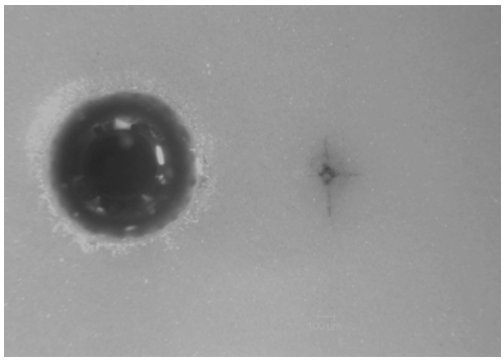

(b) Polymer 1

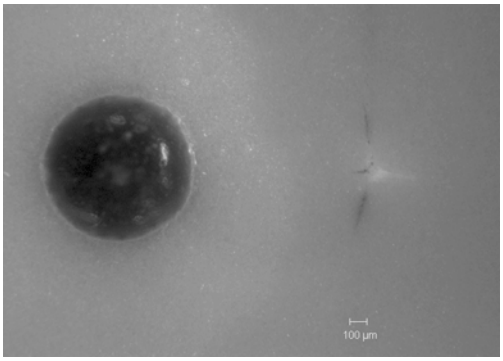

(c) Polymer 2

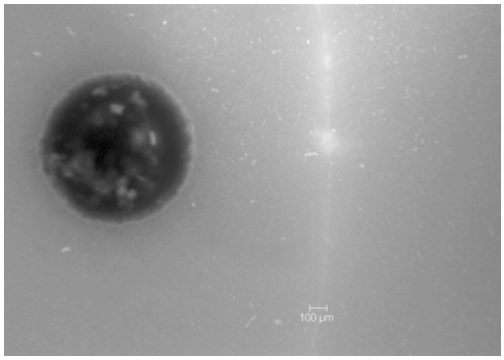

(d) Polymer 3

Figure 1. (a). The schematic of an alumina (AD 96) ceramic substrate with two through holes is shown. The polymer lines are on the far face. Indentations are placed on the ceramic near face, directly above the polymer lines. (b) through (d) show the indentations for three different polymeric materials. Material 3 produces a very severe stress state in the ceramic, and the indentation cracks run to the ends of the sample. The cracks parallel and perpendicular to the Material 1 polymer line are nearly equal in size, indicating that there is no appreciable stress in this system. The block arrows indicate direction parallel to the polymer lines.

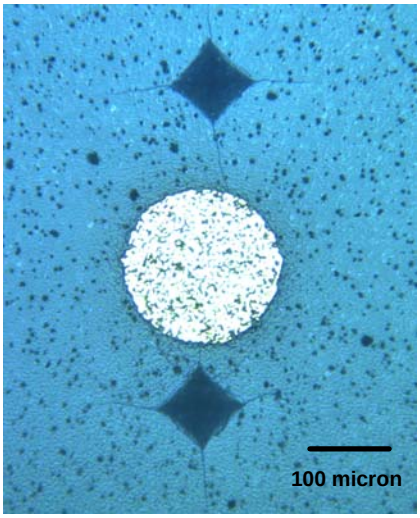

Figure 2. Indentation cracks in a LTCC substrate (blue) interact with the stress field around the metallic via (diameter~ 200 microns). The stress state influences the crack initiation, and three (instead of one) cracks initiate closer to the via (bottom indent, top vertex). Crack trajectories at the two vertices below are slightly affected, whereas the bottom vertex is unaffected. Only the crack emanating from the bottom vertex of the indent further from the metal via (top) is affected by the stress field.

NMR Spectroscopy Investigations of Thin Films and Interfaces

T. M. Alam

Motivation: The development and implementation of new nuclear magnetic resonance (NMR) spectroscopy techniques that allow for the investigation of thin films and interfaces in materials is an area of active research at Sandia. The NMR laboratory continues to use these advances to probe the structure and chemistry in amorphous and highly disordered materials.

Accomplishment: During the last few years the advent of very fast ^{1}H magic angle spinning (MAS) NMR, along with increasing magnetic field strengths, has greatly improved the spectral resolution obtainable for ^{1}H NMR of materials. The increased sensitivity of the ^{1}H MAS NMR also allows much smaller sample sizes to be investigated, including thin films. The development of multi-dimensional and multi-quantum NMR spectroscopy has allowed additional details about the structure, dynamics and morphology of materials to be addressed. Solid-state double quantum (DQ) two-dimensional (2D) ^{1}H MAS NMR spectroscopy has been used to investigate hydrogen bonding in supramolecular complexes, domain size in biofuel cell membranes, water dynamics in mesoporous materials, and molecular self-assembly. During self-assembly, interactions between the inorganic and organic aggregates are known to be important, but for uncharged surfactant species these organic/inorganic interactions are poorly characterized. NMR spectroscopy provides an excellent tool to characterize these materials. For example, we have recently reported the use of solid-state high-speed ^{1}H MAS NMR along with 2D DQ NMR to investigate the local structure of surfactant-templated silicate thin films involved in the evaporation-induced self-assembly (EISA) through detection of close spatial interaction between different molecular species in these materials.[1] Figure 1 shows the 2D ^{1}H correlation spectrum and a graphical representation of the inorganic-organic interactions measured.

The use of ^{13}C-enriched materials has also allowed us to investigate the low temperature annealing properties of tetrahedral amorphous carbon (ta-C) thin films using ^{13}C NMR spectroscopy. Thin films of ta-C have been investigated for MEMS applications, but the nature of stress relaxation is still open to question. Through a series of solid-state ^{13}C MAS NMR investigations, we have recently provided important atomic level details about the annealing process for 0.35 μm thin films of the ta-C material (Figure 2)[2]. Interestingly we have shown that no major conversion between 4-fold and 3-fold coordinated carbon occurs during the annealing process. In addition, we have shown that the stress relief is heterogeneous with respect to carbon type, with the 3-fold carbon type revealing the largest reduction in structural distribution with annealing time. The implication of these NMR measurements for stress-relief mechanisms are discussed, and a model for stress relaxation with annealing is presented in detail elsewhere.[2]

Significance: These studies and examples clearly demonstrate the potential of NMR spectroscopy for the analysis of thin films and interfaces in amorphous and disordered materials.

[1] T.M. Alam, H. Fan, (2003) *Macromol. Chem. Phys.*, **204**, 2023-2030.
[2] T.M. Alam, T.A. Friedmann, P.A. Schultz, D. Sebastiani (2003) *Phys. Rev. B,* **67**, 245309-20.

Contact: Todd Alam, Organic Materials Dept., Org. 1811
Phone: (505) 844-1225
Fax: (505) 844-9624
Email: tmalam@sandia.gov

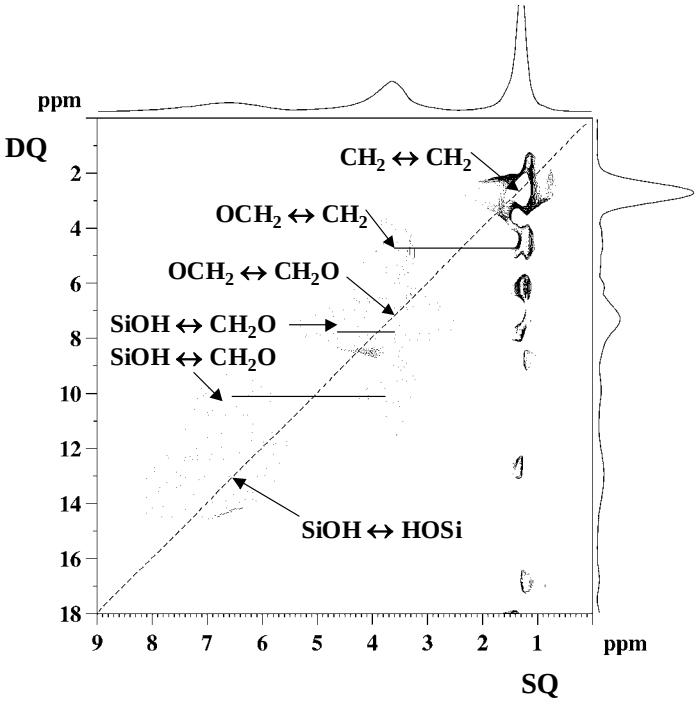

Figure 1. The 2D DQ ^{1}H MAS NMR spectrum of a surfactant-templated mesoporous silicate thin film, from which the spatial distances between chemically different protons within the thin film can be determined. Lower portion of the figure shows a graphical representation of the spatial contacts between the silanols, oxomethylene protons of the surfactant and water within the template silicate thin film.

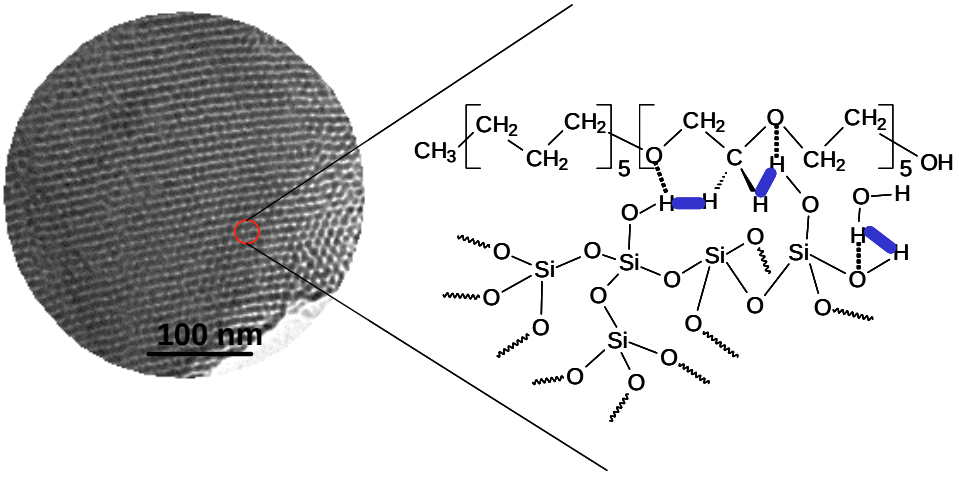

Figure 2. The experimental 1D ^{13}C MAS NMR spectrum of tetrahedral amorphous carbon thin film during low temperature annealing along with the simulated ^{13}C NMR spectrum based on *ab initio* and molecular dynamic simulations.

Pole Figure Integration for Intensity Correction of Textured Samples

M. A. Rodriguez, R. G. Tissot

Motivation: We have developed a technique to integrate the volume of a pole figure and reassign its intensity to a given HKL. This ability is important because accurate intensity values are critical for structural analysis of materials. Parameters such as atom site occupancy, phase fraction, and atomic displacement all effect peak intensity.

Difficulty often arises in determining accurate intensities because of texture in the material. Samples for neutron targets are often textured. This results in strong variability of peak intensities in standard Θ-2Θ scans and limits structural analysis of samples.

Because the intensity of a given HKL is strongly dependent on the sample orientation, we can collect intensity of a given HKL in many different orientations (pole figure) to unbias observed intensities due to texturing. Subsequent integration of the pole figure using our newly developed IDL-based software program results in much more accurate intensity values.

Accomplishment: Figures 1 and 2 show the pole figures for a molybdenum substrate. If one considers the initial observed intensities from the Θ-2Θ scan as listed in Table 1, one can clearly see that the observed relative intensities of the (110) and (200) are incorrect as compared to the expected data from the standard in our database (which represents a randomly-oriented sample).

After pole figure integration, assigned corrected intensities are very close to expected intensity values in Table 1

Significance: This new technique will improve our ability to understand texture effects and eventually enable structural analysis of textured samples by unbiasing texture-related intensity effects from structure-related intensity variation. This technique is currently under investigation for usefulness in determining structural aspects of textured Er-Tritide films.

Table 1. Relative Intensisties for Moly Sample

HKL	Observed Rel. Int.	Expected Rel. Int.	Corrected Rel. Int.
(110)	34	100	100
(200)	100	16	14
(211)	22	31	38

Contact: Mark Rodriguez, Materials Characterization Dept., 1822
Phone: (505) 844-3583
Fax: (505) 844-9781
Email: marodri@sandia.gov

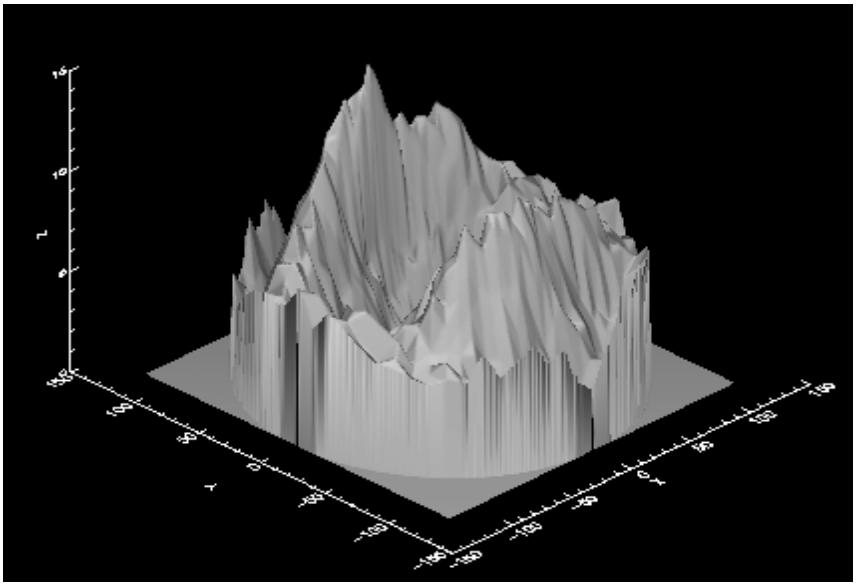

Figure 1. Molybdenum (110) pole figure.

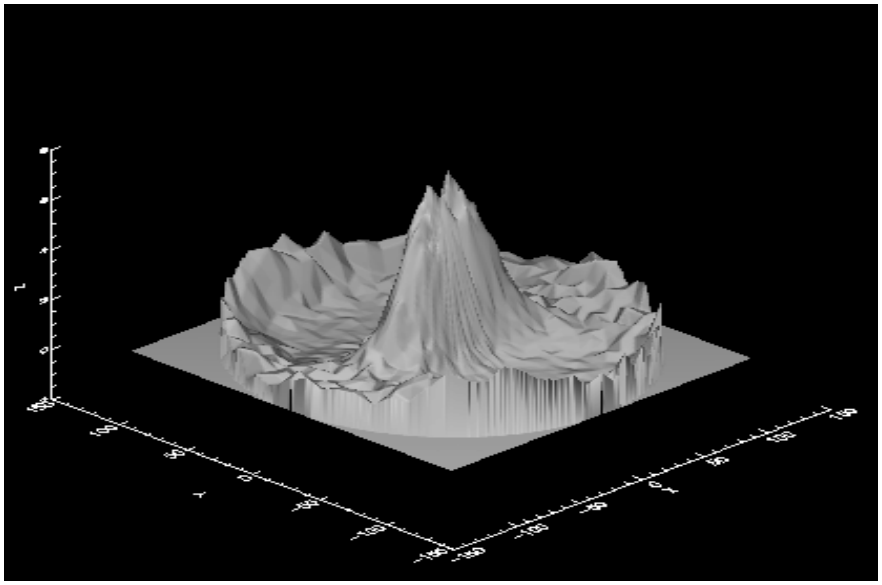

Figure 2. Molybdenum (200) pole figure.

Measuring Low Levels of Polymer Oxidation by Neutron Emission

R. Assink, M. Celina

Motivation: Organic materials are often the life-limiting component of complex defense and commercial assemblies. Accurately predicting the performance of these materials as a function of time has significant economic and national security implications. Thermo-oxidation, a common degradation mode for many organic materials, is controlled by a series of reactions involving chain scission, chain crosslinking and changes in the functional chemistry along the polymer backbone. It is exceedingly difficult to model these processes from first principles. Predictions of polymer lifetimes depend on more phenomenological approaches such as the extrapolation of high-temperature short-time behavior to low-temperature long-time predictions. These extrapolations may span several orders of magnitude in time and can result in considerable uncertainty. Multiple reaction pathways cause non-Arrhenius behavior that leads to predicted lifetimes that exceed actual lifetimes. Previous studies have shown that the degradation of the macroscopic properties of a polymer is closely correlated to the amount of oxygen consumed by the polymer. The task of predicting a polymer's lifetime can, therefore, be reduced to measuring the rate of oxygen consumption at the polymer's use temperature. We have developed a method based on neutron emission techniques to measure the oxidation rate of polymers at ambient conditions.

Accomplishment: Measuring the very slow oxidation rates of ambient temperature polymers requires a sensitive probe of the oxygen content and the means to distinguish the oxygen incorporated during the exposure period from oxidation that occurred earlier in the life of the polymer. The use of ^{18}O as the oxidant enables us to precisely control the time and conditions under which the polymer degrades. The ^{18}O label also provides a sensitive method to measure oxygen content by neutron emission techniques. A series of propellant binders were aged as a function of time in an atmosphere of $^{18}O_2$. Elevated temperatures were used for these experiments in order to incorporate elevated concentrations of ^{18}O in a short period of time. Classical measurements of oxygen pressure and gas analysis were used to calculate the ^{18}O content of each of the samples. These samples were analyzed at the Idaho State Accelerator Center by the $^{18}O(\gamma,p)^{17}N$ reaction shown in Figure 1. We had previously performed measurements to show that the number of neutron counts, as measured by a boron detector, was linearly related to the concentration of ^{18}O in the sample. Figure 2 shows the relationship between neutron counts and the ^{18}O content of the binder samples. We see an excellent correlation between neutron counts and ^{18}O concentration over a range spanning two orders of magnitude. Future efforts are being directed at developing improved detectors and increasing the energy and flux levels of the accelerator. Our goal is to detect ^{18}O at a level of 1ppm. If we are successful, we will be able to measure the oxidation rates of polymers aged at room temperature after exposure of less than 1 week.

Significance: Nuclear emission methods may change how we measure oxidation rates in two fundamental ways: (1) the increased sensitivity may enable polymer lifetimes at ambient conditions to be estimated from experiments completed in days or weeks rather than months and (2) utilization of ^{18}O as a "tracer" may enable us to image the oxidation process of materials in complex engineering assemblies.

Contact: Roger Assink, Organic Materials Dept., 1811
Phone: (505) 844-6372
Fax: (505) 844-9781
Email: raassin@sandia.gov

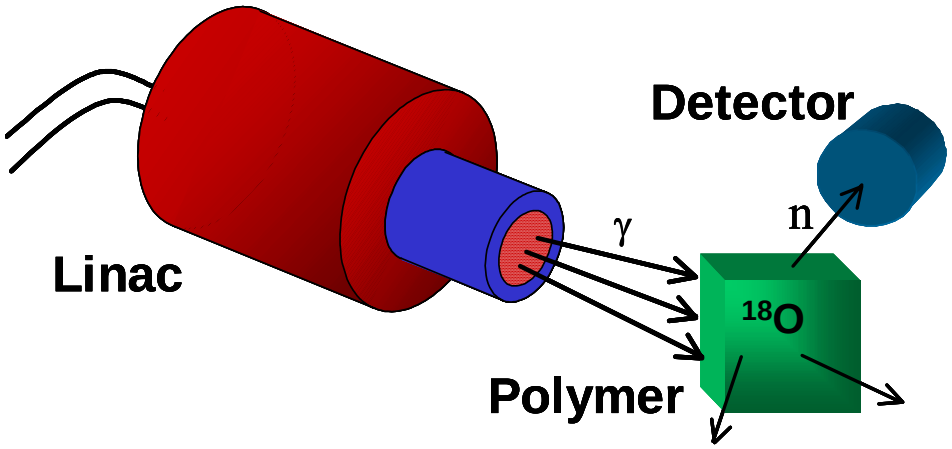

Figure 1. Collaboration with the Idaho State Accelerator Center to optimize the detection of ^{18}O in polymers by neutron emission techniques.

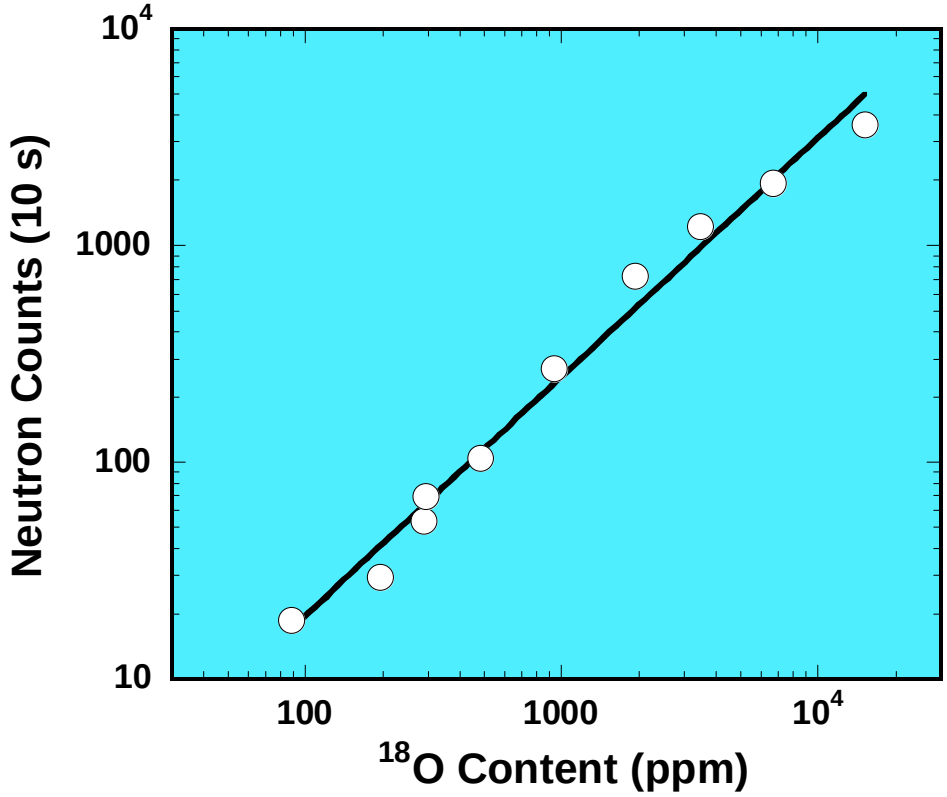

Figure 2. Excellent correlation between the ^{18}O concentration and neutron counts for a series of propellant binders.

Molecular Modeling of Polyolefins using Theory and Simulation

J. G. Curro, G. S. Grest

Motivation: Polyolefin polymers represent the largest and most important class of polymers in terms of volume of production. Even though these polymers consist of only single bonded carbon and hydrogen atoms, they have a wide range of properties that depend sensitively on the molecular architecture. For example, Krishnamoorti and coworkers showed that ordinary head-to-tail polypropylene is immiscible whereas head-to-head polypropylene is miscible with polyisobutylene. Recent advances in polymer synthesis using metallocene catalysts now give the polymer chemist unprecedented control over the molecular weight, chain architecture, and stereochemistry of polyolefin macromolecules. We have developed computational tools that can help guide the synthesis of new polyolefins with optimized properties.

Accomplishment: Several years ago J. G. Curro and K. S. Schweizer developed a theoretical approach for describing the equilibrium structure and properties of amorphous polymers. This theory, the Polymer Reference Interaction site Model or PRISM theory, is based on an extension to polymers of liquid state methods originally developed for atomic and small molecule fluids. The essence of the theory is that the complex, multiple chain problem is replaced by the much simpler single chain problem. In this work we have written a general PRISM code that solves the PRISM nonlinear integral equations self-consistently with the single chain Monte Carlo simulation. This code gives a computationally tractable description of polymer liquids and polymer alloys using realistic models that reflect true chain architecture. In order to benchmark the accuracy of the ability of the theory to describe the packing of the macromolecules, we performed PRISM calculations and exact Molecular Dynamics (MD) calculations for a range of polyolefin liquids using the same force fields and molecular architecture in both the theory and MD simulations. In Figure 1 we show a comparison between PRISM computations and MD simulation for the intermolecular packing of polyisobutylene, a polyolefin used extensively in o-rings and seals in Sandia applications. The packing is described by the six intermolecular pair correlation functions between CH3, CH2 and C groups making up the PIB macromolecules. It can be seen that the agreement of the theory, while not completely quantative, certainly captures the essence of the intermolecular packing.

Significance: We have performed MD simulations of a number of different polyolefin blends and have found good agreement with experiment for the phase diagrams. As an illustration, in Figure 2 we compare the results for the Flory-Huggins chi parameter obtained from MD simulations with the experimental neutron scattering measurements of Krishnamoorti for head-to-head polypropylene mixed with polyisobutylene. These simulations suggest that MD can be used in general as a computational tool to predict phase behavior of polyolefin mixtures.

Contact: John G. Curro, Materials & Process Modeling & Computation Dept., 1834
Phone: 505-272-7129
Fax: 505-272-7336
E-mail: jgcurro@sandia.gov

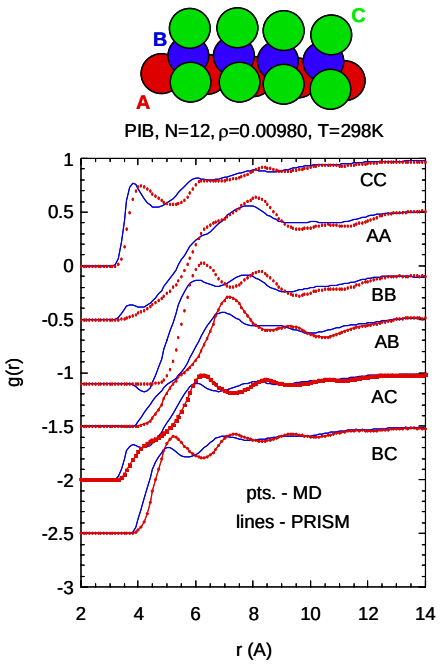

Figure 1. Comparison of PRISM theory and MD simulation for polyisobutylene at 298K.

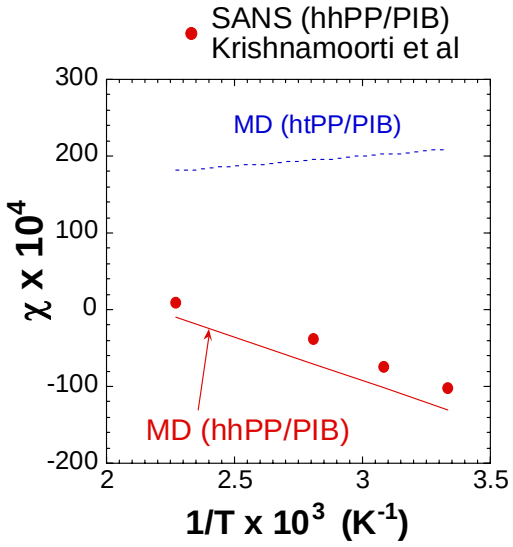

i

Figure 2. The Flory-Huggins chi parameter computed from MD simulations for head-to-head and head-to-tail polypropylene mixed with polyisobutylene (lines). The points were experimentally measured from small angle neutron scattering experiments (Krishnamoorti et al *Macromolecules* **28** 1250 (1995)).

Research in Infrared Spectroscopy

M. K. Alam, D. Rivera

Motivation: Routine infrared spectroscopy has typically required clear liquid samples placed in a thin transmission cell. Component separation was often done to avoid overlapping bands, allowing the researcher to uniquely identify the components or develop a clean, univariate calibration curve. Nowadays, investigators do not have the time to develop sophisticated sample preparation methods, but still need the detailed chemical information provided by infrared analysis. Thus, the non-traditional infrared sampling methods, combined with sophisticated multivariate analysis have begun to find a niche. These methods have been developed in our laboratory to examine a variety of chemical and materials problems. We have a number of non-traditional sampling methods providing fast spatial information about the sample under study. Thermogravimetric analysis combined with infrared has been used to provide not only qualitative information regarding the thermal decomposition products, but developed multivariate methods have also provided quantitative information regarding the evolved gases. Recently developed photoacoustic (PAS) methods have shown promise when combined with multivariate analysis in providing interesting qualitative information regarding the change in composition with depth. Finally, attenuated total reflectance sampling has been used to study water-based samples, long a difficult task for infrared spectroscopy.

Accomplishment: Photoacoustic spectroscopy has been used to study polymer aging as a function of depth. Photoacoustic FT-IR (PAS/FTIR) spectroscopy works by modulating infrared radiation at acoustic frequencies and detecting the "sound" of the radiation that is returned from the sample of interest, using a microphone as the detector. This study demonstrated the usefulness of PAS FT-IR combined with multivariate analysis. Using this method the molecular components of aging within hydroxyl terminated polybutadiene/dimethyl disocyanate copolymer were identified. Small chunks of the polymer were sampled without any further preparation. Standard multivariate methods such as PLS gave good predictions of age as a function of depth. Additionally, Multivariate Curve Resolution provided a relative measure of kinetics and the pure component plots obtained from the PAS data (Figure 1), showing the oxidized and unoxidized components.

Attenuated Total Reflectance (ATR) Spectroscopy allows water-based samples to be analyzed using infrared by limiting the analyzed pathlength to a micron or less. ATR uses an internal reflectance element (IRE) to guide the infrared light. As the light 'bounces' through the crystal it interacts with the sample placed on top of the crystal. We have used this technique to study live, murine macrophage cells as they reacted to an activating agent, simulating infection. Cells were analyzed using two methods: 1) direct placement of cells on the ATR crystal and 2) growing the cells directly on the crystal surface. In both cases, molecular signatures were identified that allowed classification of control populations from those cell that were activated. Figure 2 shows the separation of the two populations using principal components analysis and the resulting spectral features associated with activation.

Significance: This work has indicated the wide range of materials that can be analyzed by infrared spectroscopic techniques. Combined with multivariate analysis, these techniques can provide a wealth of chemical information without rigorous sample preparation.

Contact: Kathy Alam, Chemical & Biological Sensing, Imaging & Analysis Dept., 1812
Phone: (505) 845-9621
Fax: (505) 844-2974
Email: mkalam@sandia.gov

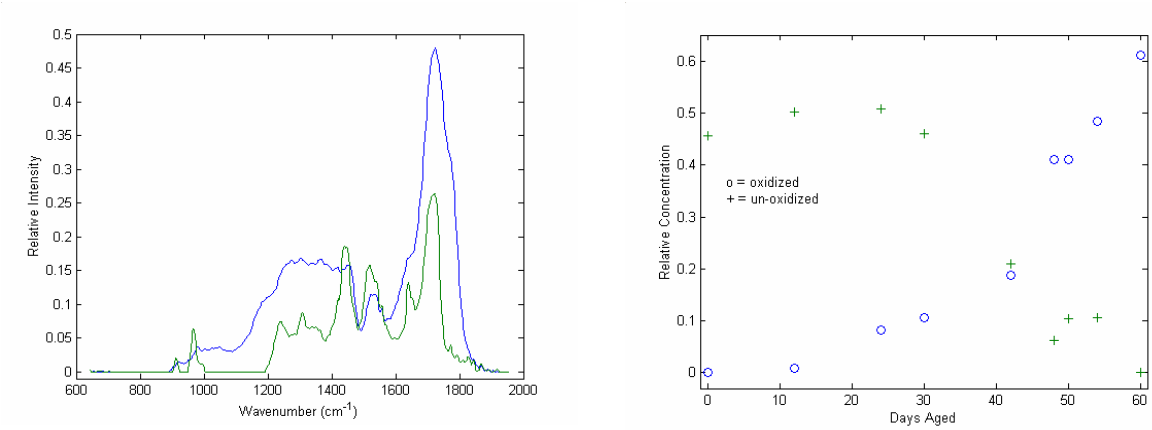

(a) (b)

Figure 1. a) The curve resolution estimates of the spectral components, oxidized (blue) and unoxidized (green) are shown. b) the relative concentration estimated for the oxidized (+) and unoxidized (o) are indicated. The curve resolution results are from photoacoustic data collected at 732 Hz between 2000 and 600 cm^{-1}.

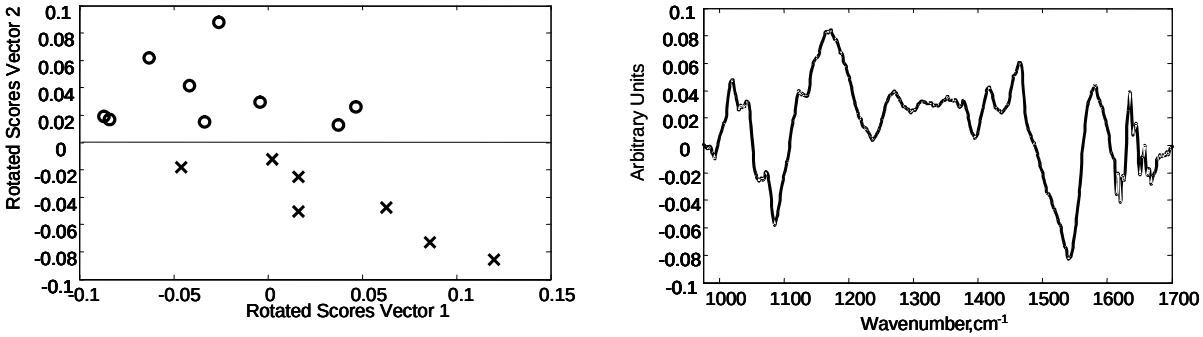

(a) (b)

Figure 2. Shown are rotated principal components calculated from infrared spectral data collected from activated and control cell samples. The rotated scores are shown in (a) while the rotated loading associated with rotated scores vector is shown in (b).

Base Metal Integrated High K' Dielectrics

P.G. Clem, J.T. Dawley, J. Richardson

Motivation: Base metal integration of high K' dielectrics is of interest for microelectronic packaging and low cost passive component production. Historically, thin films of high dielectric constant oxides such as $BaTiO_3$ have been deposited on high cost platinum or gold bottom electrodes. However, the high cost of these metals may comprise over half the cost of resulting capacitors. A new method has been developed for deposition of random grain orientation or epitaxial growth of high dielectric constant oxides on low cost base metals such as Ni, Cu or Al. This process utilizes low cost, ambient pressure chemical solution deposition (a.k.a. sol-gel processing) to dip coat or spin coat films on base metal tapes, and crystallize the films at relatively low temperatures of 500-900°C in a low oxygen partial pressure atmosphere. This enables crystallization and enhanced properties of these oxide films on a variety of low-cost metal substrates, for high density decoupling capacitor or multilayer capacitor applications.

Accomplishment: The new process is the first report of solution-deposited dielectrics with high dielectric constant values atop base metal substrates. Processing and properties are presented in Figures 1 and 2 for random and enhanced <100> orientation $SrTiO_3$ and $Ba_xSr_{1-x}TiO_3$ (x = 0.33, 0.50, and 0.67) films fabricated on base-metal <100> Ni tapes using a chemical solution deposition (CSD) approach.[1,2] Permittivity values over 1000 were obtained for several BST film compositions on Ni substrates. Films were crystallized in a reducing atmosphere, which prevented Ni oxidation, but permitted growth of oxygenated $SrTiO_3$ and $Ba_xSr_{1-x}TiO_3$ films with dielectric loss tan δ = 0.003 - 0.015. For randomly oriented $Ba_xSr_{1-x}TiO_3$ (x = 0, 0.33, 0.5, 0.67) films, zero-field 100kHz dielectric constants ranged from 250 to 420. Films with enhanced <100> orientation exhibited zero-field dielectric constants of 980 to 1550, three times higher than randomly oriented films. Transmission electron microscopy of the enhanced (100) orientation STO and BST films, grown at low pO_2 (< 10^{-13} atm O_2), shows growth of perovskite unit cells with registry to the Ni substrate, with clean interfaces, free of NiO formation. This interface structure and perovskite/Ni mosaic registry is a result of using pO_2 values below the Ni→NiO thermodynamic equilibrium line. It is proposed that the oxygenated precursors (alkoxides and carboxylic acids) used in the CSD process may be responsible for the apparent full oxygenation and low loss tan δ of the deposited films, in contrast to many vapor phase deposited films.

Significance: The technology developed enables low-cost, low temperature (500°C) integration of high dielectric constant insulators on a variety of oxidation-sensitive substrates. Other perovskite dielectric and substrate materials are currently under investigation. Development of such high (ε' = 1000-1500) dielectric constants on Ni enables inexpensive, high performance base-metal electrode capacitor fabrication for printed circuit board integration or reduced-cost multilayer capacitor fabrication.

1 J.T. Dawley and P.G. Clem, *Applied Physics Letters* 81(16), 2038 (2002).

2 R.J. Ong, J.T. Dawley, P.G. Clem, *Journal of Materials Research* 18(10), 2310 (2003).

Contact: Paul Clem, Microsystem Technologies Dept., 01851
Phone: (505) 845-7544
Fax: (505) 844-9781
Email: mailto:pgclem@sandia.gov

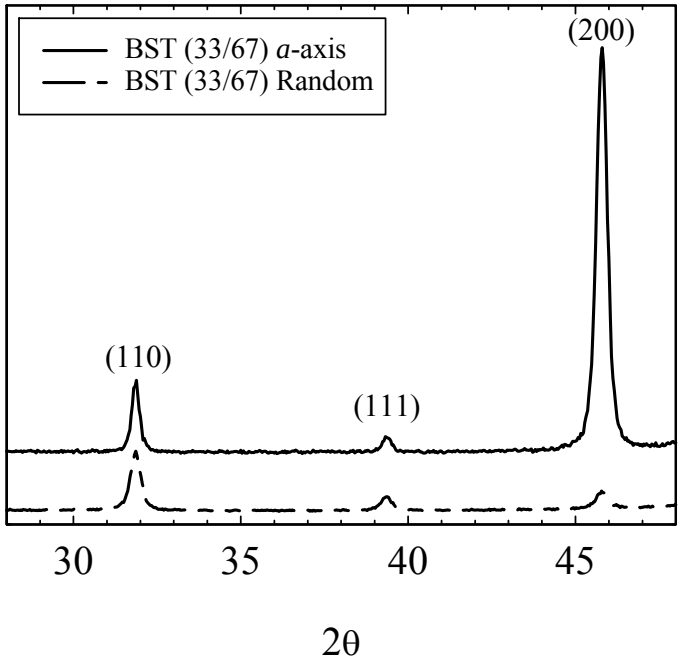

Figure 1. X-ray diffraction of (100) oriented, solution deposited (Ba,Sr)TiO_3 dielectric films on Ni tape.

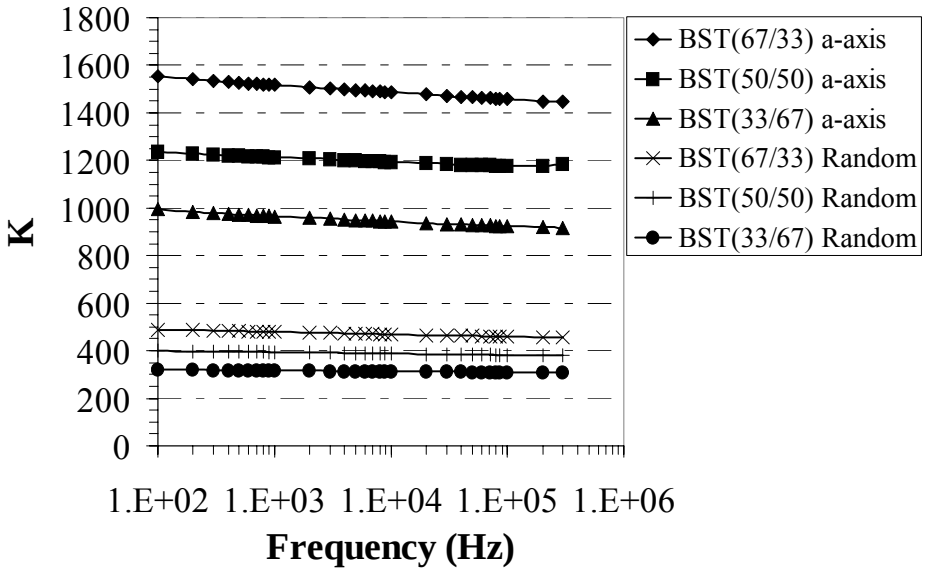

Figure 2. Dielectric constant versus frequency for randomly-oriented vs. (100) textured (Ba,Sr)TiO_3 films, displaying 3X improvement in capacitance density.

Corrosion Behavior and Electrical Contact Resistance of LIGA Electrical Contact Spring

L. Serna

Motivation: LIGA technology is used to produce small-scale metal electrodeposits of net-shape parts with high precision (e.g. micron tolerances). These parts will play an increasingly important role in new component designs in a number of high-reliability applications (e.g. weapon surety). For example, the LIGA electrical contact spring shown in Figure 1 is designed to replace a conventional spring in a specific electrical application. The conventional spring is made of a gold-based alloy, whereas the Ni-based LIGA part must be gold-plated to enhance its electrical contact properties.

Although Ni is a fairly corrosion resistant material, the unique microstructure and the possibility of contaminant trapping during processing and fabrication could influence the corrosion behavior of LIGA materials. A study is ongoing to characterize this behavior of actual LIGA parts under service conditions, and to bound the environmental conditions that could result in unacceptable degradation. The specific initial objective of these aging studies is to determine how gold-plated LIGA springs will perform relative to the conventional material, Neyoro G. Interestingly, although the corrosion rate of Ni is very low under most atmospheric conditions (microns/year), corrosion of nickel is known to be accelerated by bimetallic contact with gold.

Accomplishment: State-of-the-art techniques were used to test LIGA parts in both aqueous and atmospheric environments. Aqueous electrochemical tests provide quantitative data (pitting potentials) and can be used to test specific part surfaces (e.g. lapped, release and sidewall). Due to the small size of LIGA parts, aqueous tests were conducted using a micro-capillary system capable of targeting small length-scale features (e.g. 50 microns). Electrochemical test results indicate that uncoated LIGA NiMn has similar (even slightly higher) corrosion resistance than wrought pure Ni (Figure 2). Atmospheric tests provide a more relevant exposure environment for these parts. Controlled accelerated aging conditions, in a regime that produced low corrosion rates, were used and included increased temperature, humidity and contaminant levels. Exposing gold-plated LIGA parts showed that the base Ni material is susceptible to corrosion through pores in the gold coating (Figure 3). No corrosion was observed on Neyoro G. The environment used for these initial scoping tests, however, is much more aggressive than those normally found in our military hardware.

As a component intended to complete an electrical circuit, the LIGA spring is required to have low contact resistance. Therefore, corrosion product build-up on the gold layer is a concern. Future studies will focus on determining the effect of corrosion product build-up on electrical contact resistance. These measurements will be made using a custom microprobe station (Figure 4).

Significance: These studies have shown that under highly accelerated conditions, significant differences exist in the corrosion resistance of gold-plated LIGA NiMn compared to the noble material it is intended to replace. Of utmost importance, however, is that this does not preclude reliable use in an actual weapon environment. The goal of future work is to provide information on the environmental limits of the LIGA contact spring with respect to corrosion, so that performance will not be compromised.

Contact: Lysle Serna, Corrosion, Electrochemistry and Cleaning, Dept. 1832
Phone: (505) 284-4495
Fax: (505) 844-7910
Email: lmserna@sandia.gov

Figure 1. LIGA electrical contract spring in development for the W76-1 & W80-2, 3.

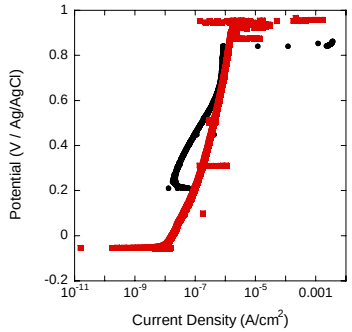

Figure 2. Potentiodynamic scans of LIGA NiMn and pure Ni in 50 mM NaCl, measured using 80 micron diameter capillary. Pitting potential is the metric for corrosion resistance. In this example, LIGA has a slightly higher corrosion resistance than pure Ni.

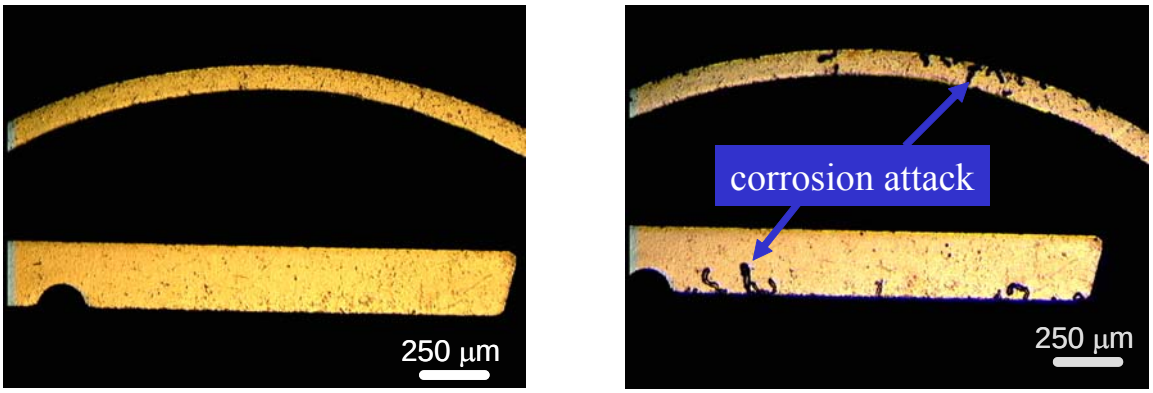

(a) (b)

Figure 3. Gold-plated LIGA NiMn spring arm a. pre-exposure, b. post exposure, 2 weeks in Class II atmospheric environment.

Figure 4. Contact resistance station for measuring change in contact resistance as a function of environmental exposure. Probe is shown in contact with a gold-plated LIGA part.

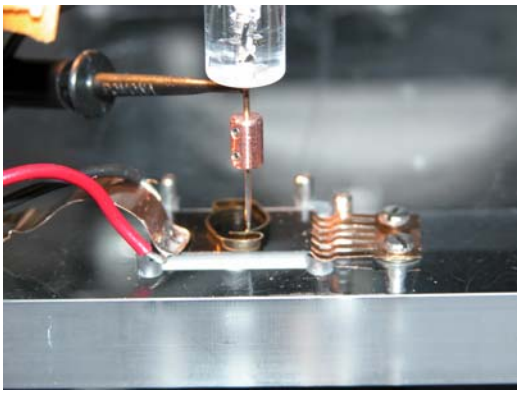

Development of High Zr Content PLZT Thin Films for Integrated Microsystems

B. A. Tuttle, D. Williams, T. Headley, M. Rodriguez, J. Wheeler, G. Brennecka

Motivation: Next generation micro-fuze and DOI capacitor pulse discharge units require high energy density capacitors that are integrable with Si CMOS and MEMS technology. Recent developments in the field of dielectric relaxor materials have the potential to enhance system reliability and performance by miniaturization and integration of the largest component in these micro-systems: the pulse discharge capacitors. High Zr content PLZT (HZPLZT) dielectrics being developed at SNL have the potential to reduce device size by a factor of 2 to 20 times. In order to achieve this revolutionary improvement, materials issues of controlling high PbO activity within HZPLZT films and formation of multilayer devices must be addressed.

Accomplishment: Sandia scientists have determined synthesis procedures for High Zr PLZT thin film dielectrics that will be the basis of Si integrable high energy density capacitors for next generation micro-fuze and DOI capacitor pulse discharge units. Critical understanding of process – microstructure relationships has recently been developed. It is essential for the development of high energy density capacitors to fabricate single phase perovskite films (Figure 1) which have high dielectric constants (K > 1000). Because of the high PbO activity of the HZPLZT material family, single phase perovskite films with high dielectric constants are not achieved through conventional processing. Typically, a Pb deficient fluorite phase with a dielectric constant of approximately 50 forms on the top of the 0.4 μm thick film that can reduce the overall dielectric constant, and thus, the energy handling capability by as much as a factor of 6 (Figure 2). Seven different process parameters were investigated to optimize film properties. Pyrolysis temperature, the temperature at which volatile organics are removed from the chemical solution deposited film, was shown to be an extremely critical parameter. Appropriate modification of process parameters results in single phase perovskite films with a wide range of grain morphologies and ferroelectric domain assemblages. Process optimized thin films resulted in reproducible capacitors with area dimensions large enough for prototype CDUs. These PZT based thin film capacitors have energy densities of 16 J/cm3, approximately 20 times the energy density of state of the art BaTiO3 bulk dielectrics. Further, Sandia's first multi-layer PZT thin film capacitor has been fabricated and tested. While the Multilayer capacitor has expected dielectric properties at 1 kHz, further process development is underway to enhance performance at higher frequencies.

Significance: This new technology will enable both ruggedized and future generation fireset technology.

A critical materials development in obtaining high dielectric constant, high energy density films was the ability of SNL scientists to control Pb stoichiometry over nanometer dimensions at dielectric electrode interfaces for these high PbO activity materials. Our materials development will impact RF MEMS, pyroelectric sensor and decoupling capacitor technologies. In addition to the considerable interest in this technology by DOE DP systems engineers, the Office of Naval Research, the Army Research Office, DOE OAAT and General Motors have applications that will benefit from our next generation high energy density dielectric film achievements.

Contact: Bruce Tuttle, Ceramic Materials Dept., 1843
Phone: (505) 845-8026
Fax: (505) 844-9781
Email: slmonro@sandia.gov

K = 1200

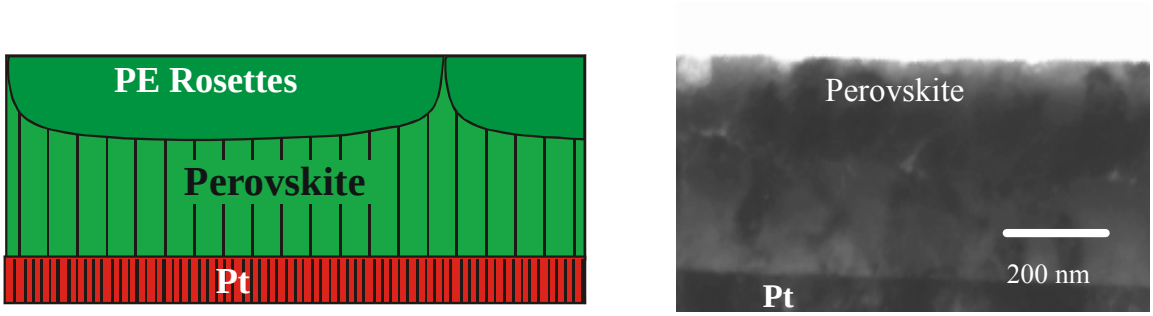

Figure 1. TEM micrograph and Schematic Diagram of High Dielectric Constant HZPLZT Film

K = 650

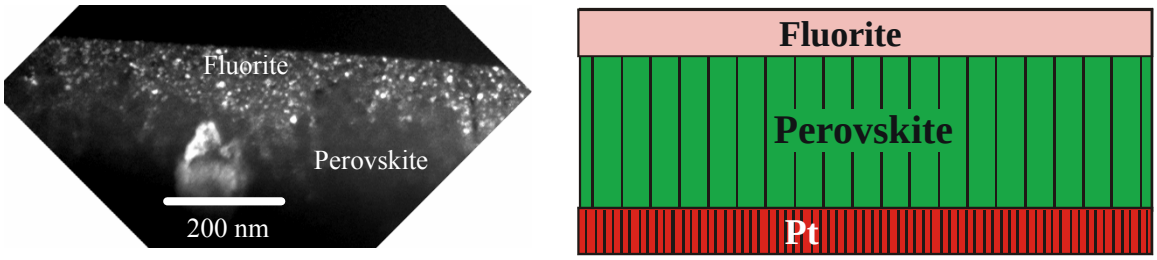

Figure 2. TEM micrograph and Schematic Diagram of Low Dielectric Constant HZPLZT Film

Friction between Disordered Self-Assembled Alkylsilane Monolayers

M. Chandross, G. S. Grest, M. J. Stevens, E. B. Webb III

Motivation: Self-assembled monolayers (SAMs) offer a unique means to alter and control the chemical nature of surfaces. The alkylsilanes are a particularly interesting type of SAM because they bond to oxide surfaces and are thus of use in silicon based micro-electromechanical systems (MEMS), which have a native oxide surface. While experimental measurements yield atomic scale force data, they do not produce the simultaneous structural characterization that can be deduced from molecular scale simulations. A predictive, molecular-level understanding of friction is the missing key to intelligently designing interfacial lubricants for MEMS

Accomplishment: Molecular dynamics (MD) simulations are ideal for probing the properties of SAM coated surfaces, since they are able to produce both atomic scale force data as well as the underlying structural information. We have carried out extensive MD simulations of the adhesion and lubrication of SAM coated SiO_2 surfaces. We have studied the effects of chain length, system size, shear velocity, and defect density between pairs of SAMs covalently bonded to crystalline and amorphous SiO_2 surfaces. Representative snapshots of equilibrated SAMs with defect densities ranging from zero to 30% are shown in Figure 1. As the surfaces are brought into contact, there is a small region of attraction due to the van der Waals interaction, of about 150MPa for all chain lengths studied, n = 6 to 18. Further decrease in the distance between the surfaces leads to compression, as the interactions become strongly repulsive. The relationship between load and surface separation is monotonically dependent on the chain length. Shorter chains are stiffer and have a larger repulsion compared to longer chains. Increasing defect density at a given chain length also results in stiffer chains, as the increase in area per headgroup allows chains to collapse (see Figure 1).

Lubrication between SAMs is studied by shearing two surfaces relative to each other. The velocities that can be studied by MD are within the range of MEMS devices but large compared to typical force probes. We find that for well-ordered, fully packed SAMs the friction exhibits a non-monotonic chain-length dependence, as seen experimentally. For this case all chain lengths and shear velocities studied show stick-slip dynamics, as seen in Figure 2a. Stick-slip dynamics requires commensurability of the two sliding surfaces, which can be broken by a small percentage of defects, as shown in Figure 2b. Increasing defects leads to increasing friction coefficients μ in the compressive regime, as determined from the slope of the shear stress vs. normal force. Most friction simulations in the literature determine μ by dividing shear stress by load at a single state point, which does not account for the attractive region in the force-separation curve, and gives erroneous results.

Significance: MD simulations provide new insight into the atomic scale motion of SAMs, providing details of the molecular structure under shear and the energy dissipation mechanisms. Other work on this project has included varying the end groups to study the chemical dependence of friction and including fluorocarbons. Future work will introduce water into the simulations, leading to a quantitative understanding of adhesion and friction under adverse environmental conditions.

Contact: Michael Chandross, Materials & Process Modeling & Computation Dept., 1834
Phone: (505) 844-5081
Fax: (505) 844-9781
Email: mechand@sandia.gov

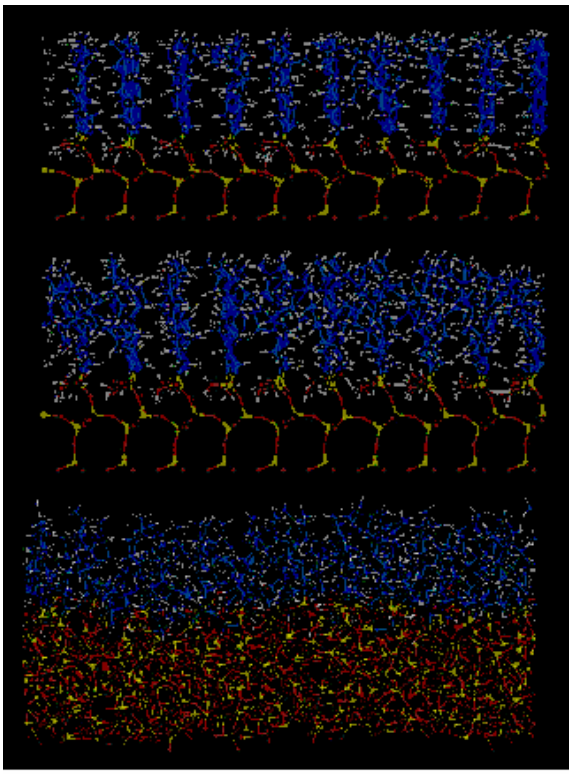

Figure 1. Snapshot of an *n*=8 alkylsilane SAMs with (a) zero [top], (b) 10% [middle], and (c) 30% defects [lower]. Both (a) and (b) show SAMs on a crystalline substrate while (c) shows a SAM on an amorphous substrate. Silicon atoms are red, oxygen atoms are yellow, carbon atoms are cyan and hydrogen atoms are white.

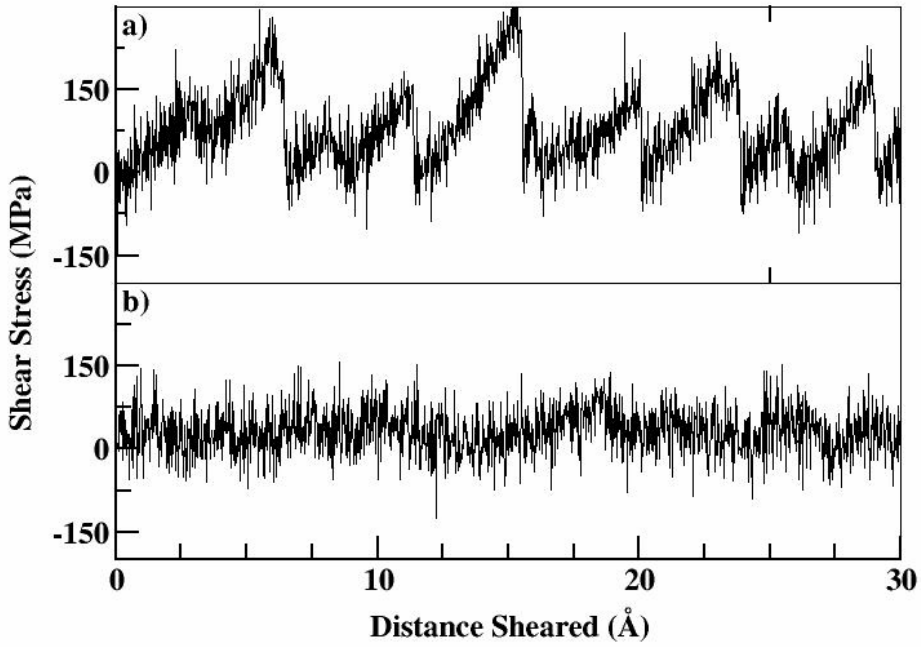

Figure 2. Shear stress as a function of distance sheared for *n*= 9 at a normal load of 200 MPa and relative shear velocity *v*=0.2 m/s with (a) no defects [top],and (b) 10% defects[lower]. Results for 100 chains attached to each crystalline surface.

Novel Techniques for Characterizing Wear Surfaces in Microsystems Materials by Cross-sectional Microscopy using FIB and EBSD

J. R. Michael, S. V. Prasad

Motivation: Plastic strains during sliding contact typically result in subsurface layers whose microstructures are different from those of the bulk. Changes in the surface roughness, hardness, grain size and texture often occur during the initial run-in period, resulting in the evolution of a subsurface layer with characteristic features. Friction is, therefore, a time-dependent phenomenon until a steady state subsurface is evolved. Microstructural characterization of wear -induced sub-surfaces is critical to the understanding of tribological phenomena. Conventional cross-sectional TEM specimen preparation techniques require large wear scars, and involve such aggressive steps as core drilling, grinding, dimpling and electropolishing, which are time consuming and cumbersome. Also they are inadequate in locating sub-surface regions at specific locations on the wear surface. Thus, the conventional microstructural characterization techniques are clearly not suited for Microsystems materials. We have utilized focused ion beam (FIB) micromachining to produce site specific cross section samples from small wear scars suitable for transmission electron microscopy (TEM) and orientation mapping via electron backscatter diffraction (EBSD).

Accomplishment: Figure 1 shows an example of a unidirectional wear scar on a LIGA Ni surface. We have utilized a FEI DB (dual beam)-235 FIB tool to prepare a cross section of the wear scar in the location shown in Figure 1. In this particular case the final FIB cut cross section is parallel to the sliding direction, although any orientation is possible. Orientation analysis was conducted in the DB-235 tool using the HKL Technology orientation mapping hardware and software. The as-electrodeposited Ni has a <100> fiber texture with respect to the growth direction. The orientation map from a wear scar section clearly reveals microstructural changes with an equi-axed fine grained recrystallized zone near the surface followed by a region of deformed columnar grains as shown in Figure 2. There is a region at the extreme surface of the sample that is not successfully studied using EBSD. The reason for this is clear from the TEM image that shows a region with nanocrystalline structure, Figure 3. Selected area electron diffraction obtained from this region reveals a ring pattern indicating the nanocrystalline nature of this layer.

Significance: This work has demonstrated the unique ability to obtain correlative information from SEM, EBSD and TEM over a range of length scales from a single FIB prepared cross section. This technique has also been extended to other microsystem materials such as polycrystalline Si. Many microelectro-mechaninical systems (MEMS), such as the LIGA gear train assembly shown in Figure 4, contain surfaces that come into sliding contact. The techniques developed here will help further our understanding of microstructural evolution due to sliding interactions in MEMS devices.

Contact: Joe Michael, Materials Characterization Dept., 1822
Phone: (505) 844-9115
Fax: (505) 844-2974
Email: jrmicha@sandia.gov

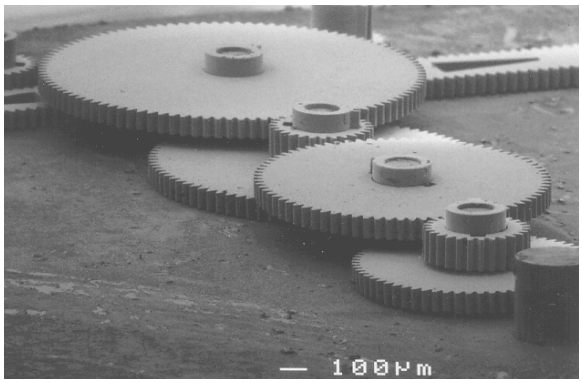

Figure 1. Wear scar in LIGA surface and area from which site-specific FIB micromachined sample was obtained.

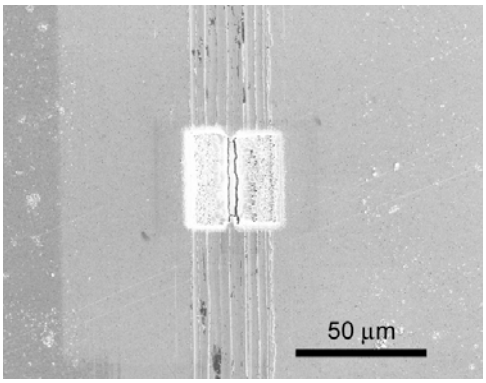

Figure 2. Orientation map of cross section of a wear scar in LIGA Ni. The deformation of the grains and the recrystallized surface layer is clearly visible. The nano-crystalline region at the immediate surface of the sample is not resolved by EBSD.

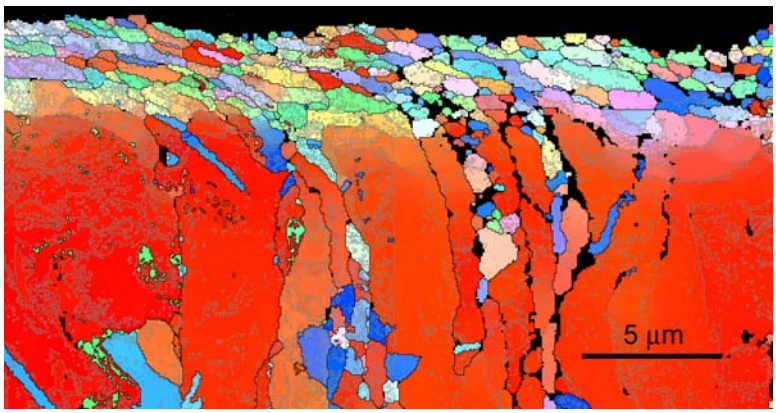

Figure 3. TEM bright field image of the same sample shown in Fig 2. The TEM image is complimentary to the orientation map in that here the nanocrystalline layer is clearly visible.

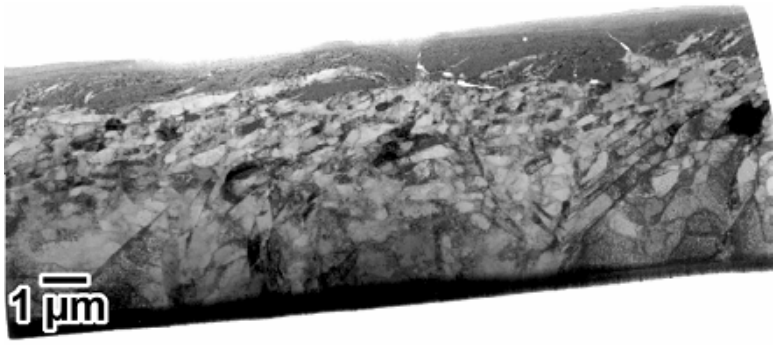

Figure 4. LIGA gear assembly that shows the importance of friction and wear due to the large number of sliding sidewall surfaces.

Pressure, Gas Composition, and Hermeticity of MEMS Packages

S. M. Thornberg, I. C. Abraham, R. M. Rohde

Motivation: Silicon based micro-electro-mechanical systems (MEMS) are gaining importance in a variety of applications. They are already widely employed in the current generation of computer-interfaced slide projectors, and as accelerometers for automotive air bags. Several of the next applications for MEMS devices, such as capacitive pressure sensors, need hermetic vacuum sealing of cavity structures. The frequency response of other devices, such as mechanical oscillating parts, is also influenced by the residual gas pressure. Therefore, sampling of the pressure and gas composition of the interior of sealed cavities becomes vital, particularly as devices age and after long-term operation.

Chemical and physical materials aging processes can significantly degrade the long-term performance and reliability of dormant MEMS devices. This degradation results from materials interactions with the evolving microenvironment by changing both bulk and interfacial properties (e.g., mechanical and fatigue strength, interfacial friction and stiction, and electrical resistance). Eventually, device function is clearly threatened and, as such, these aging processes are considered as high-negative consequence processes.

Accomplishment: The internal atmospheres of MEMS packages as small as 3 µl in internal volume were analyzed, and a non-destructive test for hermeticity of fully packaged MEMS chips was devised. The small volume samples were anodically bonded Pyrex 7740 empty packages (Fig. 1) with internal volumes ranging from 3 µl (rectangular) to 15 µl (square). The full packages were commercial Kyocera 24-pin narrow well packages (Fig. 2) containing a surface micromachined "Aging Module" (internal void volume ~150 µl) that incorporates prototype weapon devices and diagnostic structures made for a MEMS aging and reliability project (Mike Dugger, 1851). Both packages were sealed under an inert nitrogen atmosphere. The MEMS chip package was sealed at elevated temperatures (~300°C), resulting in sub ambient internal pressures at room temperature.

The gas composition measurements were obtained by magnetic sector mass spectrometry. The MEMS package samples were placed in an evacuated known volume and destructively opened, yielding the internal pressure. A substantial amount (~10%) of hydrogen, from the anodic bonding process, was detected in some of the Pyrex samples. All but one of the hermetic MEMS chip samples contained mostly nitrogen. The exception showed air contamination *prior* to sealing.

For the MEMS chip samples, the *non-destructive* leak test procedure measured the small contribution of the gas contained in the MEMS package to the overall pressure inside an enclosure that was exposed to a small (~300 Torr) pressure drop from atmospheric pressure. As shown in Fig. 3, a substantial number (~50%) of the chip samples were non-hermetic.

Significance: Diagnostic gas composition and internal pressure measurements were made on real MEMS package samples, as small as 3 µl in internal volume. A non-destructive hermeticity test of commercial fully assembled MEMS devices showed a substantial number of faulty packages. This procedure could be implemented as a routine test *prior* to electrical/functional testing.

Contact: Steve Thornberg, Chemical & Biological Sensing, Imaging & Analysis Dept., 1812
Phone: (505) 844-8710
Fax: (505) 844-2974
Email: smthorn@sandia.gov

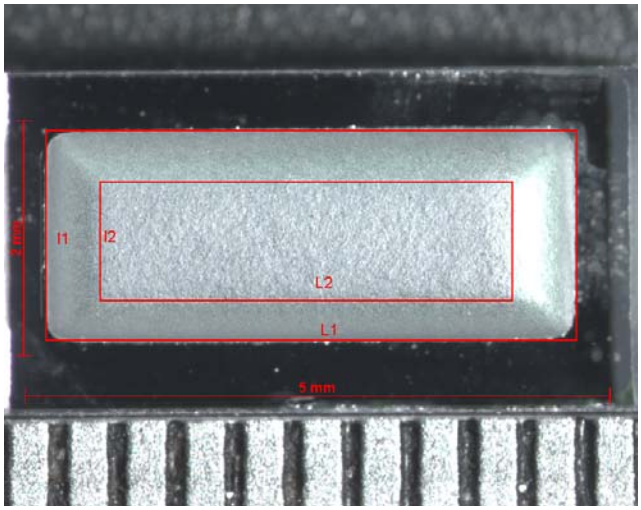

Figure 1.Top view of typical rectangular Pyrex package. The out-of-plane internal thickness (height) of the package is ~0.5 mm. Typical internal volumes were 3-4 µl

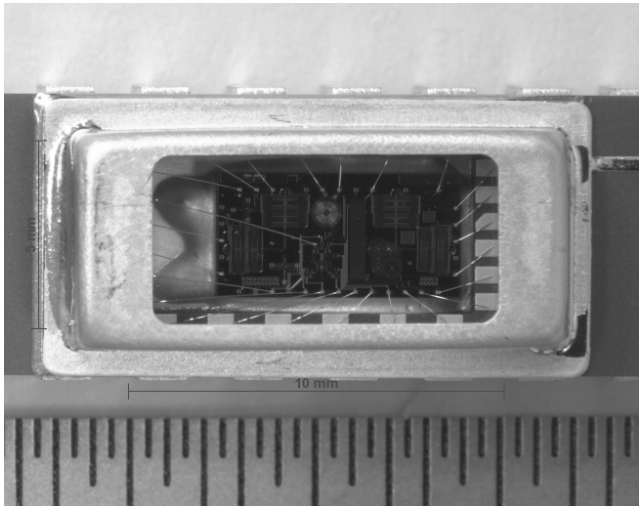

Figure 2. Top view of a typical MEMS chip package.

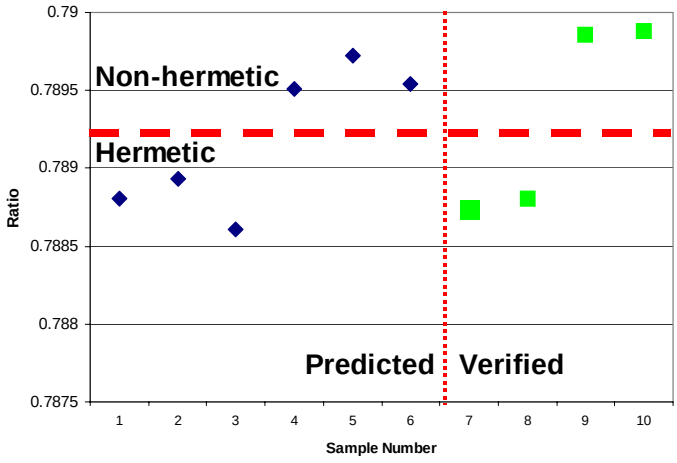

Figure 3. Results of MEMS leak check method showing a clear break between hermetic and non-hermetic parts. The classification of the 4 parts on the right was verified via destructive sampling.

Size Effects on Failure in Polysilicon

C.C. Battaile, T.E. Buchheit, G.W. Wellman, B.L. Boyce

Motivation: Conventional approaches to modeling the mechanical response of elastic materials often assume that the material can be adequately represented as a continuum. However, the small sizes of many MEMS parts jeopardize this assumption. Furthermore, examining the details of phenomena like failure initiation requires information about the microstructure and microscale anisotropy of the material.

Accomplishment: To examine the effects of microstructure on the mechanical response of small-scale elastic components, we perform finite element calculations of elastic deformation in a polycrystalline aggregate of silicon grains. Each grain has a different crystallographic orientation, and because silicon is elastically anisotropic, the distribution of stresses in the material is nonuniform and depends strongly on the distribution of grain orientations. The computer microstructures are represented by 2+1 dimensional hexahedral finite element meshes that are taken directly from orientation imaging micrographs of the poly1/2 and poly3 layers of a silicon gear hub, as shown in Fig 1. These meshes are subjected to simulated uniaxial tension via prescribed displacement boundary conditions in the x-direction (short edges), free surfaces along the x-z faces (long edges), and periodic boundary conditions in the z-direction (into the "page"). The simulations are performed one hundred times with different random distributions of grain orientations on each microstructure, in order to examine the variability of the mechanical response for different incarnations of nominally similar crystallographic textures. Figure 2a-b shows the locations of the maximum von Mises stress for each of these simulations. These locations represent likely failure points. The magnitudes of the maximum local stresses were used to produce the Weibull failure statistics in Fig 2c-d. These Weibull plots resemble the available experimental information (not shown) in form, but exhibit a significantly narrower distribution in the "failure" stress, probably due largely to the absence of structural defects in the simulations.

Significance: The mechanical response of large populations of microstructural features (grains in the present context) is generally assumed to behave as a continuum. The increasing miniaturization of MEMS and related technologies challenge these assumptions and demand that they be verified or refuted, using more detailed calculations and experimental validation. The results presented herein demonstrate that the simulated behavior of microstructures that are identical except for the differing random distributions in grain orientations can show significant spatial variations in mechanical response and failure statistics. These differences can only be exacerbated by other real-world factors, such as microstructural variability and defects, which were omitted from the present simulations. This information suggests that, while continuum approaches are applicable to certain aspects of microsystems analysis, they must be used with caution when addressing structurally dependent behaviors like failure.

Contact: Corbett Battaile, Materials & Process Modeling and Computation Dept., 1834
Phone: (505) 844-7039
Fax: (505) 844-9781
Email: ccbatta@sandia.gov

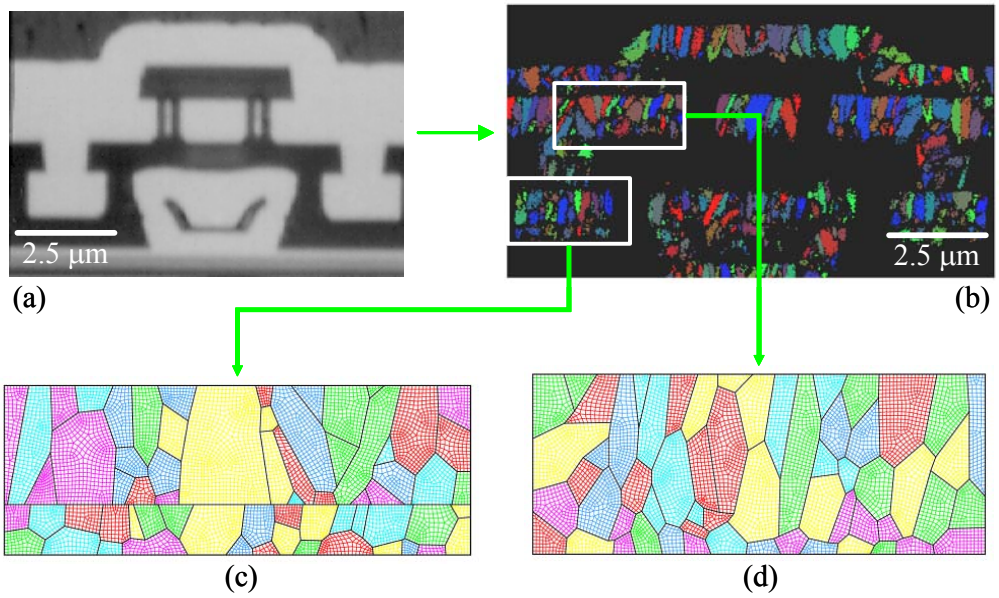

Figure 1. The mapping of a) an optical micrograph of a SUMMiT-fabricated polysilicon gear hub, to b) an orientation imaging micrograph showing different grain orientations as different colors, to finite element meshes of c) the poly1/2 and d) the poly3 layers.

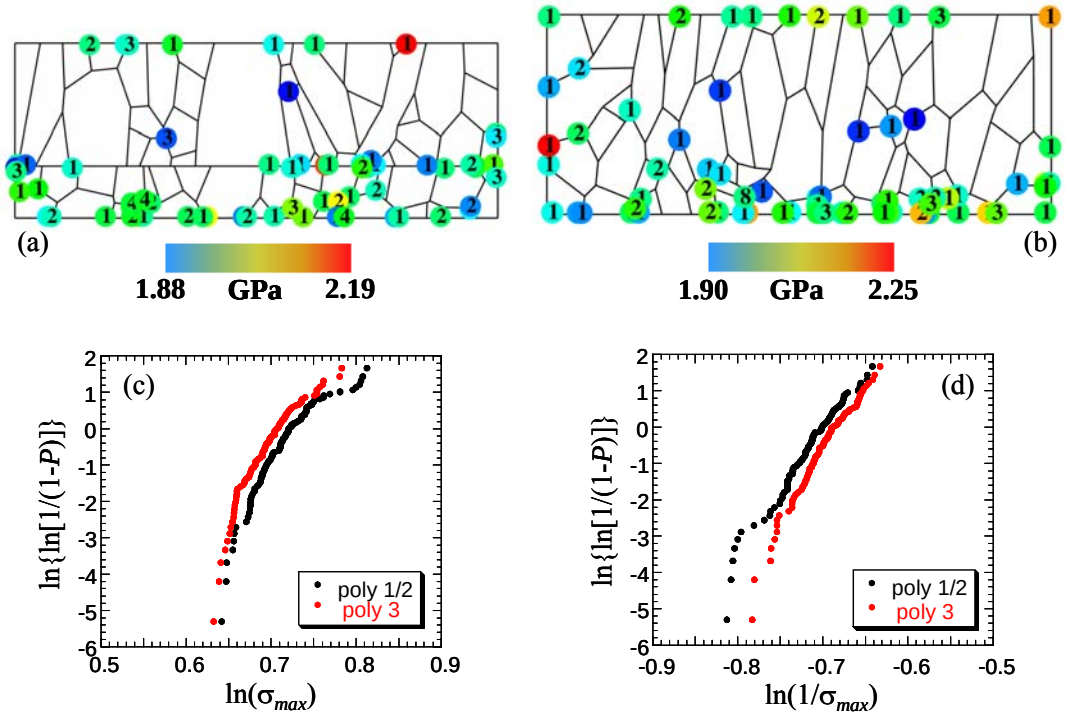

Figure 2. Results from one hundred tension simulations on each structure showing the locations of maximum von Mises stress in a) the poly1/2 and b) the poly3 microstructures, and the corresponding Weibull failure analyses using a) the maximum stress and b) the inverse of the maximum stress. The colors in a) and b) represent the stress magnitude, and the numerals denote the number of simulations that produced maximum stress at that location.

Automotive Lean-Burn NO_x Catalysis

E. N. Coker, J. E. Miller, D. A. Peña, R. S. Sandoval

Motivation: Lean-burn engines have been identified by U.S. automakers as the next major technological step in combustion engine design and fuel economy. By using more air during combustion, lean-burn engines yield better mileage and produce less carbon monoxide and unburned hydrocarbon pollutants than conventional gasoline engines. However, destruction of NO_x pollutants, which are produced by all engines, is more difficult in a lean-burn engine. Catalytic converters that were developed for conventional engines are not effective in lean-burn engines. For lean-burn engines to become commercially viable, novel catalyst technologies are needed. Similar catalysts may also find application for diesel engines, where highly oxidizing conditions in the exhaust stream demand similar advances in catalyst technology. The program, sponsored by the DOE Office of Transportation Technologies, is facilitated by separate CRADAs between the Low Emission Technologies Research and Development Partnership (General Motors, Ford and DaimlerChrysler) and Los Alamos, Oak Ridge and Sandia National Laboratories. Sandia is the technical lead for the three National Labs.

Accomplishment: Our initial goal was to develop hydrous metal oxide (HMO)-based catalysts to mitigate NO_x emissions in lean-burn engine exhaust. The flexibility of the HMO process chemistry allowed a wide variety of catalysts to be screened for activity in the selective catalytic reduction (SCR) of NO_x via hydrocarbon reaction using materials in bulk powder form. We fabricated and tested promising catalyst compositions on small-scale cordierite monoliths using HMO coating and ion exchange techniques. The best HMO-supported catalyst systems were further evaluated by scaling up the HMO-coating and ion-exchange processes to a full developmental size (110 cubic inch) catalytic converter (Fig. 1).

With the new Environmental Protection Agency (EPA) Tier II emission standards scheduled to phase in starting in 2004 (Fig. 2), we are now addressing new and potentially more efficient NO_x reduction options for lean-burn exhaust aftertreatment, in particular the SCR of NO_x by urea (or NH_3), which has been shown to provide excellent NOx reduction in stationary sources. To transition urea-SCR to mobile sources, several key parameters are under investigation, including the influence of space velocity, NO:NO_2 feed ratio, presence of residual hydrocarbons, temperature, and durability to sulfur poisoning and high-temperature excursions. Furthermore, catalyst formulations free from vanadium (which is used in stationary sources) are targeted for environmental reasons. We are also engaged in more studies related to determining the mechanism of the SCR of NO_x over different catalyst materials with various reductants, and are conducting mixed catalyst and support studies designed to optimize lean-burn NO_x catalysts.

Significance: Lab-scale catalyst testing protocols reflecting the transient nature of automotive exhaust chemistry have been successfully developed and implemented. The catalyst formulations developed have brought catalytic NO_x removal technologies for lean-burn engines closer to acceptance by EPA. Tests of developmental size hydrocarbon-SCR catalytic converters (Fig. 1) on a lean-burn engine dynamometer showed NO_x reduction activity rivaling a commercial benchmark catalytic converter. Total time from initial bulk screening to developmental size catalytic converter fabrication was less than 2 years.

Contact: Eric Coker, Chemical Synthesis & Nanomaterials Dept., 01846
Phone: (505) 272-7593
Fax: (505) 272-7304
Email: encoker@sandia.gov

Figure 1. Sandia-fabricated full developmental size (110 cubic inch) catalytic converter in take-apart can assembly.

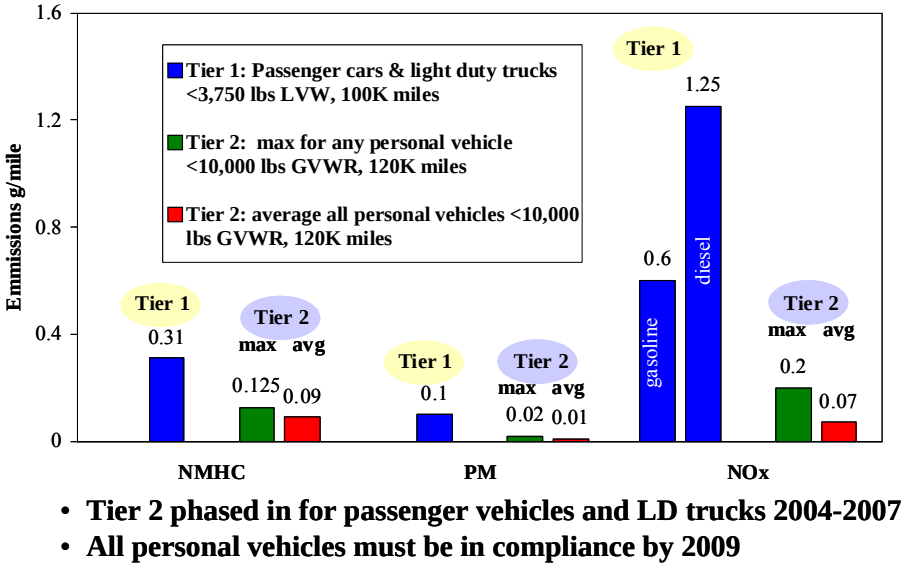

- **Tier 2 phased in for passenger vehicles and LD trucks 2004-2007**
- **All personal vehicles must be in compliance by 2009**

Figure 2. EPA Tier 1 and 2 standards for Non-Methane Hydrocarbon (NMHC), Particulate Matter (PM) and NO_x emissions from light-duty vehicles.

Unique Monoliths for Enhanced Catalytic Combustion

J. Stuecker, R. Ferrizz, J. Miller, J. Cesarano

Motivation: Monolithic catalytic reactors, widely utilized for environmental applications (automotive and stationary emissions control), are currently being considered for a variety of additional applications. Monoliths offer several advantages over traditional packed bed systems; perhaps the most significant of these is offering a high surface/volume ratio (similar to that of very small particles) with little resistance to flow (low pressure drop). Many of the potential new applications require very high gas flow rates (with space velocities up to 10^6 hr^{-1}). However, an inherent weakness of most monoliths is the potential for bulk gas-solid mass transfer limitations under high flow conditions.

We are utilizing a novel direct ceramic fabrication technique (robocasting) to produce 3-dimensional ceramic monoliths, e.g. meshes with controlled porosity in all dimensions but no line-of-sight pathways, which can function as catalyst supports for catalytic combustion, and self regenerating filters for diesel particulates. Compared to the traditional 2-dimensional "honeycomb" structured extrudates, our 3-dimensional structures promote higher mass transfer rates to catalytic surfaces while maintaining high surface to volume ratios, predictable permeability, and low pressure drop. In addition, robocasting allows for greater flexibility in materials, possibly alleviating problems related to thermal shock and chemical degradation.

Accomplishment: Using CO oxidation over Pt as a probe reaction, it has been shown that robocast monoliths with an “FCC-like” geometry of alternating rods (for which there are no direct line-of-sight pathways) exhibit superior mass transfer properties relative to traditional honeycomb monoliths (Figure 1 a,b). Robocast and honeycomb samples with identical dimensions, geometric surface areas, and catalyst loadings were both subjected to a high flow rate of 13,000 sccm (~750,000 hr^{-1}) of 1% CO in air. At 350 °C, it is evident from conversion vs. temperature plots that both samples are clearly in the mass-transfer-limited kinetic regime. CO conversion over the robocast sample was 99%, while it was only 75% over the honeycomb sample as seen in Figure 2. This corresponds roughly to a 3-fold increase in the Sherwood Number (a measure of convective mass transfer).

The reported gain in mass transfer was made at the expense of a significant increase in pressure drop. However much of this increase is due to the relatively small bulk porosity of the FCC sample (45%). A robocast sample that more closely matches the bulk porosity (74%), pressure drop, and surface area of the honeycomb monolith was tested and is shown in Figure 1c. This sample exhibits enhanced mass transfer properties (88% conversion at 350 °C) and no line-of-sight pathways.

Enhanced heat transfer (and mixing) is also more prevalent in robocast monoliths as shown by computational fluid dynamics modeling in Figure 3 (a,b) where two regions of gas (hot and cold) are kept separate up until the entrance of the monoliths. The cross-section views in Figure 3 (c,d) shows the enhanced mixing effect of the robocast monolith.

Significance: The superior properties exhibited by robocast monoliths could potentially reduce the amount of precious metals needed for reactions (enhanced mass transfer), preserve the catalyst by preventing thermal runaways (enhanced heat transfer), and prevent harmful reaction byproducts by ensuring reaction stoichiometry (enhanced ixing ponents).

Contact: Joe Cesarano, Ceramic Materials Dept., 1843
Phone: (505) 272-7624
Fax: (505) 272-7336
Email: jcesara@sandia.gov

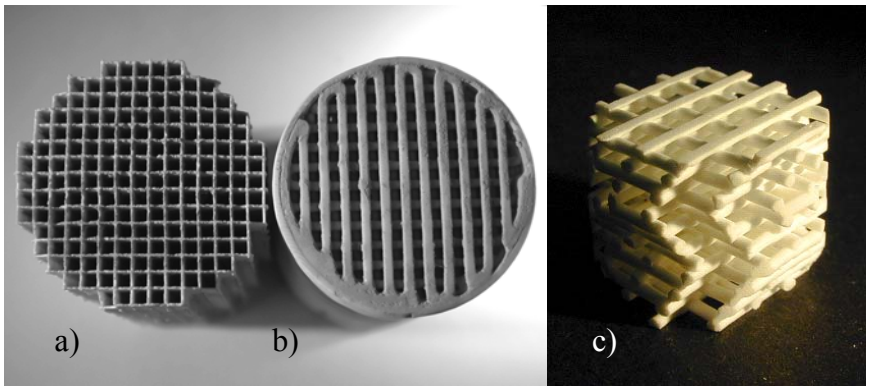

Figure 1. a) 75% porous honeycomb, b) 45% porous robocast FCC, c) 74% porous robocast modified FCC monoliths

Figure 2. CO conversion (750,0000 hr^{-1}) over Robocast FCC and honeycomb monoliths

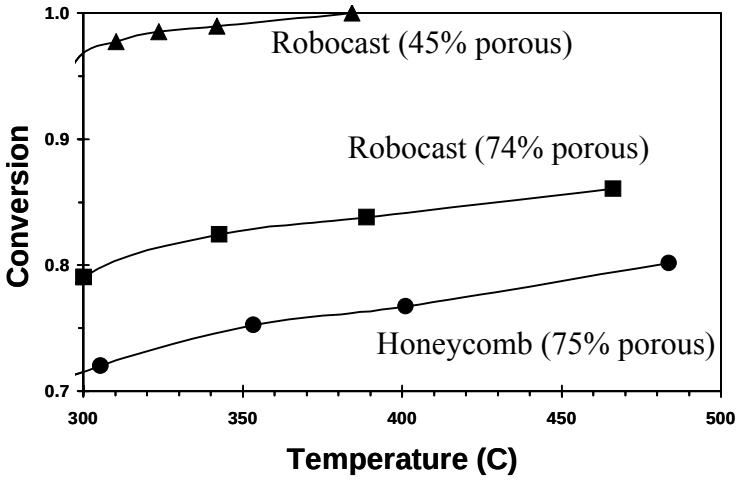

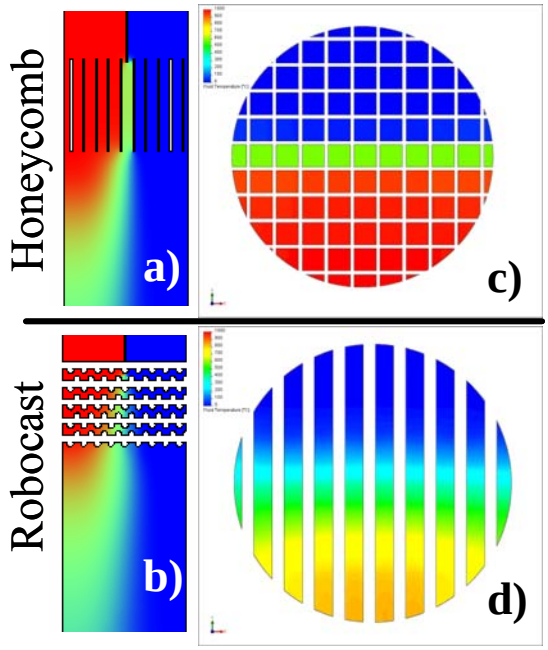

Figure 3. CFD model showing heat transfer/mixing along cross-sections of a) honeycomb and b) robocast monolith. Planar views c) and d) show temperature profiles at the exit of the monoliths.

Epitaxial Superconducting Wires by Chemical Solution Deposition

P.G. Clem, J.T. Dawley, J. Richardson, M.P. Siegal, J.A. Voigt, D.L. Overmyer

Motivation: A new method for high-rate deposition of epitaxial oxide films has been developed and applied to fabrication of low cost superconducting wires for power transmission and high magnetic field generation. The new architecture, termed 2nd generation coated conductors, may cost as little as $5-10 per kA-m, in contrast to 1st generation BSCCO/silver composites which may cost $200 per kA-m of power transmission. Both types of wire have been developed under the Department of Energy's Superconductivity Program for Electric Systems. The ultimate goal of the program is fabrication of superconductor-based wires for high magnetic field (1-10 Tesla) and current density (10^4-10^6 A/cm^2) applications, at a cost of $10/kA-m, which is competitive with the cost of copper, at $3/kA-m. The coated conductor wires possess performance advantages over copper for a number of technologies, including higher resolution MRI and NMR machines, more efficient electric motors, and higher density, loss-free electrical power transmission. In the current work, metal tapes up to km lengths may be dip coated with solution precursors and annealed to deposit $YBa_2Cu_3O_7$ (YBCO) films with current densities up to 1.3 MA/cm^2 at liquid nitrogen temperature (77K). The method may find application for high throughput (1000 km/year) production of superconducting wires.

Accomplishment: Chemical solution deposition (a.k.a. sol-gel or metal-organic decomposition) has been used at Sandia to develop the first all solution deposited 1 MA/cm^2 current density coated conductor architecture: YBCO/$SrTiO_3$/Ni tape (Figure 1). The process developed has the potential to be significantly less costly than alternative vapor phase methods of wire fabrication. A few of the key aspects of this process are shown in Figure 2. The solution deposition method enables coating at 3-10 cm/s, or > 1000 km/year. Novel precursor chemistries have been developed to enable rapid film deposition, solvent removal and crystallization, toward industrial production rates. In particular, methods of producing micron-thick YBCO coatings in fast (minutes) anneal times are under development. These technologies are available for license or commercial scale-up. Currently, the processes are being scaled up in conjunction with Oak Ridge National Laboratories, and coated conductor technical details are being jointly studied in research projects with Oxford Superconducting Technologies, American Superconductor Corporation, and MicroCoating Technologies.

Significance: Solution deposition methods are a potentially low cost (~$2/kA-m) and high throughput method of fabricating 2nd generation coated conductor wires. The current developments suggest promise for replacing existing metal and silver/BSCCO conductors in MRI, high current power conduits, and motor windings with a lower cost, more compact, higher-performance product.

Contact: Paul Clem, Microsystem Materials, Tribology & Technologies Dept., 1851
Phone: (505) 845-7544
Fax: (505) 844-9781
Email: mailto:pgclem@sandia.gov

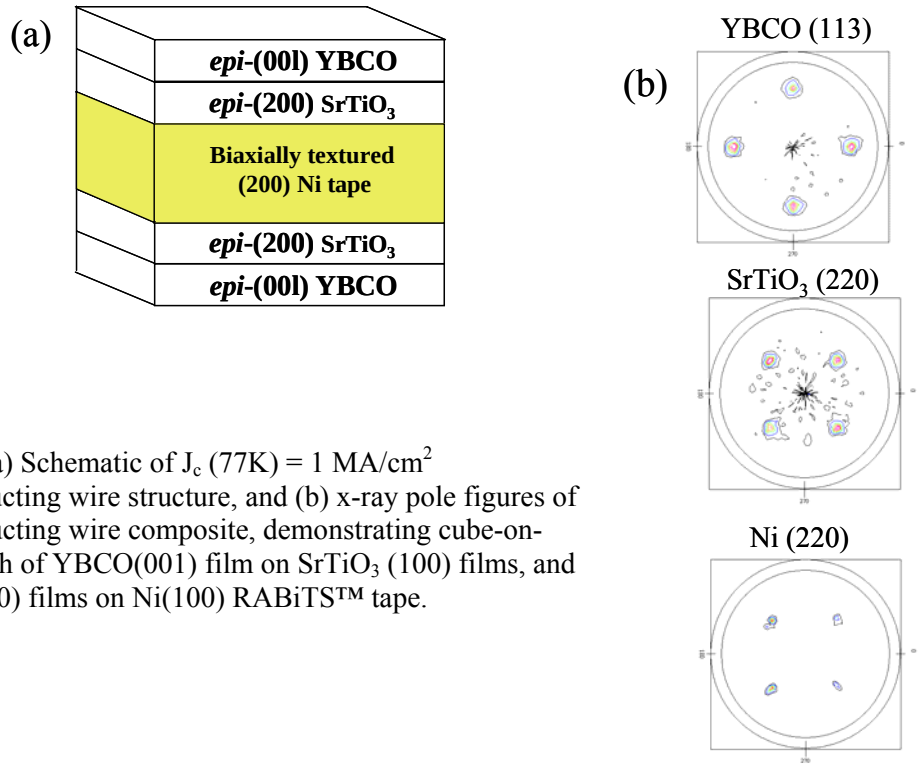

Figure 1. (a) Schematic of J_c (77K) = 1 MA/cm^2 superconducting wire structure, and (b) x-ray pole figures of superconducting wire composite, demonstrating cube-on-cube growth of YBCO(001) film on $SrTiO_3$ (100) films, and $SrTiO_3$ (100) films on Ni(100) RABiTS™ tape.

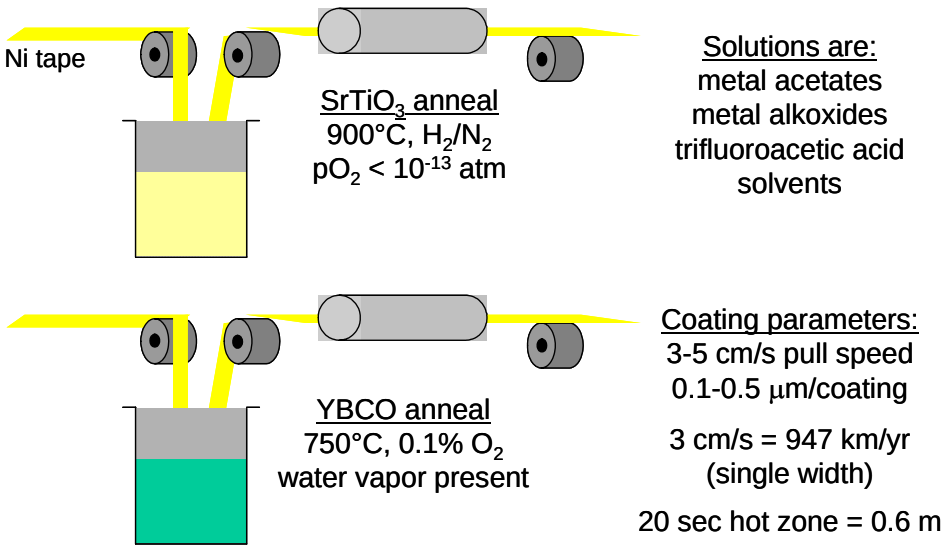

Figure 2. Schematic of continuous epitaxial film solution deposition process

Atomistic Modeling of the Deformation of Nano-scale Thin Films

S. M. Foiles

Motivation: The ability of integrated metal-semiconductor micro-systems to perform highly complex functions will depend on developing freestanding metal structures with desirable mechanical properties. This work models the deformation of freestanding metal films similar in texture and grain size to those produced via electrodeposition and being examined experimentally here at Sandia. The large-scale atomic-level simulations reveal the fundamental mechanisms involved in the tensile straining of freestanding films with nanometer scale grains. This understanding will aid the development of films with improved mechanical properties. In addition to this practical application, there is substantial scientific interest in understanding the deformation mechanisms in this class of materials. There is both experimental and computational evidence that deformation mechanisms that are not important for traditional metal samples may dominate the mechanical response at the nanometer scale. In particular, other molecular dynamics simulations of nano-grained metals point to the importance of grain boundary sliding and grain rotation in the deformation of nano-scale materials. This work complements these other studies by focusing on the influence of the free surfaces inherent in free-standing metal films.

Accomplishment: Atomistic simulations of the tensile loading of nano-grained thin films of Al have been per-formed. These simulations are based on large-scale molecular dynamics using embedded atom method potentials. Figure 1 shows the initial grain structure for a film with a strong [111] texture that was obtained via thermal annealing of the film structure. In this figure, only the atoms whose local environment deviates from the FCC crystal are shown. The continuous defects are high angle grain boundaries. The local areas are dislocations that form sub-grain boundaries. This film was subjected to tensile loading and the stress-strain curve computed. In order to address the role of the surfaces, these simulations have been performed for a variety of film thicknesses and for a periodically repeated film that approximates a bulk sample. Figure 2 shows the resulting stress-strain curves. Note that the coarse behavior of the films is very similar. Similar plots of the stored energy, though, show a strong dependence on the film thickness. The amount of stored plastic energy is relevant to the potential subsequent recrystallization of the film. Figure 3 shows the final film after deformation for the case of a very thin film. These figures can be analyzed to determine the microscopic nature of the defects that are created during deformation. It is important to note that the nature of the defects formed during the deformation does depend on the film thickness in the simulations. This corresponds to the observed differences in the stored energy.

Significance: The analysis of these simulations will reveal the fundamental mechanisms involved in thin film deformation at this scale. Ongoing work is further examining the role of film thickness and also exploring the importance of the film texture. The understanding produced from these simulations will provide insight into how the strength and stability of these materials can be improved.

Contact: Stephen Foiles, Materials & Process Modeling & Computation Dept., 1834
Phone: (505) 844-7064
Fax: (505) 844-9781
Email: foiles@sandia.gov

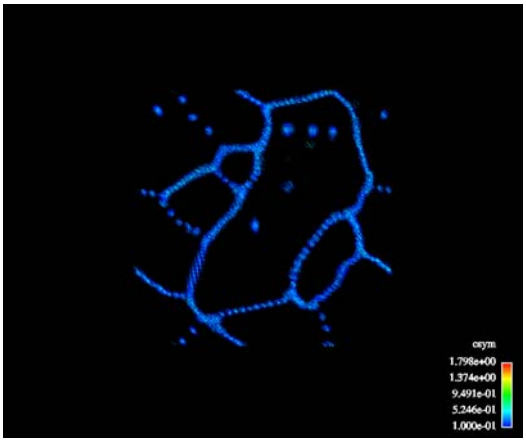

Figure 1. Simulated annealed structure of an Al thin film as determined by atomistic computer simulations. The structure is periodic in the plane of the figure. Only the atoms in non-ideal fcc environments are shown.

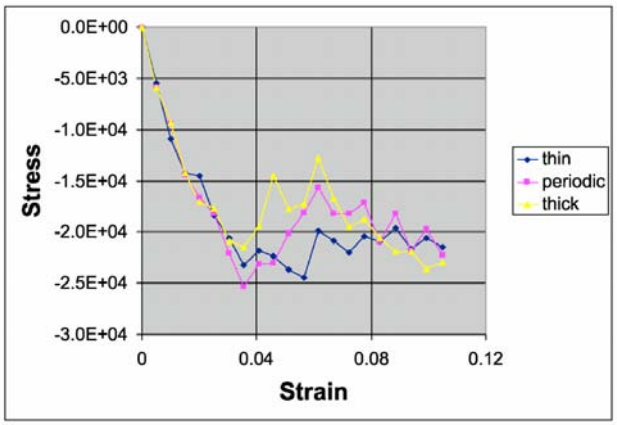

Figure 2. Computed stress-strain curves for tensile elongation of thin films such as in Figure 1. The results compared films of different thickness as well as periodically extended in the direction normal to the plane. Note the coarse similarity in the results.

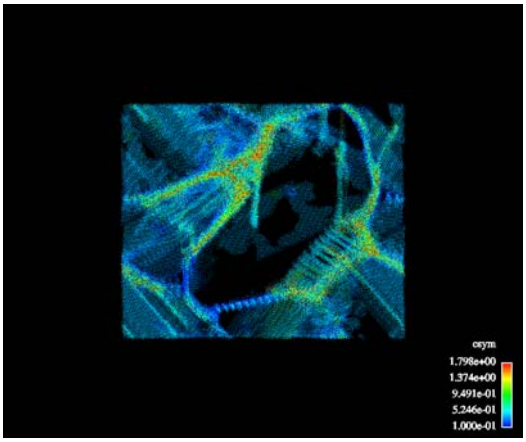

Figure 3. The final structure of the thin film after deformation as in Figure 1. Note that the nature of the final structure is strongly dependent on film thickness.

Controlled Synthesis of Nanoparticles

T. J. Boyle, S. D. Bunge

Motivation: In order to make the advances predicted by nanotechnology, it is necessary to be able to synthesize nanoparticles in controlled sizes, shapes, phases, stoichiometry, and other properties. In order to accomplish this, it is necessary to understand how to manipulate the various properties of the precursor to affect the final materials. We have undertaken this for metals, alloys, semiconductors, and ceramics.

Accomplishment: Using literature and some of our novel routes, we have at our disposal, a variety of mixed shaped nanoparticles of numerous metals. Figure 1 shows several representative structures and metals we have isolated. We have recently used the concepts of metalorganic chemical vapor deposition (MOCVD) to discover a new class of compounds for nanoparticle synthesis. These mesityl derivatives have been shown to generate high quality nanoparticles of metals in a relatively simple preparation. We have also extended this approach to metal amides and metal alkoxides. In addition to metals, we have also developed routes to alloys. While this is still preliminary we have shown we can make Pt/Ir, Cu/Au, Fe/Pt nanomaterials that by XRD, UV-*vis*, and TEM analysis prove conclusively that we have made alloys.

One of the most widely studied nanoparticle systems are CdE (E = S, Se, Te) often referred to as quantum dots. Control over the properties of these materials (i.e., size, shape, and arrangement) are critical to the fulfillment of the development of devices. We have studied the changes of the formation of CdE from CdO over time and found for E = S dots are formed, = Se rods are formed (Figure 2a) and = Te tetrapods are isolated (Figure 2b). The CdSe rods were found to form tracks of over 1μm in length.

We have investigated routes to ceramic materials and then attempted to exploit them using structural variations in the precursor. Shown in Figure 3 is one such study wherein we synthesized and characterized numerous zinc ethyl alkoxides with different nuclearities. These were then used in a novel methyl-imidazole water (95:5) mixture to generate ZnO nanomaterials. For the monomeric system (Figure 3a) dots were isolated but for the higher nuclearity (Figure 3b-c) it appears that rods that increase in size with increased nuclearity are isolated. We have initiated our investigation into complex ceramic materials using novel multi-cationic metal alkoxide precursors.

As these simple systems become more routine, we are extending our research into more complex nanoparticles. In particular, we are developing routes to core-shell materials. Shown in Figure 4a, CdS@CdSe materials which passivate the surface allow for sharper signals for photonic devices For Figure 4b, Er-doped SiO_2@Au nanoparticles which we are using for luminescent studies on controlled assembled silica spheres. To do this, it was necessary to synthesize and characterize a series of $Ln(OR)_3$ species and we have isolated over 40 novel compounds. Additionally, we are interested in TiO_2 coated nanoparticles for light activated decomposition of organic and inorganic species. In order to accomplish this we have developed several sterically hindered species such as $Ti(OPy)_2(OPr^i)_2$ which was used with an amino-alcohol surfactant to generate a TiO_2@CdSe. (Figure 4c)

Significance: With the diverse type of nanoparticles, we can contribute to the development of nanodevices. In particular we are working on making nanoparticles for active photonic devices, biolabel imaging, catalytic decomposition species, and many others.

Contact: Tim Boyle, Chemical Synthesis & Nanomaterials Dept., 1846
Phone: (505) 272-7625
Fax: (505) 2727336
Email: tjboyle@Sandia.gov

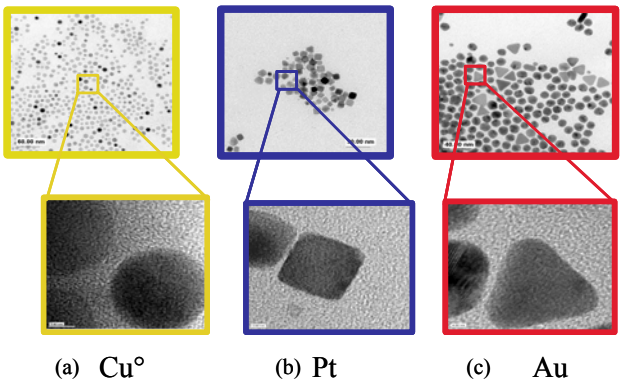

Figure 1. Controlled structures of oxide free metal nanoparticles (a) Cu° spheres, (b) Pt° cubes, (c) Au° triangles. Other shapes with different metals are also available.

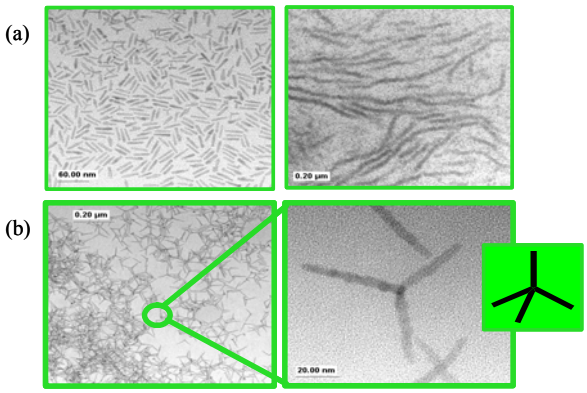

Figure 2. Using $Cd(O_2CCH_3)_2$ and CdO, CdE materials of distinct shapes: (a) rods of CdSe which assemble into tracks over 1 µm in length and (b) tetrapods of CdTe.

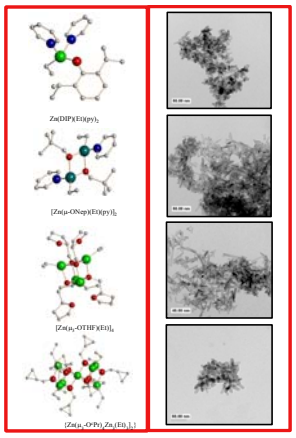

Figure 3. Using select precursors: row i:(a) Zn(DIP)(Et)(solv) (over 16 monomeric species with variety of ligands available), (b) $[Zn(\mu\text{-}ONep)(Et)(py)]_2$, (c) $[Zn(\mu_3\text{-}OTHF)(Et)]_4$, (d) $\{Zn(\mu\text{-}O^cPr)_4Zn_3(Et)_3]_2\}$ the resulting nanorods of ZnO were isolated row ii.

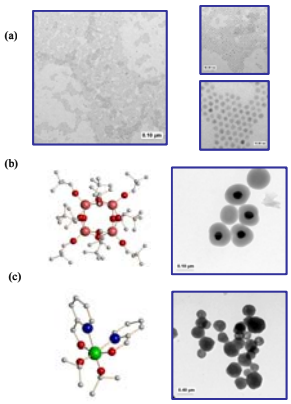

Figure 4. Core Shell materials (a) CdS@CdSe, (b) $[Er(\mu\text{-}ONep)_2(ONep)]_4$ precursor for Er-doped SiO_2@Au, and (c) $Ti(OPy)_2(OPri)_2$ for TiO_2@CdSe

Nanoparticle Nucleation and Growth in a Microfluidic Reactor

T.L. Sounart, J.A. Voigt, J.E. Bickel, D.R. Tallant, C.M. Matzke, T.A. Michalske

Motivation: Nanoparticles have wide ranging potential applications such as advanced computing, chemical and biological analysis/detection, drug delivery/discovery, tissue engineering, catalysis, and energy conversion and storage. However, the current ability to control nanoparticle properties is at a state of infancy, and there is a general lack of fundamental understanding of the nucleation and growth processes. Traditional batch operations not only involve extreme synthesis conditions with poor control of thermal, chemical, and fluid transport, but also lack in-situ monitoring and feedback mechanisms for obtaining critical information on the reaction pathways. Here, a continuous-flow microfluidic reactor has been applied to control process variables and provide time-resolved monitoring of CdS quantum dot (QD) nanoparticle growth.

Accomplishment: Microfluidic technology involves the manipulation of fluids in microfabricated devices with channel length scales on the order of one to hundreds of microns. On these length scales, laminar flow and high heat transfer rates can be exploited to exercise unparalleled control over fluid, mass, and energy transport. In addition to providing better control of reactor conditions, microfluidic systems provide a unique platform for investigation of fundamental reaction processes. CdS QD growth, which is too fast to observe transiently, has been resolved spatially in a continuous-flow microreactor. Using a two-feed stream system (Fig. 1), an aqueous solution containing $CdSO_4$ is continuously fed into one side of a rectangular microchannel while a solution containing Na_2S is fed into the other. The laminar flow of the impinging streams allows for controlled diffusional mixing of the reacting cadmium and sulfide ions at the boundary between the two solutions. The solution contact time, and therefore reaction time, increases along the channel axis (from zero at the solution confluence).

Using spatially resolved fluorescence imaging and spectroscopy of the solution-solution interface coupled with varying reactant concentrations and flow rates, kinetic data on cysteine-mediated CdS particle growth have been obtained. Figure 2 shows a CdS photoluminescence intensity distribution during growth in the microchannel. The intensity increases and the peaks spread with increasing reaction time, as nuclei accumulate and particles diffuse away from the solution interface. The Gaussian shape of the CdS concentration profile suggests diffusional transport is the rate-limiting step. Fluorescence spectroscopy measurements show an early (< 1s) bimodal distribution (Fig. 3), and a red shift in the photoluminescence spectrum during the first few seconds of reaction (Figs. 3 and 4), after which little change in the emission spectrum is observed. These data are also qualitatively consistent with diffusion-limited reaction kinetics except in a developing region near the solution confluence. Microreactor models are now being developed to quantitatively interpret reactor data.

Significance: Chemically synthesized QD growth has been observed on subsecond time scales for the first time using a microfluidic platform. Improved experimental techniques are now being developed to observe nucleation and growth on even shorter time scales. Fundamental studies with other chemistries and reactor geometries will be applied to learn how to better control nanoparticle properties.

Contact: Thomas Sounart, Chemical Synthesis & Nanomaterials Dept., 1846
Phone: (505) 845-0946
Fax: (505) 844-5470
Email: tlsouna@sandia.gov

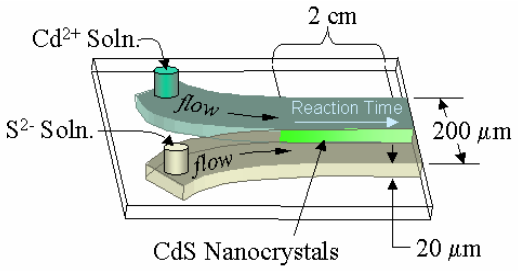

Figure 1. Sketch of continuous-flow microfluidic reactor for *in situ* analysis of CdS growth.

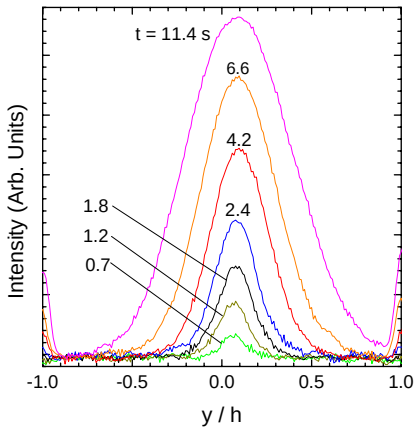

Figure 2. Cysteine-mediated CdS photoluminescence intensity profiles at selected reaction times (axial positions) in microfluidic channel. y is the distance from the solution boundary. Channel half-width h = 100 μm; flowrate = 200 nL/min, $[Cd^{2+}]$ = 0.025 M, S:Cd = 1:1, Cys:Cd = 2:1. Mercury lamp excitation at 360 nm.

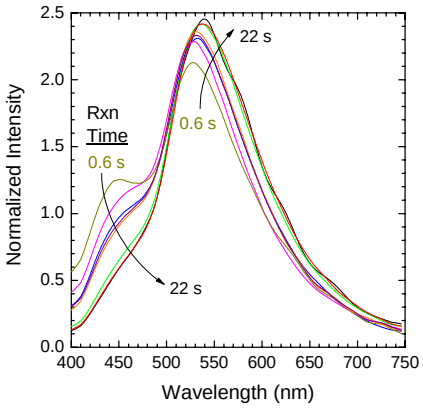

Figure 3. Normalized (by mean) photoluminescence spectra at selected reaction times. Flowrate = 200 nL/min, 2 μL/min. Laser excitation at 350-360 nm. All other conditions as for Fig. 2.

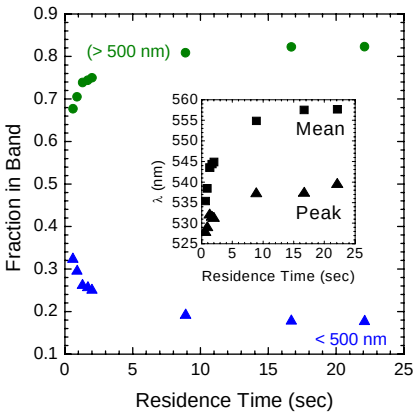

Figure 4. Time-dependence of photoluminescence red-shift. Fraction of CdS fluorescence greater than or less than 500 nm obtained by integration of the emission spectra. All conditions as for Fig. 3.

Self-Assembly and Integration of Ordered, Robust, Three-Dimensional Gold Nanocrystal/Silica Arrays

H. Fan, J. Brinker

Motivation: Develop methods to synthesize monodisperse nanocrystals (NCs) in aqueous conditions providing the ability to create robust multifunctional NC arrays for development of collective eletronic/photonic behavior and controlled catalysis.

Accomplishment: We have developed the direct synthesis of water-soluble nanocrystalline gold micelles (NC-micelles). Our concept is to consider organically-passivated nanocrystals as large hydrophobic molecules that, if incorporated individually into the hydrophobic interiors of surfactant micelles, would result in the formation of NC-micelles composed of a metallic (or other) NC core and a hybrid bilayer shell with precisely defined primary and secondary layer thicknesses (see Fig.1H). The hydrophilic NC micelle surfaces would cause them to be water-soluble and allow further assembly or derivitization as depicted in Fig. 1. To individually incorporate NCs in surfactant micelles and realize this concept, we developed a micro-emulsion procedure. A concentrated nanocrystal solution in organic solvent is added to an aqueous solution of surfactant under vigorous stirring to create an oil-in-water micro-emulsion. Organic solvent evaporation transfers the NCs into the aqueous phase by an interfacial process driven by the hydrophobic van der Waals interactions between the primary alkane of the stabilizing ligand and the secondary alkane of the surfactant, resulting in thermodynamically defined interdigitated bilayer structures. For single-tailed surfactants, an alkane chain of eight or more carbons is required to form micelles with gold nanocrystals stabilized by C_{12} alkanethiols. Cationic, anionic, and non-ionic surfactants can all form NC-micelles. In addition, fluorescent semiconducting CdSe NCs have been formed into NC-micelles with maintenance of optical properties. NC-micelle solutions are colored and indefinitely stable (>2-years). We have synthesized a new NC/silica mesophase through self-assembly of water-soluble NC-micelles with silica. The mesophase comprises gold NCs arranged within a silica matrix in a face-centered-cubic lattice with cell dimensions that are adjustable through control of the nanocrystal diameter and/or the alkane chain lengths of the primary alkanethiol or the surrounding secondary surfactants. Under kinetically controlled silica polymerization conditions, evaporation drives self-assembly of NC-micelles into ordered NC/silica thin film mesophases during spin-coating (Fig. 2). Initial studies of charge transport within such ordered gold NC/silica films show non-linear current-voltage behavior at low temperature and complete Coulomb Blockade at 78k. Linear Arrhenius plot at zero bias conductance testifies both to the uniformity of NC sizes and to the dominance of charge transport mechanism at room temperature. Calculated activation energy is U=90.4mev. By measuring the *I-V* characteristics at T>the threshold temperature, we established for the first time current voltage scaling relationship for a well-defined 3-D array, $I \sim V^{2.9}$.

Significance: The new method invented is a very simple, one-step process to self-assemble hydrophobic nanocrystals into water-soluble micelles. The flexibility of incorporating functional groups on the outer micelle surface should enable these water soluble nanocrystals to efficiently couple with DNA or proteins for biomolecular tagging. The formation of highly ordered robust arrays with controlled nanocrystal spacings and high particle loadings provides great opportunities in the development of new quantum solids with unique optical, electronic, and magetic properties.

Contact: Hongyou Fan, Chemical Synthesis & Nanomaterials Dept., 1846
Phone: (505) 272-7128
Fax: (505) 272-7336
Email: hfan@sandia.gov

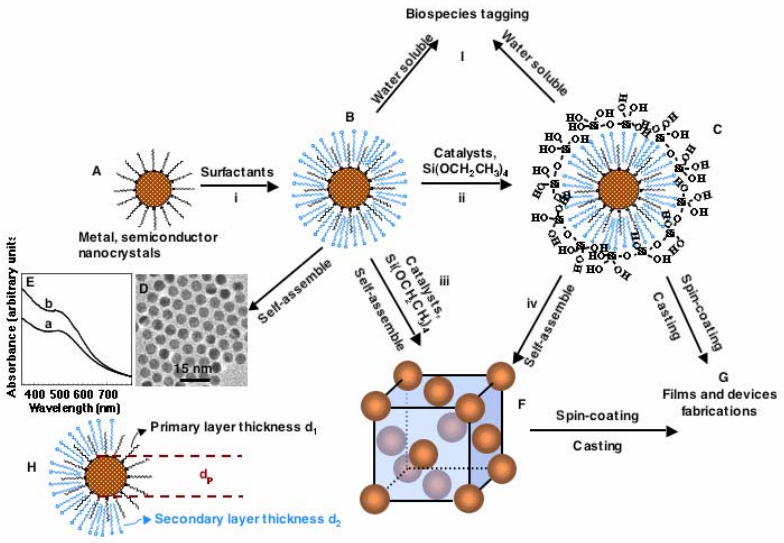

Figure 1. Processing diagram for the synthesis of water-soluble gold nanocrystal micelles and periodically ordered gold NC/silica mesophases. (A) Gold nanocrystals were prepared according to the method of Brust *et al*, using 1-dodecanethiol (DT) as a stabilizing agent. Heat-treatments were employed to further narrow the particle size distributions. (B) Thiol-stabilized nanocrystals are encapsulated in surfactants to form water-soluble NC micelles that, upon evaporation, self-assemble to form hexagonally-ordered NC arrays as shown in the TEM image (C).

(D) UV-visible spectra of (a) gold nanocrystals in chloroform and (b) gold NC-micelles in water both exhibit plasmon resonance bands at 510-cm^{-1}. (E) Silicic acid moieties formed by hydrolysis of TEOS are organized at the hydrophilic surfactant-water interface of NC micelles, leading, under basic conditions, to a gold NC/silica mesophase (F) composed of NCs organized in a periodic FCC lattice within a dense silica matrix. (G) Under acidic conditions that suppress siloxane condensation, spin-coating or casting result in ordered thin film NC/silica mesophases that are readily integrated into devices. (H) The lattice constant of the NC/silica mesophase is controlled by the nanocrystal size (d_p), the primary layer thickness of the alkanethiol, d_1, and/or the secondary layer thickness of the surfactant, d_2. I. Polyethylene glycol-surfactants or lipids can be used to prepare biocompatible water-soluble NC micelles for biolabeling.

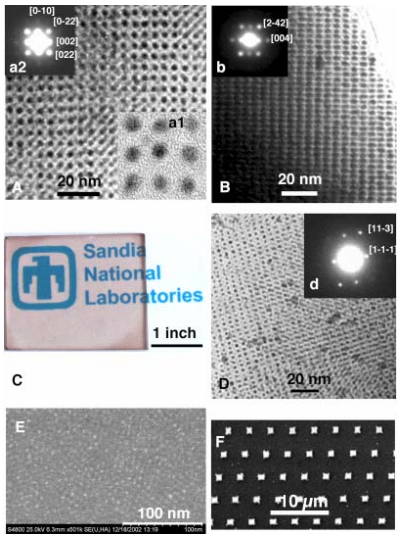

Figure 2. Representative transmission electron microscope (TEM) images of gold nanocrystal/silica mesophases. (A) and (B) [100] and [210] orientations of bulk samples prepared according to pathway i-ii-iii (Fig 1). Inset (a1): high resolution TEM of sample (A) showing gold NC lattice fringes. Inset (a2): selected area diffraction pattern from the image in (A). Inset (b) selected area electron diffraction from the image in (B). (C) Optical image of ordered gold NC/silica thin film spin-coated on glass. (D) TEM image of [211]-oriented NC/silica thin film mesophase. Inset (d) selected area diffraction pattern from image in (D). (E) Scanning electron microscope plan-view of ordered gold NC/silica films. (F) Patterned ordered gold NC/silica films through μ-molding.

Solution-Based Nanoengineering of Materials

R. Tian, J. Liu, T. Boyle, L. Criscenti, R. Cygan, J. Voigt

Motivation: Solution-based synthesis is a powerful approach for creating nano-structured materials. Although there have been significant recent successes in its application to fabricating nanomaterials, the general principles that control solution synthesis are not well understood. The purpose of this project is to develop the scientific principles required to design and build unique nanostructures in crystalline oxides, II/VI semiconductors and other materials using solution-based molecular self-assembly techniques. The ability to synthesize these materials in a range of different nano-architectures (from controlled morphology nanocrystals to surface templated 3-D structures) will provide new opportunities for the development of interactive interfaces for optics, electronics, and sensors.

Accomplishment: Having chosen homogeneous precipitation of ZnO in aqueous solution as a model system, we developed a low temperature, environmentally benign, solution based approach to prepare complex and oriented ZnO nanostructures. Through controlled seeded growth, with simple citrate anions selectively adsorbing on ZnO basal plane surfaces as structure-directing agent, we prepared large arrays of oriented ZnO nanorods with controlled aspect ratios. The architectured films consisting of oriented nanocolumns and nanoplates are remarkably similar to biomineral structures in red abalone shells (see Figure 1, for example). These unique architectured ZnO films showed novelties in photocatalytic decompositions of volatile organic compounds (VOC).

In order better understand how specific growth modifying agents interact with specific crystallographic faces and to eventually develop predictive and modifier design tools, we have extended our molecular modeling capabilities to oxide surfaces and ligand adsorption. Again using the ZnO system as our model system, we developed representative periodic models for the three primary zinc oxide growth surfaces, (100), (101), and (001) in which surface oxygens were protonated as expected in an aqueous solution at 25°C and pH 7. Two-dimensional molecular mechanics calculations were used to derive relative binding energies of several different adsorbates on each of the zincite surfaces. Each zinc oxide surface was initially equilibrated to allow for complete surface relaxation, then optimized configurations and binding enthalpies for each adsorbate-surface system were obtained (see Figure 2 for the case of citrate adsorption).

The film growth approach developed for the ZnO system has been applied to several other material systems to produce oriented nanostructures, including conductive polymers, TiO_2 nanowires, and mesoporous silicates. For example, a novel hierarchical and self-similar crystal-growth process has been used to produce controlled morphology mesoporous silicate film structures with ordering from the nano- to macro-scale (see Figure 3 for a few examples).

Significance: Extended and oriented nanostructures are desirable for many applications, including microelectronic devices, chemical and biological sensing and diagnosis, energy conversion and storage (photovoltaic cells, batteries and capacitors, and hydrogen storage devices), light emitting display, catalysis, drug delivery, separation, and optical storage.

Contact: Jim Voigt, Chemical Synthesis & Nanomaterials Dept., 1846
Phone: (505) 845-9044
Fax: (505) 844-9781
Email: javoigt@sandia.gov

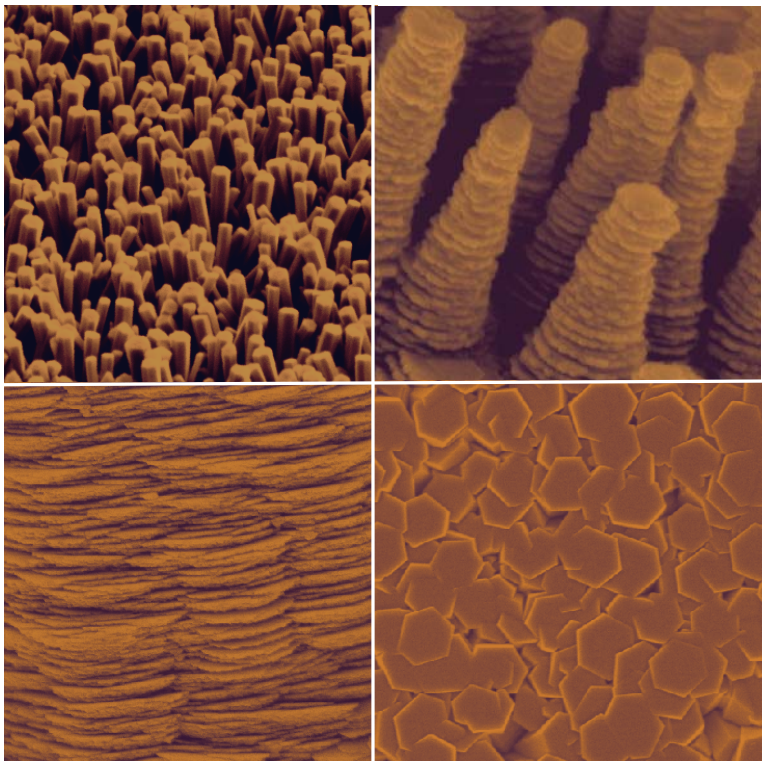

Figure 1. SEM photomicrographs of: a) nanoplate growth of ZnO and b) plate-like structure of layered abalone nacre ($CaCO_3$).

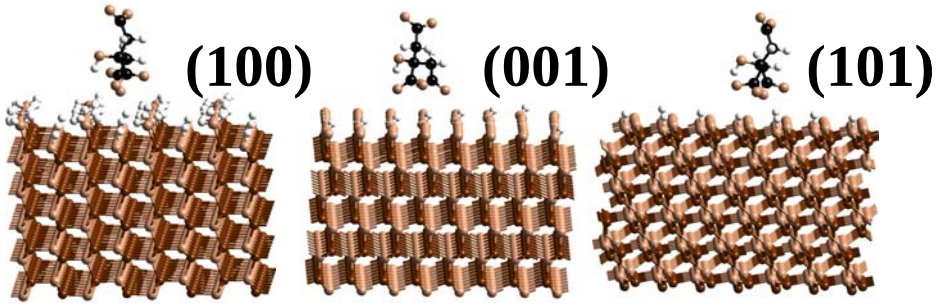

Figure 2. Optimized configuration of citrate adsorbed onto each of the three zinc oxide surfaces.

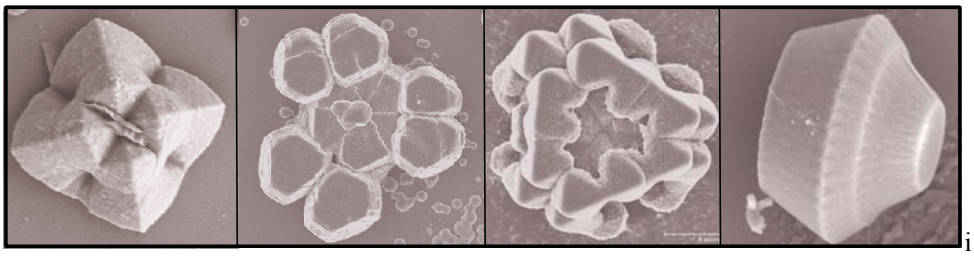

Figure 3. SEM photomicrographs of a sampling of the crystal morphologies and hierarchal structures of mesoporous silicates grown on glass substrates.

Non-Aqueous Gels for Sensors and Weapons

J. Lenhart, P. Cole

Motivation: A gel is a cross-linked polymer highly swollen by solvent. Mechanically the solvent creates a "soft solid", which is easily deformable yet still recovers from deformation due to the elastic nature of the cross-links in the polymer. While polymer gels have potential use in a variety of emerging technical applications including drug delivery, medical implants, artificial muscles, food and cosmetics, separation systems, display devices, batteries, and optical devices to name a few, of particular interest to Sandia are gel applications in sensors, and electronic devices. While varying solvent types and loading provides a wealth of applications, the high solvent loading invokes unique materials challenges because solvent-polymer partitioning and the resulting gel microstructure, largely determines the gel properties. Non-aqueous based gels are the focus as a broad temperature requirement and other material constraints render aqueous base gels useless for our applications.

Accomplishment: Polymer gels are proposed as replacement technology for several applications. In late FY02, components utilizing gel technology were exhibiting nearly 100% device failures. A sequence of gel modifications in FY03 has resulted in nearly 100% success in component testing. Analysis of the failed components and gel characterization confirmed that device failures were due to gel delamination from a substrate. Figure 1 plots the storage modulus of the initial gel formulation as a function of temperature and solvent loading. The main graph shows the temperature range used in the component. The inset shows a larger temperature range. A dramatic increase in the gel modulus occurs at the lower temperature requirements for the devices, as the gel approaches its glass transition temperature. Stress development at the gel-substrate interface at cold temperatures was the cause of the device failures. In order for the device to function, a new gel was designed with a lower plateau modulus, lower glass transition temperature, and enhanced adhesion-tack. Three modification strategies were used to designed gels with improved performance including: reducing the polymer cross-link density, incorporating pendant functional groups in the polymer chains, and switching solvents to provide improved polymer-solvent miscibility. Figure 2a compares the storage modulus of the old gel with the new gel. The glass transition of the new gel is 20 ºC lower than the old gel material. The modulus of the new gel is more than an order of magnitude lower over the entire use range of the component. Figure 2b plots tan δ (loss/storage modulus) versus temperature for the old and new gels. The large peak in tan δ indicates the glass transition of the gels. With the new gel, a secondary hump in tan δ is observed near –40 ºC, indicating enhanced energy dissipation in that temperature vicinity. We correlated the height of this secondary hump with increased gel adhesion-tack and improved device performance. The molecular mechanisms leading to the secondary hump are under investigation.

Significance: Polymer gels can exhibit a volume phase transition in response to changes in the external conditions. For the current devices we designed a gel that does not exhibit this shrinking transition over required temperature ranges. For future applications in sensors and micro-pumps, valves, etc., we will design gels to undergo rapid and reversible volume shrinkage in response to changes in the external environment such as temperature, chemical-biological toxin absorption, electrical-magnetic stimuli, etc.

Contact: Joseph Lenhart, Organic Materials Dept., 1811
Phone: (505) 284-9209
Fax: (505) 844-9781
Email: jllenha@sandia.gov

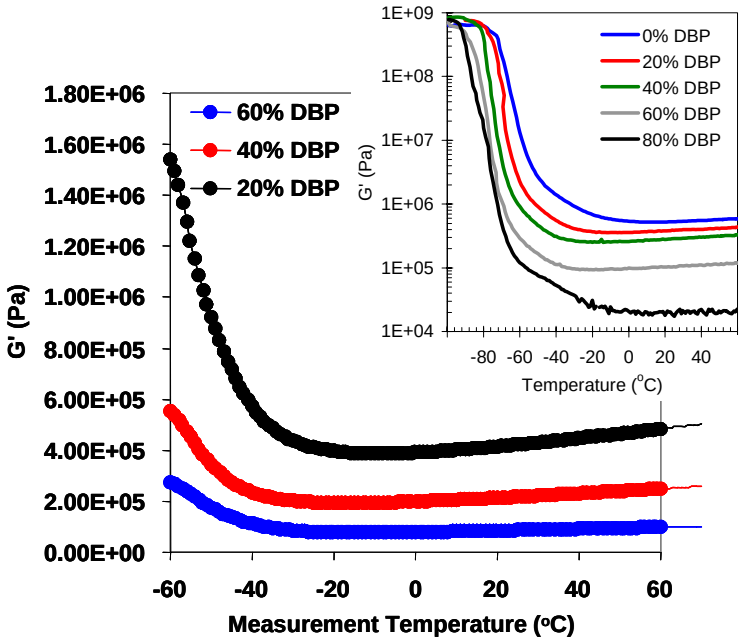

Figure 1. The storage modulus of the gel is shown as a function of temperature and solvent loading. The main graph shows the temperature range of the gel based devices. The inset shows a broader temperature range including the gel glass transition temperature.

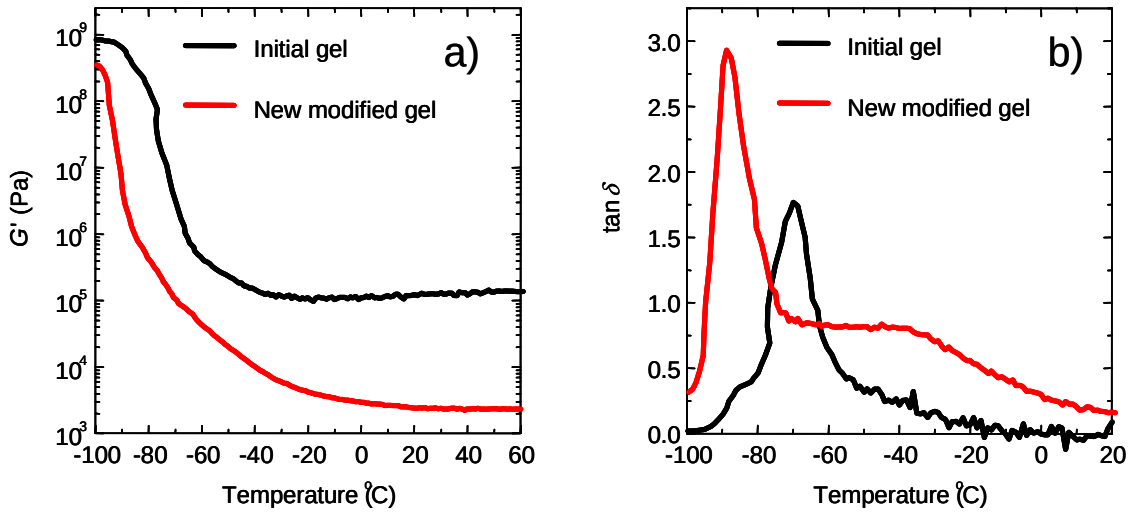

Figure 2. a) storage modulus of the old and new gel material b) tan δ of the old and new material.

Removable Epoxy Conformal Coatings and Adhesives

J. H. Aubert, P. S. Sawyer

Motivation: There are occasions when a conformal coating is desired on printed wire boards (PWB) for environmental protection of weapon electronics. A variety of commercial conformal coatings could be utilized for this application. A contrasting requirement on new weapon electronics is that the conformal coating be totally removable when desired. Such occasions might occur if there is an electronic malfunction during development, during production, or even after deployment. Additionally, clean removal of the conformal coating could be advantageous for surveillance and for dismantlement. There are few commercial conformal coatings that allow removal and none that satisfy our additional requirements that are not described here.

We have developed a new removable conformal coating to address these needs. The coating is based upon epoxy chemistry and thermally-reversible Diels-Alder adducts. The removable conformal coating is also being applied as a removable adhesive for some applications.

Accomplishment: The removable conformal coating was formulated with a diepoxy resin that contains two Diels-Alder (D-A) adducts as shown in Figure 1. Details of this synthesis are described elsewhere.[1] The diepoxy resin is mixed with a commercial diepoxy resin and cured with a mixture of three commercial curatives. Two of the curatives are diamines and the other is a plastizer. The formulation, (RCC200), is described in Table I.

A PWB is conformally coated by first mixing the resins and curatives at 70 °C. When at temperature and well mixed, the conformal coating is poured into 10 cm^3 syringes. Entrapped air bubbles are removed by centrifuging the syringes. The conformal coating is then dispensed over the printed wire board. The thickness of the coating is related to the temperature of cure – thicker coatings are obtained with room temperature cure and thinner coatings are obtained with a cure of 60 °C. The cure time varies with temperature – 16 hours at room temperature and 4 hours at 60 °C.

The coatings are elastomeric due to the use of the long-chain aliphatic curatives described in Table 1. The glass transition temperature is –5 °C. The conformal coating is bubble-free and clear with a slight amber color, Figure 2.

The conformal coating dissolves in 1-butanol at 90 °C. This mild condition allows the coating to be removed without damage to the PWB or its components. The removal process takes advantage of the thermally reversible D-A adducts. It has been reported that the D-A adduct forms below 60 °C and reverses above 90 °C as shown schematically in Figure 3. In actuality, the D-A adduct is a reversible process with an equilibrium constant that can be described by $K = K_o \exp[A/T]$, with T in K[2]. For a resin similar to RER 1, the equilibrium constant has been measured to be 413 at 60 °C and 36 at 90 °C. There are sufficient open adducts at 90 °C to be solvated by 1-butanol which effectively opens them irreversibly.

Significance: A removable conformal coating has been demonstrated that allows for the rework of PWBs when desired. The removal process is based upon the use of thermally-reversible Diels-Alder adducts incorporated into a diepoxy resin.

[1] McElhanon, J. R., Russick, E. M., Wheeler, D. R., Loy, D. A., and Aubert, J. H., J. Appl. Polym. Sci., **85**, 1496-1502 (2002).
[2] unpublished FTIR/chemometrics data obtained by D. R. Tallant and M. M. Garcia, Sandia National Labs, 2003.

Contact: Jim Aubert, Organic Materials Dept., 1811
Phone: (505) 844-4481
Fax: (505) 844-9624
Email: jhauber@sandia.gov

TABLE I. Formulation of removable conformal coating, RCC200.		
RESIN	**CURATIVE**	
RER 1 (Figure 1.)		41.07%
EPON® 8121		13.69%
	JEFFAMINE® 230	5.69%
	JEFFAMINE® 2000	32.48%
	NONYLPHENOL	7.07%

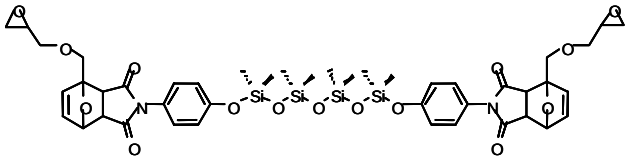

RER 1

Figure 1. The diepoxy resin, RER 1, containing two Diels-Alder adducts.

Figure 2. PWB with a thick coating of RCC200

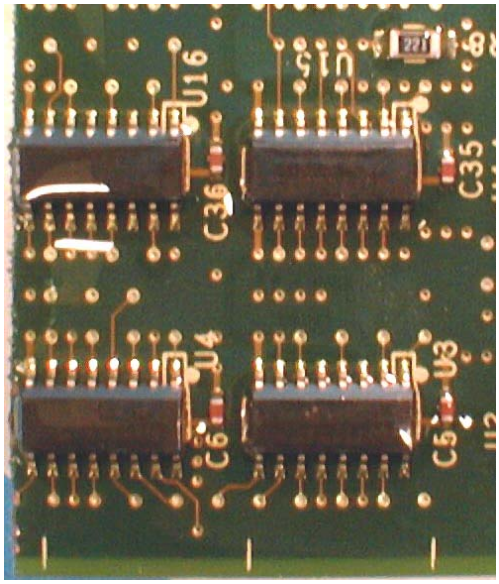

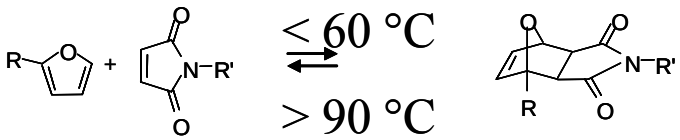

Figure 3. Schematic of the reversible Diels-Alder adduct formation and the temperatures at which the equilibrium shifts from primarily forward to primarily retro.

Removable Foam Encapsulant Technology

E. Russick, J. Aubert, M. Stavig, P. Sawyer, T. Huber

Motivation: Foam encapsulants are used in weapon systems primarily to mitigate shock and vibration incurred by electromechanical components. However, when malfunctions of encapsulated systems take place or retrofitting is necessary, conventional encapsulants are not removable except with very aggressive solvents or by mechanical means that risk damaging sensitive equipment. For decades, there has been a desire for removable encapsulants that would allow for damage-free depotting of components in weapon systems. After depotting, components could be reworked or repaired, then repotted for future use. Removable foam technology would be particularly useful for systems that are extremely expensive to replace.

Accomplishment: The Materials and Process Sciences Center encapsulation team has developed removable encapsulant technologies that allow for the depotting, reworking, repair, and/or replacement of components. A new removable epoxy resin that utilizes Diels-Alder reversible chemistry has been synthesized which, when incorporated into conventional epoxy foam formulations, results in a removable foam (REF300) that dissolves in a mild solvent (e.g., n-butanol) at 90°C. The Diels-Alder reversible chemistry equilibrium reaction is shown in Figure 1. During the synthesis of removable resin at 60°C, the reaction is driven towards the bonding of furan and imide groups in the resin molecule which allow it to behave like a conventional epoxy resin. Thus, when the removable epoxy resin in the foam is at normal temperatures (i.e., T < 60°C), the foam has the structure and properties similar to a conventional epoxy foam. However, at a temperature of 90°C, the driving force of the equilibrium reaction reverses such that the cycloaddition products revert back to the unreacted furan and imide functional groups. Therefore, when the foam is immersed in a mild solvent (i.e., n-butanol) at 90°C, the Diels-Alder bonds reverse so that the crosslinked epoxy structure breaks down and dissolves. Both blown and syntactic removable foam encapsulants have been developed. Foam removal experiments have shown that the foams are removed completely from components using this solvent immersion technique. Results of the removal of GMB-filled removable foam from electronic components are shown in Figure 2. The depotted units are fully functional and can be reworked and repotted as necessary. The removable foam technologies have been transferred to Honeywell, KCP for production applications.

Significance: The removable encapsulant technologies were developed for important Sandia/DOE projects requiring encapsulation. Existing systems had not been designed to be reworkable or repairable, thus, the units could not be easily repaired in the event of a system failure. Several electromechanical systems are being redesigned so that when a component requires repair or replacement, the modification can be done and then the unit can be returned to service. Removable encapsulants will facilitate the reworkability of these important redesigned electromechanical systems. Removable foams and adhesives will be used in developmental system units over the next several years and eventually will be used in actual system production.

Contact: Ed Russick, Organic Materials Dept., 1811
Phone: (505) 844-4357
Fax: (505) 844-9624
Email: emrussi@sandia.gov

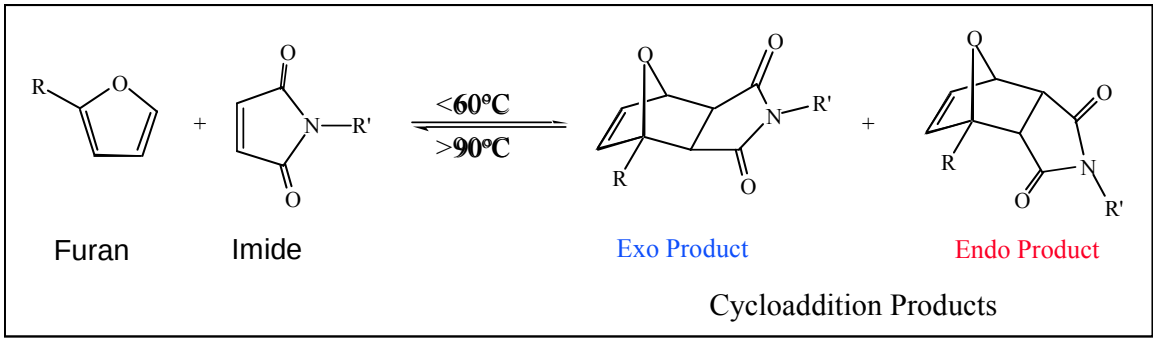

Figure 1. Diels-Alder Reversible Chemistry Equilibrium Reaction

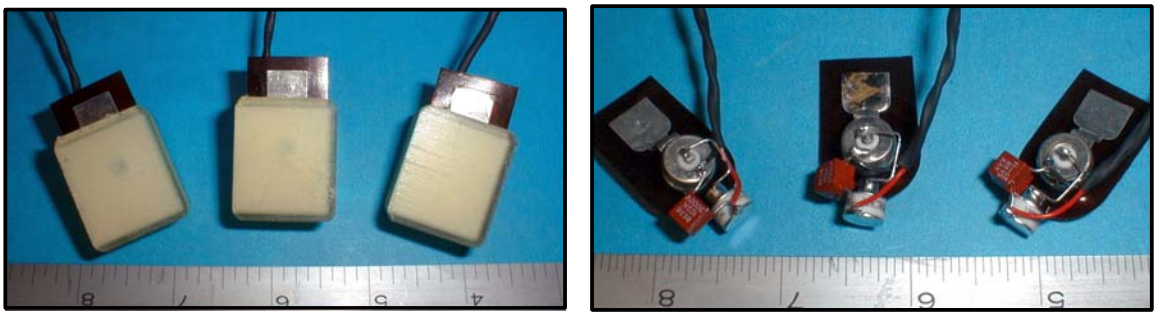

Figure 2. Components potted in removable foam (left), then depotted with 90°C n-butanol

Computational Modeling of Sintering

V. Tikare, M.V. Braginsky

Motivation: Sintering is a critical, possibly the most important, processing step during manufacturing of ceramics. The microstructural evolution, the macroscopic shrinkage, and shape distortions during sintering will control the engineering performance of the resulting ceramic component. Yet, modeling and prediction of sintering behavior is in its infancy, lagging far behind the other manufacturing models. We have developed a set of computational tools with a user-friendly, graphical interface that will enable scientists and engineers to simulate microstructural evolution and macroscopic dimensional changes during sintering. These tools are being applied to predict the microstructure of lead-zirconate-titanate (PZT) material in the power supply for the neutron generator.

Accomplishment: We have developed a kinetic, Monte Carlo model to simulate microstructural evolution during sintering. The mesoscale model can simulate microstructural evolution in a complex powder compact of hundreds or even thousands of particles of arbitrary shape and size by 1. curvature-driven grain growth, 2. pore migration and coalescence by surface diffusion, 3. vacancy formation, grain boundary diffusion and annihilation shown in Figure 1. This model has been validated by comparing predictions of the simulation to analytical predictions for simple geometries. The model can be used to obtain sintering stress and materials viscous moduli of powder compacts. These constitutive equations can be used by macroscopic simulations for simulating shrinkage and shape changes in FEM macroscale simulations. A user-friendly code that can simulate microstructural evolution during sintering in 2D and in 3D was developed. This code can run on most UNIX platforms and has a motif-based GUI. The microstructural evolution is shown as the code is running and many of the microstructural features, such as density, grain size, pore size, the average grain boundary length (in 2D) and area (in 3D), etc. are measured and recorded as a function of time.

Significance: Increasingly complex geometry, multi-material systems with very tight dimensional tolerances are required to advanced materials technologies for low temperature co-fire ceramics. Improved modeling is critical for advancing these complex ceramic technologies. However, the densification and sintering behavior in multi-material systems are poorly understood and difficult to control. Development of advanced modeling tools for simulating fabrication processes will greatly reduce the development cycle by minimizing/eliminating the repetitious, trial and error experiments and provide a predictive capability to aid the design and manufacturing processes. Consider sintering in a system of aligned, elongated particles where all thermodynamic quantities are isotropic except the shape. We found extremely variable behavior with the shrinkage anisotropy that was either in the direction of elongation or not depending on the details of particle packing as shown in Figure 2.

Contact: Veena Tikare, Materials & Process Modeling & Computation Dept., 1834
Phone: (505) 844-1306
Fax: (505) 844-9781
Email: vtikare@sandia.gov

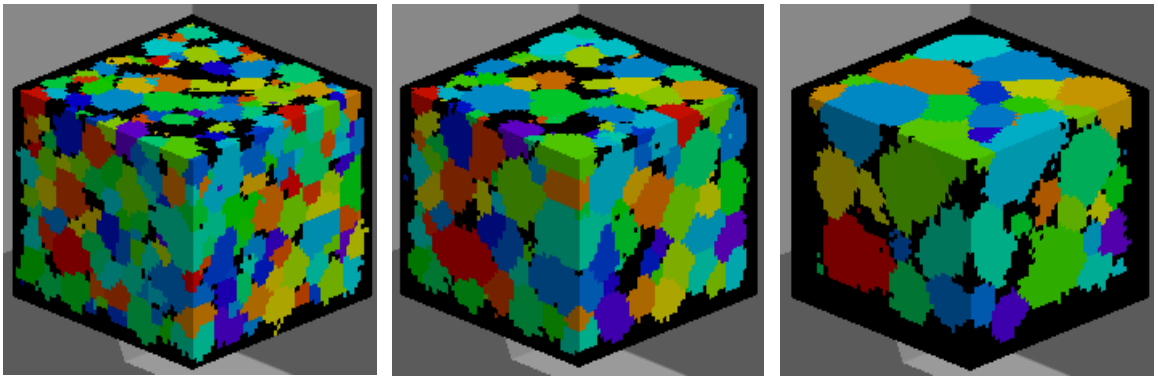

Figure 1. Three-dimensional simulation of microstructural evolution during sintering in a powder compact. The colored features are grains and the black features are pores. As sintering progresses, the compact shrinks due to densification and grains and pores coarsen.

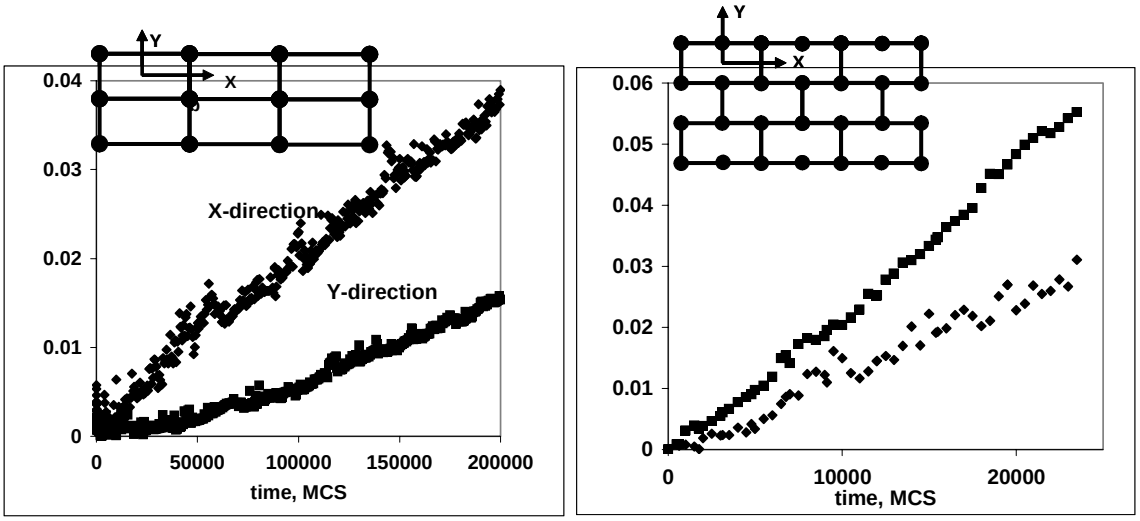

Figure 2. Shrinkage for aligned, elongated particles in two different geometries. While the particles are arranged very similarly, simple-packed and close-packed, the shrinkage behavior is very different. For simple packed particles, the shrinkage is predominantly in the direction of elongation (X-dir), but for close packed particles, it is in the direction perpendicular to elongation (Y-dir).

Low Temperature Cofire Ceramic (LTCC) Materials and Process Control

K.G. Ewsuk, C.B. DiAntonio, D.N. Bencoe

Motivation: Low temperature co-fire ceramic (LTCC) materials and processing technology provide a versatile and cost-effective means to manufacture advanced microelectronic packages (e.g., for RF wireless communications). Precise and reproducible sintering shrinkage are particularly critical in LTCC manufacturing. Sintering science and technology are being applied to improve materials and process control in LTCCs. Specifically, Master sintering curve (MSC) theory [1], has been evaluated as a tool to predict and control LTCC sintering. MSC theory isolates and relates the easily measured and controlled sintering parameters (time, t, and temperature, T) to sintered density. This generalization is possible, assuming that the microstructure-density trajectory during sintering is independent of thermal history. A unique master sintering curve is obtained for a given material processed in a given manner. Once obtained, the MSC can be used to predict and control final sintered density based solely on the time-temperature sintering profile. Additionally, the MSC also provides the ability to assess lot-to-lot materials consistency and green processing control and reproducibility prior to costly processing/firing.

Accomplishment: MSC theory was originally developed for materials that undergo isotropic densification by solid-state sintering. We have successfully extended MSC theory to a ceramic filled glass LTCC that undergoes anisotropic densification by viscous sintering [2]. Dilatometric sintering shrinkage experiments were designed and completed to characterize the anisotropic shrinkage of Dupont 951 Green Tape™, and subsequently to construct densification curves as a function of heating rate. These data were then used to determine the activation energy (317 kJ/mole) for densification that was used in conjunction with the experimental sintering time, temperature, and density data to construct a master sintering curve for the Dupont 951 LTCC system. Figure 1 shows that all of the experimentally determined, heating rate dependent densification data collapse onto to a single MSC. Calculations based on the MSC for the 951 LTCC system prove that MSC theory can be used to reliably predict sintered density as a function of arbitrary time-temperature excursions (Figure 2). Density-theta predictions for different time-temperature profiles map onto the MSC, even for multiple heating rates, soak times and temperatures (Figure 2)

Significance: We also demonstrated that different lots of the same material processed in the same manner exhibit the same sintering behavior (Figure 3). Different materials and/or processes will produce a different MSC (i.e., the sintering data will not fall on the baseline MSC). Consequently, the MSC has potential for use as a quality control tool to screen raw materials and process reproducibly before costly processing/firing.

The master curve concept also has been extended and adapted to binder decomposition. Master decomposition curves (MDCs) have been constructed for the DuPont 951 LTCC Green Tape™ that describes the degree of binder removal as a function of processing time and temperature. Together, MDCs and MSCs offer significant potential to better control and optimize the LTCC co-firing process.

[1] H. Su and D.L. Johnson, "Master Sintering Curve: A Practical Approach to Sintering," *J. Am. Ceram. Soc*., **79** [12] 3211-17 (1996).

[2] K.G. Ewsuk, C.B. DiAntonio, and D.N. Bencoe, "Characterization and Control of Low Temperature Co-fire Ceramic (LTCC) sintering," to be published in the Proceedings of Ceramic Interconnect Technology: The Next Generation, IMAPS, April 7-9, 2003, Denver, CO.

Contact: Kevin Ewsuk, Ceramic Materials Dept., 1843
Phone: (505) 272-7620
Fax: (505) 272-7304
Email: kgewsuk@sandia.gov

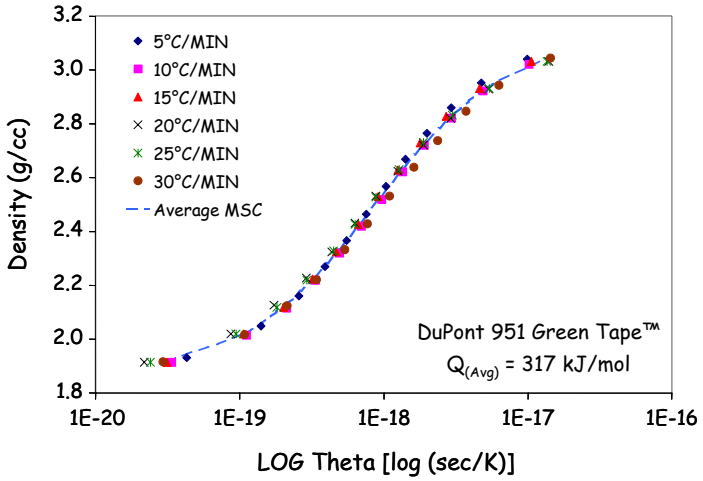

Figure 1. The master sintering curve (dashed line) for Dupont 951 LTCC Green Tape™ obtained using dilatometric density, time, and temperature data (symbols in the figure), and an experimentally determined activation energy for densification of 317 kJ/mol.

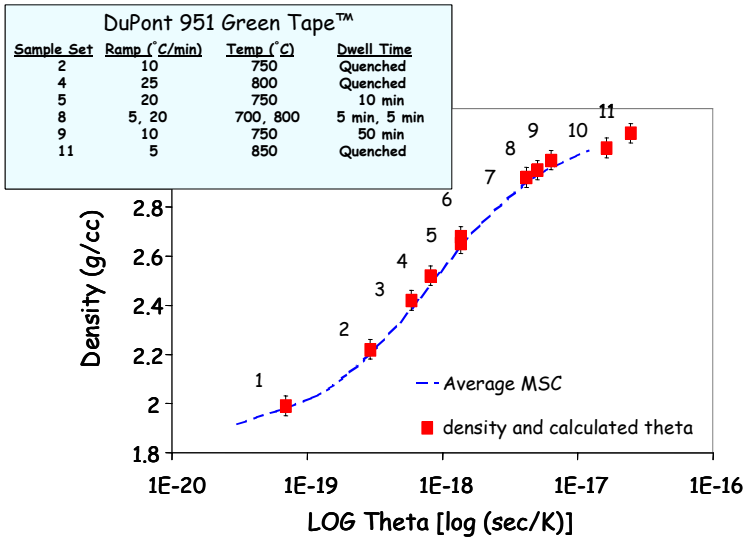

Figure 2. Density-theta values for 11 different time-temperature excursions mapped onto the MSC for Dupont 951 LTCC Green Tape™, demonstrating the ability to predict and control density during sintering

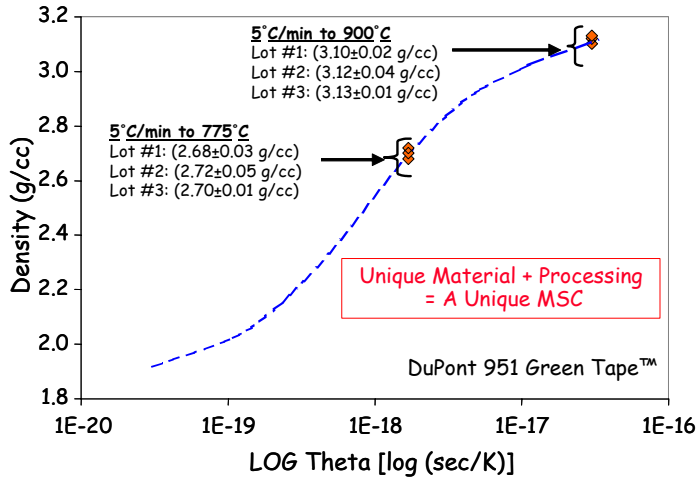

Figure 3. Density-theta values for three different lots of material processed using two different time-temperature excursions, and mapped onto the MSC for Dupont 951 LTCC Green Tape™, demonstrating lot-to-lot materials consistency.

Nuclear Magnetic Resonance (NMR) as a Tool for Characterizing Porous Ceramics and for Studying Ceramic Sintering

S. Monroe, C. Newton, J. Glass

Motivation: Differential densification during the sintering of ceramic powder compacts results in unacceptable shape deformation and microstructural inhomogeneities (e.g., cracks & porosity) that degrade functionality of the dense parts. Density gradients that lead to sintering problems on both the microscopic and macroscopic scales often develop during the powder compaction process. Both the ceramic powder compaction and sintering processes have been studied at Sandia National Labs using an approach in which we combine modeling, measurements, and materials characterization. One of the key ingredients of this program is the capability to non-destructively determine spatially resolved microstructural information about the porous ceramic body. Most conventional microstructural characterization techniques determine average properties of the ceramic compact or require that it be sectioned. We have developed Nuclear Magnetic Resonance (NMR) techniques that allow us to overcome the shortcomings of conventional techniques.

Accomplishment: We have combined both the Magnetic Resonance Imaging (MRI) and Relaxation measurement capabilities of NMR to characterize the porosity of ceramics during the early stages of sintering. Materials used in this study were a mesoporous SiO_2 glass, γ- and α-Al_2O_3 and ZnO powders, and partially sintered ceramics made from each of these powders (Fig. 1). The open porosity in the ceramic body was filled with NMR sensitive liquids or gases and the signal intensity and relaxation times were used as probes of the pore space. Gas phase imaging provides the means for non-destructively characterizing density and density gradients in ceramic compacts using the signal intensity of polarizable gases such as C_2F_6 and C_4F_8. It also allows spatially resolved measurements of pore size, surface area, and adsorption isotherms (Fig. 2). MR images obtained as a function of gas pressure, at constant temperature, form a pixel-by-pixel map of adsorption isotherms that compare very well to results obtained using conventional N_2 BET adsorption (Fig. 3). Conventional N_2 BET measurements are limited by the fact that they are bulk measurements, and are therefore capable of providing only the average properties for the material as a whole. Adsorption isotherms obtained for varying regions can only be acquired by physically sectioning the sample, a method that is both time-consuming and destructive. The advantage of the NMR adsorption isotherm measurements is that we are able to non-invasively and non-destructively obtain the spatially-resolved adsorption isotherms of gases in porous ceramics that contain open porosity. We can also obtain information about differences in surface chemistry in different regions of the same sample. While spatial resolution in MRI will never approach the scale of individual pores, it is able to provide statistical averages of the underlying pore structure parameters, resolved on a macroscopic scale.

Significance: We now have a non-destructive technique for obtaining spatially resolved microstructural information about porous ceramics including porosity, pore size, pore shape, surface area, pore connectivity, and surface chemistry. Several samples and several materials can be measured simultaneously. The information obtained from these experiments can be used for both understanding the compaction and sintering processes, for quality control, and for identifying and following the evolution of microstructural defects.

Contact: S. Jill Glass, Ceramic Materials Dept., 1843
Phone: (505) 845-8050
Fax: (505) 844-4816
Email: sjglass@sandia.gov

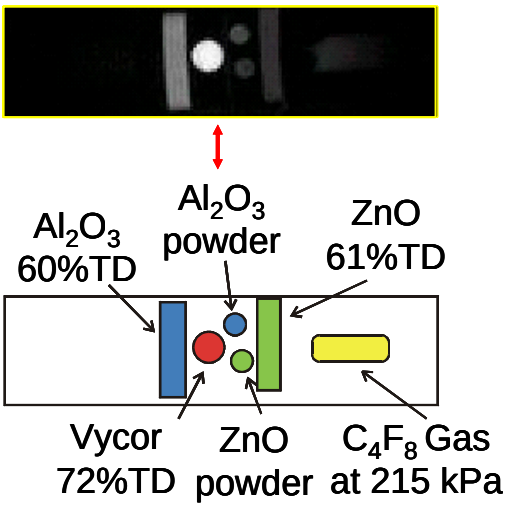

Figure 1. Gas phase magnetic resonance image (top) and schematic (bottom) of ceramic powders and samples used in NMR adsorption isotherm surface area measurements.

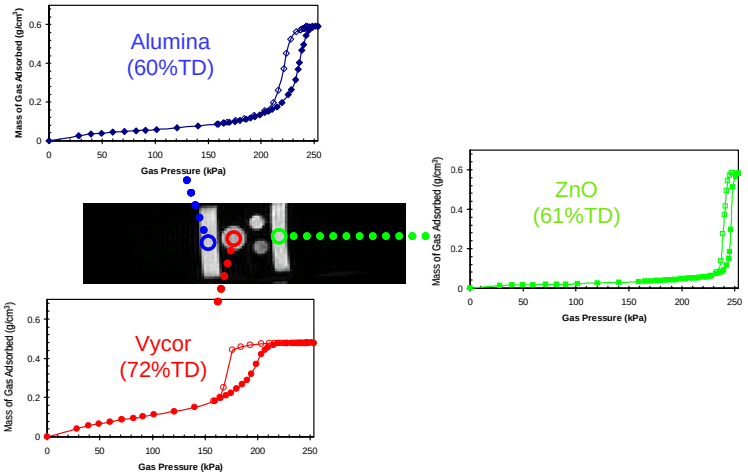

Figure 2. Space resolved adsorption isotherms for porous alumina, Vycor and zinc oxide. TD=theoretical density.

	N_2 BET Surface Area (m^2/g)	NMR BET Surface Area (m^2/g)	Hg Porosimetry Surface Area (m^2/g)
Al_2O_3 Powder	41	*42 ± 1*	
59% TD Al_2O_3	34	*35 ± 2*	37
69% TD Al_2O_3	5	*6*	7
ZnO Powder	19	*17 ± 2*	
62% TD ZnO Ceramic	7	*7.5 ± 0.6*	8.5
72% TD Vycor Glass	112	*118 ± 6*	

Figure 3. MRI space resolved surface areas agree very well with conventional nitrogen BET surface area measurements.

Sintering of Multi-Material Systems: Experiments to Support Modeling

T. J. Garino, D. J. Zschiesche

Motivation: A number of components for present or proposed future use in nuclear weapons systems consist of two or more different materials sintered together. When these materials, which may be ceramics, metals or cermets, sinter, they shrink by as much as 20% linearly. In a multi-material component, if the strain rates due to sintering of the various materials are not identical (which is nearly always true) stresses will develop in the materials. These stresses alter the shrinkage behavior of the materials and can produce defects such as cracks or delaminations. This work aims to develop a science-based understanding of the constrained sintering process so that sintering behavior can be predicted and controlled.

Accomplishment: Sandia's multi-material sintering program consists of developing a unique finite-element model to predict shrinkage, shape change and stress as well as an experimental program that supports the model development. The experimental program both provides the materials input parameters that are required by the model and also verifies the prediction of the model. The combination of an advanced model with specialized experimental characterization capabilities makes this program unique.

To be able to predict the sintering behavior of any multi-material system, a model must have accurate input data that describes the behavior of each of the materials during free sintering. The first type of data needed is the free sintering shrinkage behavior of the materials. This can be obtained with a conventional dilatometry or by using an in-situ direct-observation, non-contact technique that allows several small samples to be analyzed simultaneously at temperatures up to 1500°C in any desired atmosphere (see Figure 1a). Since this technique is non-contact, it is preferable to dilatometry for thick-film materials and viscous sintering (glass-containing) materials that might break of flow due to the load of the pushrod. This type of data can then be used to generate a master-sintering curve, which is another capability of Sandia's sintering program that can then predict the shrinkage behavior of a given material for any sintering schedule. Another parameter required is the uniaxial viscosity of the materials during sintering and this has been measured using a sinter forging apparatus where a cyclic load is applied to a sintering body during constant rate heating while measuring its shrinkage rate in the direction of the applied load (Figure 1b).

Two types of model multi-material geometries have been used to validate the predictions made by the FEM model using the experimentally determined input data, bi-layers and concentric cylinders. The shrinkage and curvature of the bi-layers was measured in situ using the same system mentioned above (see Figure 2). Several types of concentric cylinder samples where the inner and outer cylinder shrink at different rates due to differences in green density and/or average particle size (see Figure 3) were also fabricated and sintered.

Significance: The validated, experimentally-based FEM model will allow faster development of new components by eliminating the need for numerous trial-and-error experiments.

Contact: Terry Garino, Ceramic Materials Dept., 1843
Phone: (505) 845-8762
Fax: (505) 844-9781
Email: tjgarin@sandia.gov

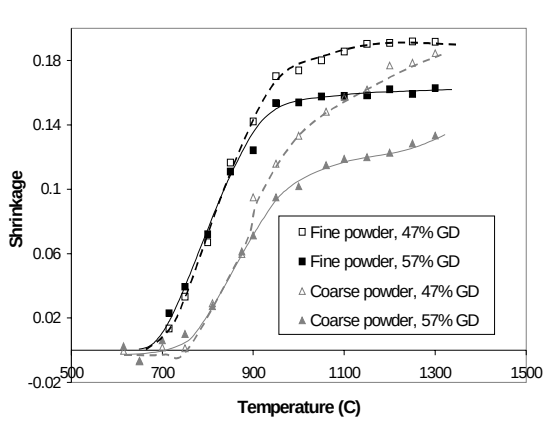

(a)

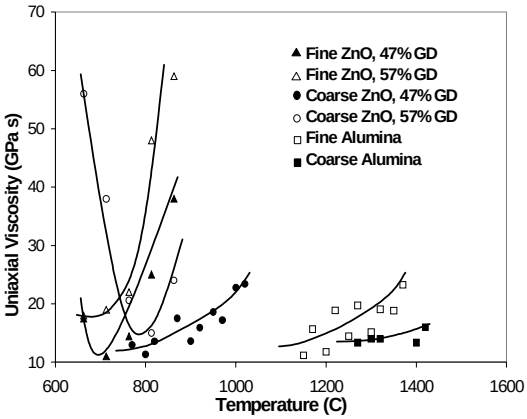

(b)

Figure 1. Input data for FEM multi-material sintering modeling: a.) free sintering shrinkage data for zinc oxide samples with differing green densities (GD) and average particle sizes, and b.) uniaxial viscosity data for various zinc oxide and alumina samples during sintering.

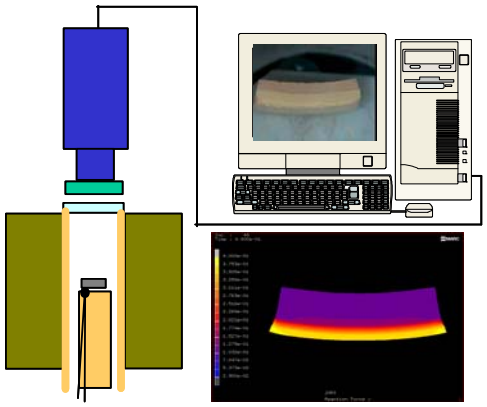

Figure 2. A schematic diagram of the video furnace apparatus for in-situ observation of sintering bilayers. The insert shows a FEM prediction for comparison.

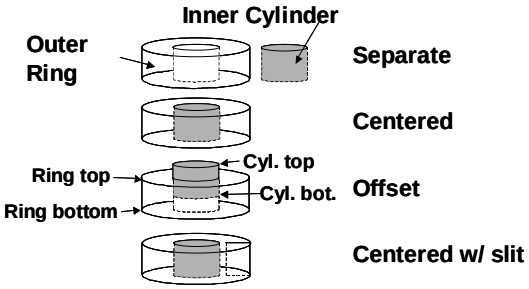

Figure 3. The four types of concentric cylinder samples used to validate multi-material sintering FEM predictions.

Ultra High Temperature Ceramics for Hypersonic Vehicle Applications

R. Loehman, B. Gauntt, D. Zschiesche, H. Dumm

Motivation: Thermal insulation materials for sharp leading edges on hypersonic vehicles must be stable at very high temperatures (2000°C), they must resist evaporation, erosion and oxidation, and they should exhibit low thermal diffusivity to limit heat transfer to support structures. Materials with those properties are required for development of hypersonics for prompt and precise delivery to difficult targets, a need that is highlighted in the Emerging Threats SBU business plan. The most promising materials for that application are the family of ultrahigh temperature ceramics (UHTCs), comprising ZrB_2 and HfB_2, and composites of those ceramics with SiC. Those ceramics are hard and have very high melting temperatures (3245°C for ZrB_2 and 3380°C for HfB_2), they are reported to form protective, oxidation resistant coatings, and to have low vapor pressures at potential use temperatures. However, in their present state of development UHTCs have exhibited poor strength and thermal shock behavior, a deficiency that has been attributed to inability to make them as fully dense ceramics with good microstructures.

Accomplishment: Our initial evaluation of UHTC specimens provided by the NASA Thermal Protection Branch suggested that their poor properties were due to agglomerates, inhomogeneities, and grain boundary impurities, all of which we believed could be traced to errors in ceramic processing. Those results suggested that UHTC properties could be improved by applying our fundamental understanding of ceramic processing to eliminate the defects that had so far limited UHTC properties.

Results in the first year have been extremely promising. We have made UHTCs in both the ZrB_2 and HfB_2 systems that are 100% dense or nearly so, and that have favorable microstructures, as indicated by electron microscopic examination. In addition, we have hot pressed UHTCs with a much wider range of SiC contents than anyone previously has been able to make, as shown in Figure 1. The microstructures of those UHTCs appear to be very uniform (Figure 2). We have started measuring thermal diffusivities so we can understand how UHTC thermal properties are determined by composition and microstructure (Figure 3).

Significance: UHTCs with better thermal and mechanical properties will enable the development of hypersonic vehicles for a variety of missions. Availability of thermal protection materials with a range of compositions and microstructures will give system engineers added flexibility in optimizing their designs.

Contact: Ron Loehman, Ceramic Materials Dept., 1843
Phone: (505) 272-7601
Fax: (505) 272-7304
Email: loehman@sandia.gov

Previous attempts required 20% SiC for full density

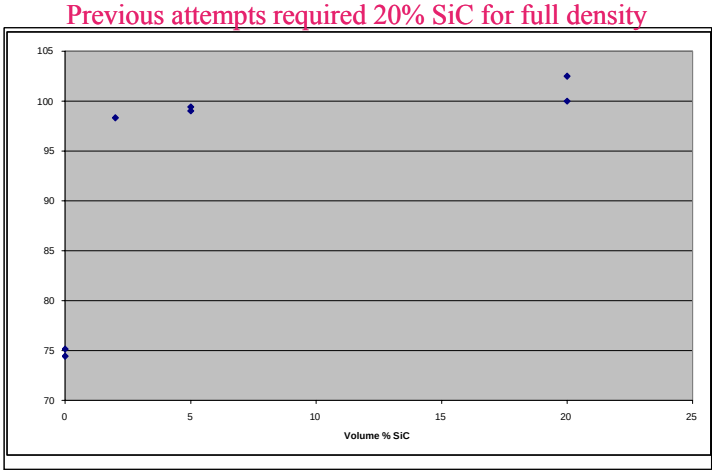

Figure 1. Variation of relative density of ZrB_2 – SiC and HfB_2 – SiC UHTCs as a function of SiC content.

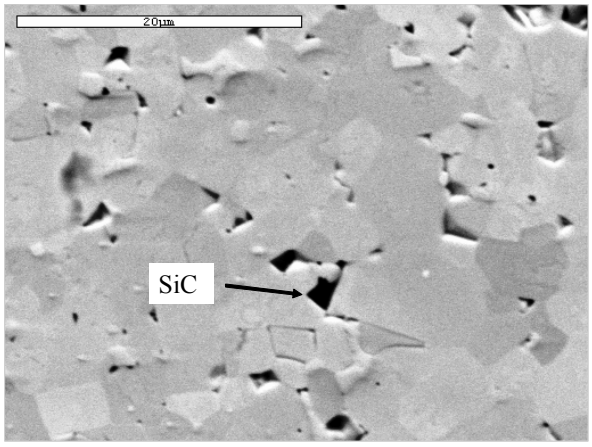

Cross section of sample interior

Figure 2. Microstructure of HfB_2 – 2% SiC UHTC showing uniform microstructure and absence of undesirable porosity

Thermal Diffusivity of HfB_2+20%SiC Composite

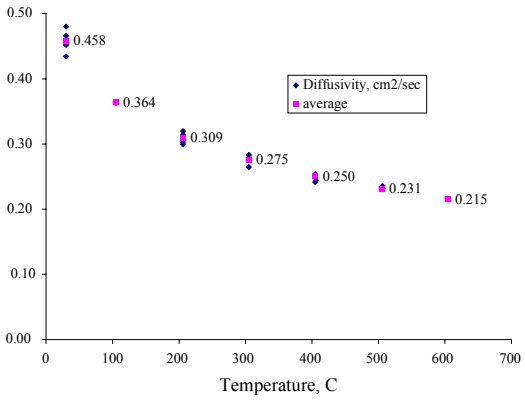

Figure 3. Variation of thermal diffusivity of ZrB_2 – 20% SiC UHTC as a function of temperature shows excellent reproducibility

Response Surfaces for a Powder Flame Spray Process

A. Hall, R. Neiser, D. Cook, A. Mayer, J. Cates, D. Beatty, T. Roemer, D. Urrea

Motivation: Traditionally arc plasma processes have been used to deposit ceramic coatings. The powder flame spray process is an oxy-fuel process making it an interesting alternative for preparing ceramic coatings. Oxy-fuel processing equipment is less expensive than arc-plasma thermal spray equipment and may apply lower heat loads to the part being coated.

The Sultzer-Metco 6P powder flame spray torch is designed to deliver a feedstock powder to the center of an oxy-acetylene flame. The oxy-acetylene flame melts and accelerates the powder particles (See Fig. 1). A coating is formed when the particles impact a surface and solidify. The temperature and velocity of individual particles at the time of impact directly affects the microstructure and properties of the coating. Thus, understanding the relationship between process inputs, like oxy-fuel ratio and standoff distance, relative to process outputs, like particle temperature and particle velocity, is key to using the process effectively.

Accomplishment: A response surface for the 6P torch was created by using designed experiments to map the particle temperature and particle velocity space available to the 6P torch (Fig. 2). Oxy-fuel ratio, total combustible gas flow, cooling air flow, and standoff distance were systematically varied while particle temperatures, particle velocities, and heat loads were measured. This data was fit to a series of parabolic models to create a response surface that shows the relationship between oxy-fuel ratio, total flow, standoff distance, and cooling air flow and particle temperature, particle velocity, and heat load. Deposition efficiency and coating microstructure measurements were also made at selected points within the larger experimental matrix (the extremes and the center point of the designed experiment). A custom alumina-titinate powder with a tightly controlled 25-micron mean particle size was sprayed during all experiments except the heat load measurements, which were made with the flame only.

Significance: The response surface created was used to identify control vectors for the 6P torch. It was found that oxy-fuel ratio and total flow are orthogonal control vectors for particle temperature and particle velocity (Fig. 3). Specifically, as oxy-fuel ratio are increased, average particle temperature decreases. This occurs because as oxy-fuel ratio increases, flame temperature decreases. As total combustible gas flow increases, average particle velocity increases. Intuitively this makes sense, since increased gas flow through the torch increases gas velocities in the flow stream. Standoff distance was found to affect particle temperature and particle velocity slightly. In addition, when an air cap that directs the cooling air strongly into the flame was used, particle temperatures were found to decrease and particle velocities were found to increase.

Calorimetry experiments showed that standoff distance and oxy-fuel ratio are the primary contributors to heat load. As standoff distance decreases heat load increases. Again, cooling air flow was found to affect heat load more strongly when the cooling air flow was directed into the flame. In all cases, increases in cooling air flow decreased heat load. This effect was significant. Deposition efficiency was found to increase as particle temperatures and velocities increased. Denser microstructures with increased interparticle bonding were also observed at operating conditions that produced higher particle temperatures and velocities.

Contact: Aaron Hall, Joining & Coating Dept., 1833
Phone: (505) 284-6964
Fax: (505) 844-6611
Email: achall@sandia.gov

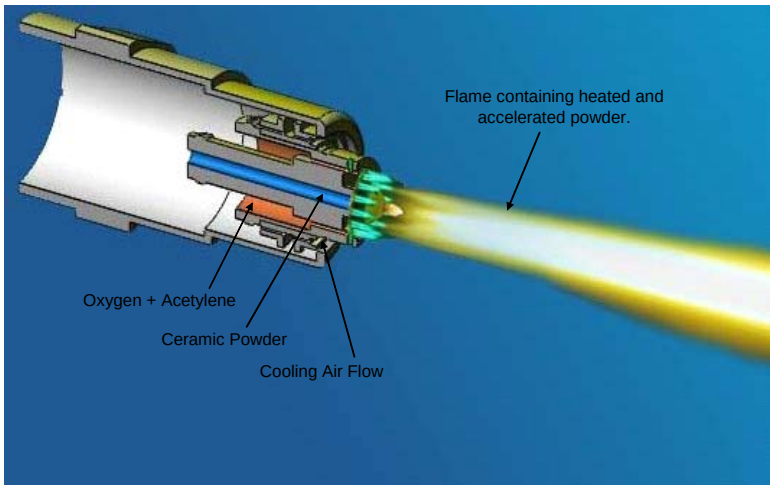

Figure 1. Schematic of the Sultzer-Metco 6P Powder Flame Spray Torch. Only the cooling air cap and nozzle are shown.

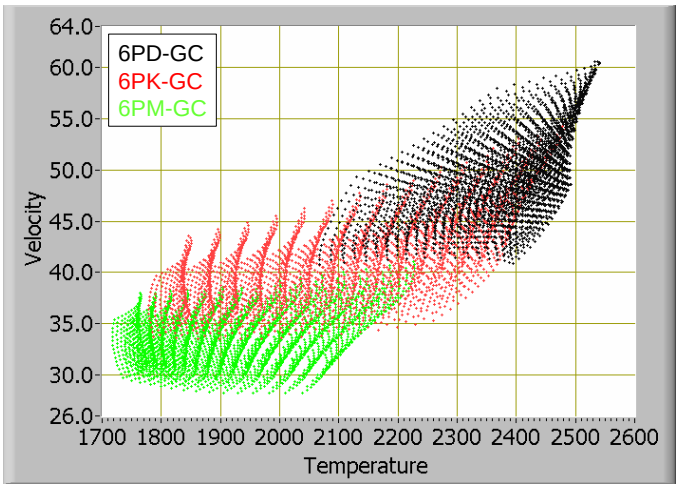

Figure 2. The particle temperature and particle velocity space available to the 6P torch with the "M", "K", and "D" nozzles using the gun cooling air cap.

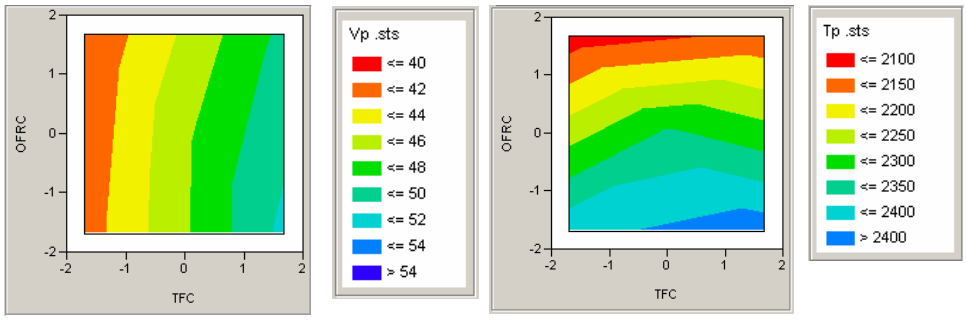

Figure 3. Two contour plots showing the orthogonal relationship between oxy-fuel ratio and total flow as control vectors for particle temperature (Tp) and particle velocity (Vp).

Improved Ceramic Joint Strength through Epitaxial Brazing Reactions

F. M. Hosking, J. J. Stephens, T. J. Headley, P. F. Hlava, F. G. Yost

Motivation: Metal-ceramic brazing is an enabling technology that is used to fabricate a wide variety of NW electromechanical devices. Applications range from high voltage tubes, thermal batteries, stronglinks, sensors, headers, connectors and feedthroughs or seals. The physical and mechanical metallurgy of the resulting braze joints are of particular interest in meeting critical product requirements. This can be accomplished through a multidisciplinary, science-based approach in understanding how the basic brazing reactions affect joint properties and performance. A systematic approach is being applied to the development and qualification of new active brazing alloys (ABA's) for use in metal/ceramic braze joints.

Accomplishment: The effects of wetting and interfacial reactions on the mechanical properties of brazed alumina ceramic were investigated. Two silver-based ABA binary systems were studied. Compositions were based on dilute active metal additions of Zr or Hf. Both additions readily reduce alumina at the brazing temperatures and form thermodynamically stable reaction products with the ceramic material and its glassy phase. The compositions were based on eutectic or near-eutectic Ag-2Zr and Ag-3.4Hf (wt. %) chemistries.

The primary research goal was to identify the fundamental mechanisms and reaction products that control active metal brazing on ceramic surfaces. The work included the development of experimental and analytical tools to correlate the different interfacial and bulk brazing reactions with hermetic and mechanical properties.

Test specimens were fabricated to characterize flow behavior, interfacial reactions, microstructure and strength of brazed single crystal sapphire and polycrystalline alumina ceramic. Crystallographic orientation effects were also examined on sapphire substrates.

Both alloys produced excellent wetting results. Microanalyses (SEM, EMPA, HRTEM, XRD) reveal a complex, multilayered reaction zone (Fig. 1). Similar reaction products are observed with either the Zr or Hf additions. The layer nearest the sapphire or alumina interface has a two-phase metal and oxide structure, with evidence of epitaxial growth of the zirconia or hafnia phase on the ceramic (Fig. 2). No epitaxy was observed for the Ag phase, although it does exhibit a single crystal structure. A continuous, columnar zirconia or hafnia layer lies next to the two-phase region. Precipitates of Zr or Hf also decorate the boundary between these two distinct reaction layers. Total thickness of the reaction product is approximately 2 μm. The remaining braze is primarily pure Ag.

Preliminary ASTM F19 tensile test data suggest that the epitaxial reaction at the ceramic interface and the compliant Ag braze structure yields consistently higher hermeticity and strength values. Tensile strength increases by almost 30% to 130 MPa for 94% alumina test pieces brazed with the Zr and Hf-containing ABA's as compared with the conventional ceramic metallization and brazing process.

This multidisciplinary research has been recognized through numerous professional invitations, awards and patents. It is a leading enabler of ABA science and technology.

Significance: Since brazing is used extensively in NW designs and production, understanding the basic brazing metallurgy is necessary to meet critical manufacturing and reliability requirements. Newer technologies, such as active metal brazing, also enable the development of improved product designs and processes.

Contact: F. Michael Hosking, Joining & Coating Dept., 1833
Phone: (505) 845-8401
Fax: (505) 844-4816
Email: fmhoski@sandia.gov

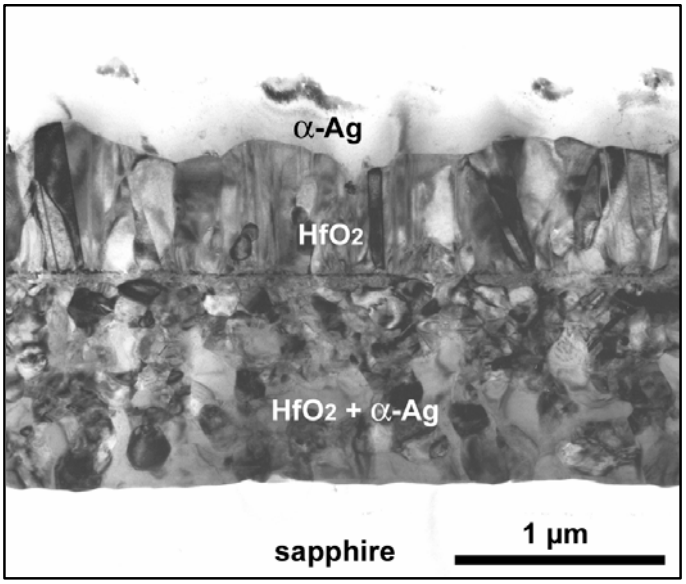

Figure 1. Multilayered reaction zone between Ag-3.4Hf ABA and single crystal sapphire.

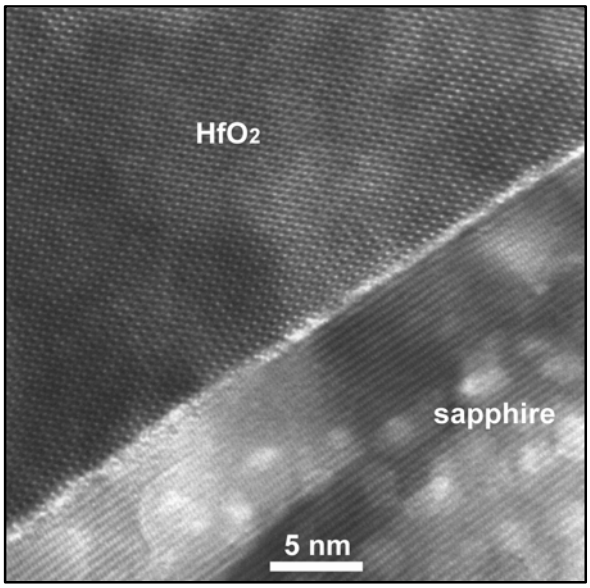

Figure 2. High resolution, transmission electron microscopy (HRTEM) image showing epitaxial orientation of hafnia lattice on basal plane sapphire.

New Developments in Low Melting Temperature, Pb-Free Solder Alloys

P. Vianco, J. Rejent, R. Grant, A. Kilgo

Motivation: Efforts are underway in the electronics industry to replace the traditional 63Sn-37Pb (wt.%) solder with alternative, Pb-free alloys. The candidate SnAgCu and SnAgBi alloys have significantly higher melting temperatures that pose processing and reliability concerns for printed wiring assembly (PWA) materials. Tin-based, Pb-free solders having melting temperatures equal to, or lower than, that of the 63Sn-37Pb (183°C) would allow designers to avoid costly laminate materials and molding compounds as well as provide a wider process window for the manufacture of Pb-free PWAs. A study was performed to develop a Sn-based, Pb-free solder having a low solidus temperature, a minimum pasty range and no low melting temperature phases. This study provided an opportunity to establish correlations between the microstructure and the physical and mechanical properties of highly complex, multicomponent alloy compositions.

Accomplishment: It was determined that low melting temperature alloys could be developed using the same empirical methodology that is the basis for developing high-performance, aerospace alloys. Those steps are: (1) Systematic elemental additions were made to a basis material –the binary 96.5Sn-3.5Ag eutectic composition (solidus = 221C). (2) Trends were established between the solder composition, critical properties and the microstructure. (3) Elemental additions were optimized for best engineering performance. Three ternary alloys were evolved from the binary alloy: 91.84Sn-3.33Ag-4.83Bi, 87.5Sn-7.5Au-5.0Bi, and 86.4Sn-5.1Ag-8.5Au having solidus temperatures of 212°C, 200°C, and 205°C as determined by Differential Scanning Calorimetry (DSC). The microstructure of the 87.5Sn-7.5Au-5.0Bi alloy (Fig. 1) included a solid solution 96Sn-4Bi matrix phase, particles of elemental Bi, and particles of Au-Sn intermetallic compound (IMC). Silver additions resulted in Ag-Sn intermetallic compound (IMC) particles. From the ternary alloys evolved the quaternary solder 86.8Sn-3.2Ag-5.0Bi-5.0Au having a solidus temperature of 194°C. Ring-and-plug shear tests determined that this solder had a shear strength nearly double that of the Sn-Pb and basis Sn-Ag solders, thereby confirming that the elemental additions provided both solid solution strengthening and precipitation hardening mechanisms. Couples were formed between the 86.8Sn-3.2Ag-5.0Bi-5.0Au solder and Cu that established interface IMC layer growth kinetics to be similar to those of the 63Sn-37Pb solder. The IMC layer composition included Cu-Sn and Cu-Au-Sn stoichiometries. Fifth and sixth order alloys were investigated, resulting in the composition 66Sn-5.0Ag-10.0Bi-5.0Au-10.0In-4.0Cu having a solidus temperature of 178°C that was 5 °C *less than* that of 63Sn-37Pb solder. The microstructure (Fig. 2) consisted of a 88Sn-6.5Bi-5.5In solid solution matrix and uniform distributions of several small particle phases. The lowest solidus temperature of 159°C was realized with the 62Sn-5.0Ag-10Bi-4.0Au-10In-4.0Cu-5.0Ga alloy. The solidus temperatures of all of these alloys could be predicted from the matrix phase composition when the latter was considered an ideal solid solution.

Significance: Tin-based, Pb-free solders were developed with solidus temperatures equal to, or less than, that of the traditional 63Sn-37Pb solder. Important correlations were identified between elemental additions, phases present in the microstructure, as well as alloy physical and mechanical properties. Engineering feasibility of the 66Sn-5.0Ag-10.0Bi-5.0Au-10.0In-4.0Cu solder was demonstrated with prototype PWAs.

Contact: Paul Vianco, Joining& Coating Dept., 1833
Phone: (505) 844-3429
Fax: (505) 844-4816
Email: ptvianc@sandia.gov

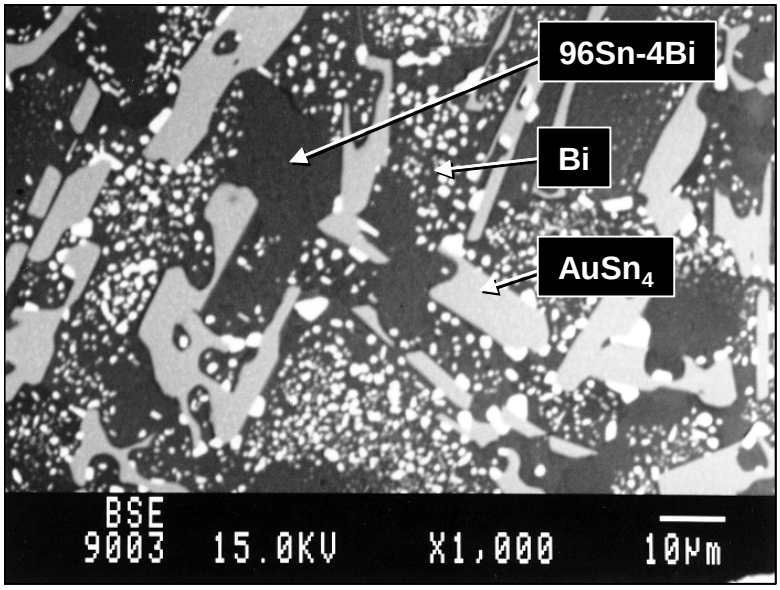

Figure 1. SEM photograph showing the microstructure of the 87.5Sn-7.5Au-5.0Bi solder ($T_{solidus}$ = 200°C).

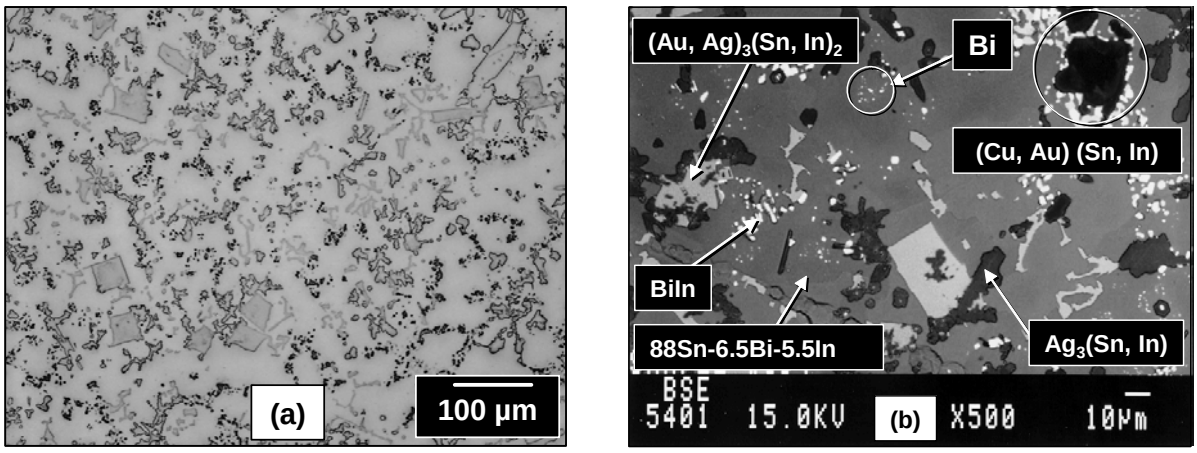

Figure 2. (a) Optical micrograph and (b) SEM/BSE photograph that identifies the phases present in the 66Sn-5Ag-10Bi-5Au-10In-4Cu solder ($T_{solidus}$ = 178°C).

Photonic Package Alignment with Asynchronous Laser Spot Welds

P.W. Fuerschbach

Motivation: Fiber optic packages are typically aligned with a laser that delivers 2 or 3 equal energy beams to the package synchronously through the use of separate optical fibers. By positioning identical focused laser beams at equidistant positions around the package and through synchronous pulsing of each fiber, multiple welds are made simultaneously. In practice, shrinkage strains from each weld are not always cancelled out via the synchronous weld approach and fiber alignment prior to welding is not maintained. Subsequent discrete alignment welds are often required to optimize fiber transmission employing a knowledge system to select the ideal position for the next weld. Active alignment using laser welding to rigidly attach diode lasers to fibers while simultaneously maximizing coupling is a very compelling approach since it completes two important assembly tasks in one step. The employment of a single fiber welding laser for asynchronous spot welding has potential as a one-step method for active alignment.

Accomplishment: CCD camera images were recorded before and after spot welding using actual fiber containing ferrules which were welded to a radially aligned TO style package. The fiber was coupled to a HeNe laser to illuminate the 62.5 mm fiber tip. Substantial movement of fiber tip after welding is apparent in Fig.1. Measurements of the fiber tip movement after each spot weld were used to investigate process variables. For the three replicate welds shown in Fig. 2, the magnitude of post weld shift does not appear to be affected by the number of prior tack welds or their sequence. Indeed, post weld shift from the first weld is virtually the same as post weld shift from the fourth weld. These results indicate that post weld shift is consistent and can be predicted at any location even after several other welds have been made. It was also found that some degree of axial restraint on the ferrule is crucial to achieve consistency in post weld shift magnitude, but that increasing the level of restraint beyond a certain minimum level does not appear to decrease post weld shift. It can also be observed in Fig. 2, that post weld shift direction is relatively consistent and predictable when welds have a minimum degree of restraint.

Significance: Since post weld shift magnitude and direction is generally consistent and predictable for asynchronous laser pulses, these results indicate that active alignment can be employed in the same manner it is employed using two or more synchronous pulses. If the post weld shift is the same for each weld, then welds that are made sequentially should have the same resultant post weld shift as welds that are made in the conventional manner. Since only one spot welding beam is used with the asynchronous approach, the cost and complexity of the multiple fiber and weld head systems is avoided. Precision may also be improved with asynchronous spot welds since it is easier to maintain and characterize one laser head than three.

Contact: Phil Fuerschbach, Joining & Coating Dept., 1833
Phone: (505) 845-8877
Fax: (505) 845-9659
Email: pwfuers@sandia.gov

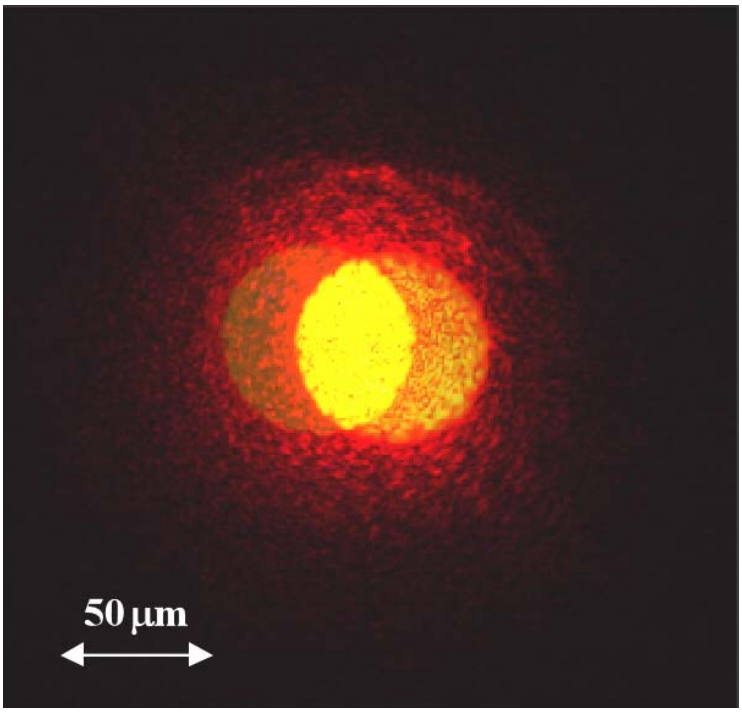

Figure 1. CCD camera image of significant fiber tip movement before and after laser spot welding. Horizontal post weld shift = 22.5 mm, vertical = 2.5 mm.

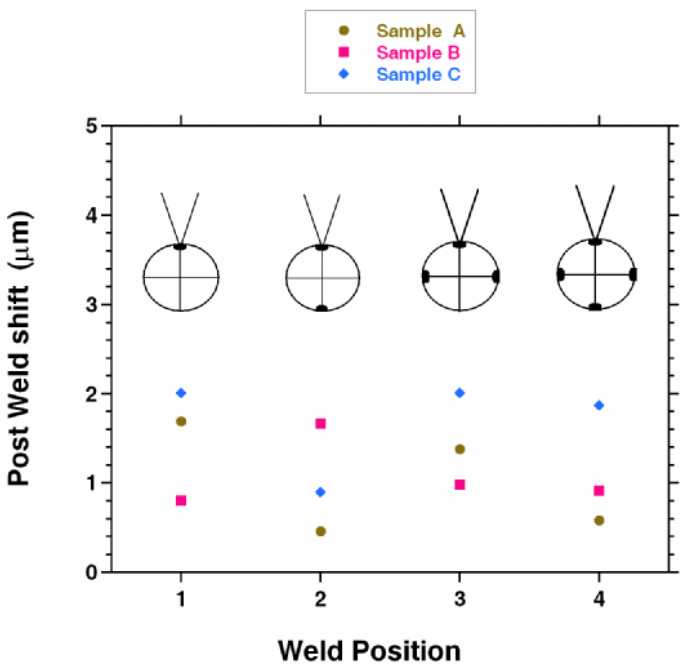

Figure 2. Effect of weld position and location of prior spot welds on resultant post weld shift magnitude. 1.7 J, 2.0 ms laser pulse, 1.0 kN axial restraint load.

Precursor Film Controlled Wetting of Pb on Cu

E. B. Webb III

Motivation: Sandia's mission to engineer nanometer scale devices motivates a need to understand atomic mechanisms by which materials form. To benefit from processes like self-assembly, one must control the forces driving the phenomenon. A fundamental concept to this is atomic transport and how transport mechanisms respond to perturbations. Surface transport is particularly relevant and, while experiments prove quite powerful for elucidating transport mechanisms for solids, liquid transport mechanisms are more elusive due to rapid transport rates. Knowledge of how surface transport mechanisms differ based on perturbations such as substrate crystal orientation will help enable the control of fluid transport on surfaces at the nanometer scale. A system that illustrates complex surface transport phenomena, including self-assembly, is Pb on Cu. Below the melting point of Pb (T_M^{Pb}), this system has been well characterized experimentally. Above T_M^{Pb}, the situation is less clear. Pb(l) is immiscible with Cu and drops on the surface equilibrate to a finite contact angle with an atomically thick Pb film covering the Cu surface between partially wetting drops. Experimental studies of the film are limited so details of film formation and structure are missing; however, this problem is well suited to atomic modeling.

Accomplishment: Molecular dynamics (MD) simulations resolve atomic trajectories, permitting direct calculation of transport properties. Pb(l) drops spreading on Cu(100) and Cu(111) were simulated with MD at T=700K. As illustrated in Fig. 1, the subtle difference of substrate crystal orientation gives dramatically different surface transport mechanisms. On Cu(111), a precursor film (or foot) of atomic thickness quickly emerges and advances ahead of the drop (Fig. 1a) whereas this is not obvious on Cu(100) (Fig. 1b). Not until much later time does a foot emerge from the drop and advance to cover the Cu(100) surface (Fig. 1c). As seen in experiments, Pb(l) drops on both Cu(100) and Cu(111) equilibrate to a finite contact angle in the model while an atomically thick film covers the rest of the Cu surface. Drops spread much more rapidly on Cu(111) than on Cu(100). Indeed, transport coefficients for Pb on Cu(111) are roughly an order of magnitude larger than on Cu(100).

Examination of the solid/liquid interface as well as atomic trajectories during the simulation reveals the cause of this dramatic difference in transport. On Cu(100), surface transport is controlled by the formation kinetics of the precursor foot. This is much slower on Cu(100) than on Cu(111) due to differences in the interaction of Pb adatoms with each surface. On Cu(100), Pb atoms exchange with Cu atoms in the surface crystal plane. Cu atoms that exchange occupy sites in the pre-wetting film. Thus, the formation of a surface alloy is partly responsible for reduced spreading kinetics for Pb on Cu(100) compared to Cu(111), where surface alloying is not observed. Simulations of droplet spreading were repeated on the substrates but with the precursor film already deposited, modeling Pb deposition in advance of droplet contact. For these simulations, very similar kinetics were observed for Pb(l) on Cu(100) and Cu(111) since the precursor film formation, and transport differences due to it, were removed.

Significance: A straightforward way to alter surface transport kinetics has been shown. Further simulations can reveal effects of surface patterning and stress to compliment our understanding of driving forces for fluid transport on surfaces.

Contact: Ed Webb III, Materials & Process Computation & Modeling Dept., 1834
Phone: (505) 284-6517
Fax: (505) 844-9781
Email: ebwebb@sandia.gov

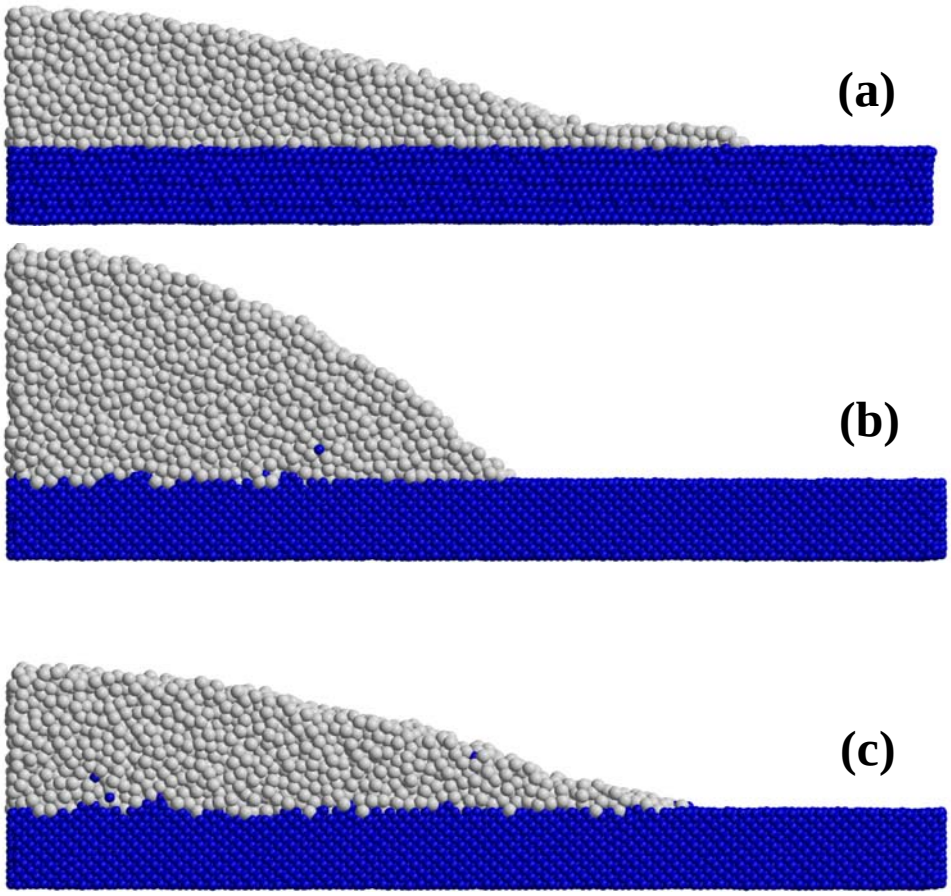

Figure 1. Snapshots from the simulations. Images are shown for Pb(l) on (a) Cu(111) and (b) Cu(100) after 0.5 ns of simulation trajectory. Pb(l) on Cu(100) after 3.6 ns is also shown (c). Larger, white atoms are Pb; smaller, blue atoms are Cu. A cross-section of the simulation cell is illustrated in each case to exhibit the drop/substrate interface more clearly. Given the symmetry of the system, only one half of the slice is shown.

Sealing of Solid Oxide Fuel Cells

R. Loehman, K. Ewsuk, D. Zschiesche, B. Gauntt

Motivation: Development of reliable methods for sealing solid oxide fuel cell (SOFC) stacks presents the most challenging set of performance criteria in the entire field of ceramic joining. For SOFC applications the requirements on the sealing method include:

1. adhesion of the sealing material to fuel cell components from RT to as high as 1000°C
2. need to provide a leak tight seal at the SOFC operating temperature
3. ability to maintain a seal while accommodating strains from SOFC components with different coefficients of thermal expansion (CTEs)
4. lack of adverse reaction between the sealing material(s) and the fuel cell components
5. chemical and physical stability of the sealant at temperatures up to 1000°C in oxidizing and reducing atmospheres
6. thermal shock tolerance
7. electrically insulating for some SOFC designs

All of the above properties must be maintained for SOFC operating lifetimes of up to 10,000 hours. No matter what the SOFC design, the seal must be adherent and leak tight. On the other hand, some stack designs may require joining only similar materials and thus, a matched CTE seal may be sufficient. The requirements may be contradictory. For example, being leak tight and adherent at high temperatures suggests a refractory, stiff sealant, which may work against the requirement for thermal strain accommodation. Such situations are common and seal developers know that seal design is specific to a particular component geometry and usually requires compromises among competing requirements.

Accomplishment: The essence of our approach is to engineer ceramic-filled glass composites, metal filled glass composites, and/or ceramic-filled metal composites that can be sufficiently fluid at temperature to relieve thermal mismatch stresses while still being rigid enough to maintain the seal. Relief of CTE mismatch stresses in these SOFC seals is achieved by either a ductile metal or a high viscosity glass that can yield through viscous creep. Properties of such composites can be varied over wide ranges by controlling the compositions, amounts, and microstructures of the different phases. In our experiments we have been able to control the flow properties of glass- ceramic powder composites by varying the glass transition temperature (Tg) of the glass and the glass: ceramic powder ratio. Figure 1 shows a composite made from a glass with a Tg of 623°C after being subjected to a representative fuel cell thermal cycle. With no added ceramic the glass flows completely over the Zr02 substrate, whereas with increasing amounts of filler the composite changes from moderate deformation at temperature to none at all. Figure 2 shows the results of experiments with the same glass: ceramic ratio and thermal cycle, but with a glass with a lower Tg (576°C). In this case all three compositions showed some flow at temperature, but it was less, the higher the ceramic filler content. In all cases the composites bonded strongly to the ceramic substrate, which was a piece of a SOFC electrolyte.

Significance: We have demonstrated compositions that bond to SOFC components and that have flow and deformation properties that can be controlled to minimize deleterious thermal stresses. This may allow SOFC developers to overcome a critical barrier to commercialization.

Contact: Ron Loehman, Ceramic Materials Dept., 1843
Phone: (505) 272-7601
Fax: (505) 272-7304
Email: loehman@sandia.gov

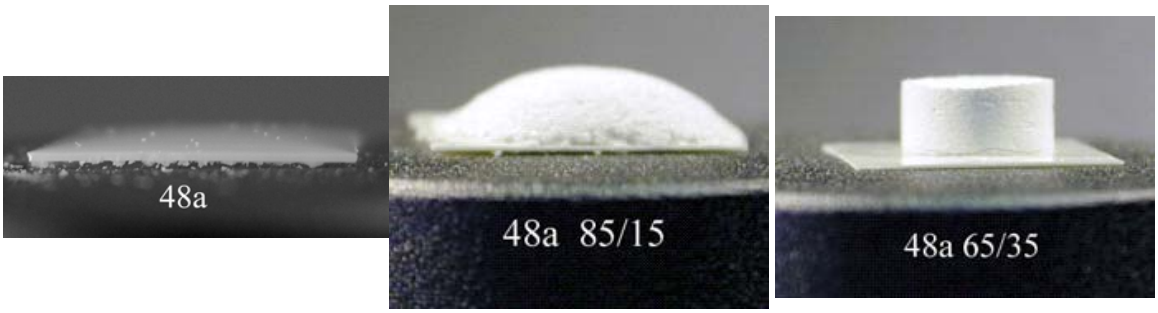

Glass on YSZ	85 vol% Glass/15%YSZ Powder	65 vol% Glass/35% YSZ Powder

Thermal Cycle: 10°/min to 1100°C, hold 12 min., cool to 850°C, hold 60 min.

Glass Properties: CTE = 6.1 x 10^{-6}/°C, Tg = 623°C

Figure 1. Heating experiments show the effect of glass/ceramic powder ratio on composite viscosity

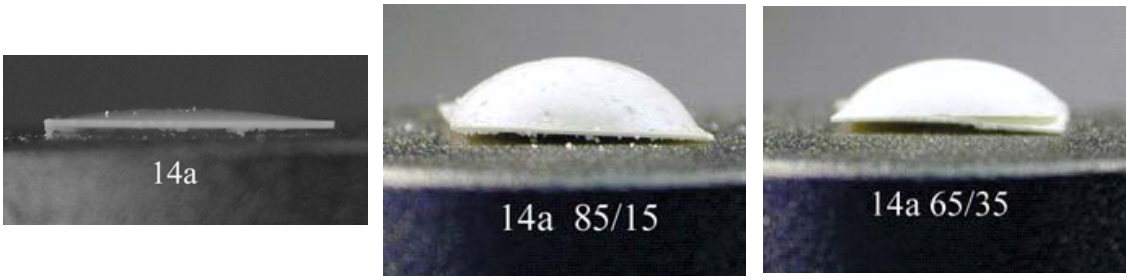

Glass on YSZ	85 vol% Glass/15%YSZ Powder	65 vol% Glass/35% YSZ Powder

Thermal Cycle: 10°/min to 1100°C, hold 12 min., cool to 850°C, hold 60 min.

Glass Properties: CTE = 9.1 x 10^{-6}/°C, Tg = 576°C

Figure 2. Heating experiments show the interplay of glass Tg and ceramic powder content on composite viscosity. Here a lower Tg produces a more deformable composite for the same thermal cycle as in Figure 1.

First Principles Model for Nucleation during Recrystallization

E. A. Holm

Motivation: In a variety of materials phenomena, nucleation events govern the final microstructure. For recrystallization, nuclei appear to originate from discontinuous growth events within the pre-existing subgrain structure. In this study, we develop a nucleation model based on the frequency of these events and apply this model to recrystallization in deformed aluminum microstructures. The result is the first recrystallization model based on fundamental physics and phenomenology.

Accomplishment: During or after plastic deformation, dislocations may organize into compact structures such as cell walls in a process termed recovery. If sufficient stored energy remains, the material may recrystallize by nucleating and propagating dislocation-free grains. How a recovered dislocation structure gives rise to growing, strain-free grains has been debated for several decades.

In this project, we explored the feasibility of nucleation of strain-free grains from a recovered subgrain structure. Using a Monte Carlo algorithm, we built subgrain structures that possess the same topology, texture, and boundary character observed in experiments. We assigned these structures appropriate boundary energies and mobilities and performed subgrain evolution simulations. In these realistic systems, we observe abnormal or discontinuous growth events rarely but repeatably, as shown in Figure 1(a). Since these events cause certain subgrains to exceed the critical radius for a recrystallization nucleus, we propose that discontinuous subgrain growth is the mechanism for nucleation in recrystallization.

In contrast with previous theories, which suggest that boundary energy anisotropy, second phase particles, or internal interfaces are necessary to nucleate recrystallization, our parametric simulations indicate that the presence of very high mobility subgrain boundaries are both necessary and sufficient to cause discontinuous subgrain growth. Therefore, we derive the frequency of discontinuous events to be proportional to the number of high mobility boundaries in the system, in excellent agreement with simulation results, as shown in Figure 1(b).

Using subgrain data accumulated for aluminum, we transform the discontinuous subgrain growth frequency to a nucleation density that is a function only of von Mises strain. Predicting more nucleation in high strain regions, such as near particles or shear bands, this model is consistent with experimental observations. Using this nucleation model, mesoscale recrystallization simulations of uniformly deformed materials yield microstructures that are realistic in scale and morphology, as shown in Figure 2. Furthermore, when this model is applied to more realistic deformed structures, it reveals structural and statistical differences due to nonuniform deformation, as in Figure 3.

Significance: This study is the first to show the plausibility for real materials of the 50-year-old abnormal subgrain growth hypothesis for recrystallization nucleation. Further, we derived physically based, quantitative models for nucleation frequency as a function of processing parameters and applied them in a recrystallization process model. This new, first-principles model for recrystallization elucidates a fundamental response of deformed metals.

Contact: Liz Holm, Materials & Process Modeling & Computation Dept., 1834
Phone: (505) 844-7669
Fax: (505) 844-9781
Email: eaholm@sandia.gov

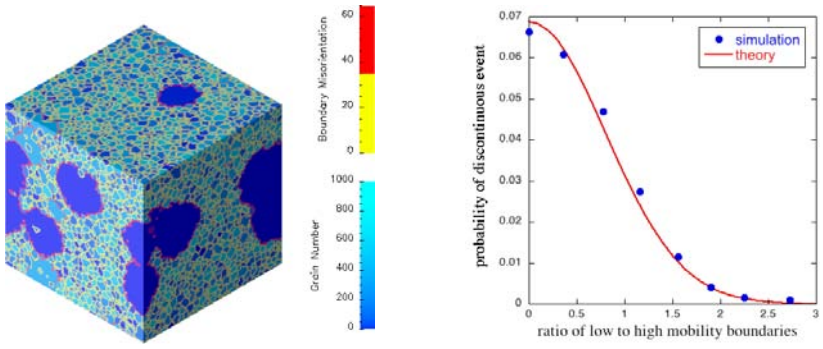

(a) (b)

Figure 1. (a) In simulations of realistic subgrain structures, a few subgrains (dark blue) grow discontinuously at the expense of the others. These subgrains invariably possess high mobility boundaries (red). (b) The probability of such discontinuous events varies with the number of high mobility boundaries in the system as predicted by theory.

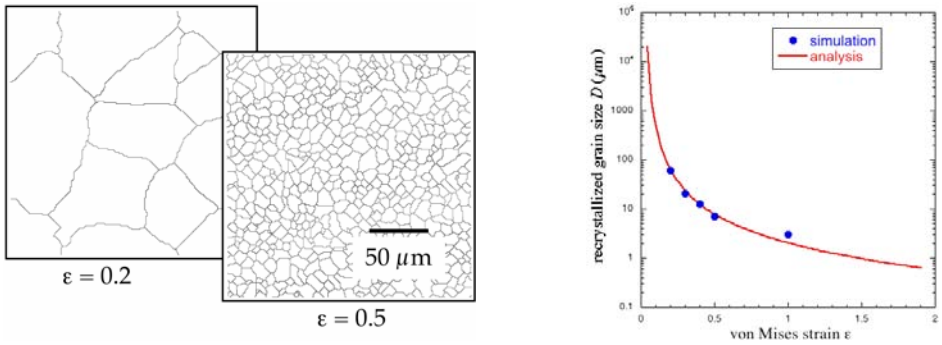

(a) (b)

Figure 2. (a) Using a nucleation model based on discontinuous subgrain growth, recrystallization simulations of uniformly deformed systems give realistic results, with recrystallized grain size decreasing as von Mises strain □ increases. (b) Recrystallized grain size agrees well with an analysis that assumes each nucleus contributes one grain to the recrystallized microstructure.

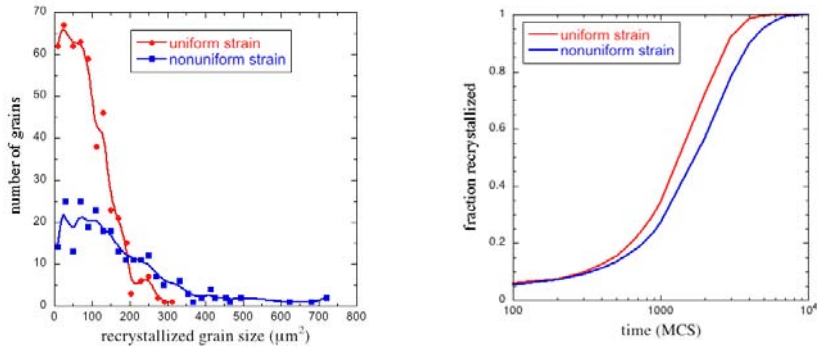

(a) (b)

Figure 3. Recrystallization simulations of nonuniformly deformed systems yield (a) a larger final grain size and (b) slower recrystallization kinetics than in uniformly deformed systems.

Atomistic Simulations of Solidification Processes

J. J. Hoyt

Motivation: A number of components critical to the Sandia mission involve the process of metal joining, either soldering, brazing or welding. Therefore it is of interest to develop a modeling capability that can realistically capture the key features of alloy solidification. Modeling of the complex morphologies that arise during solidification is a formidable challenge. A major obstacle is the fact that the final microstructure depends critically on several materials parameters which are difficult, if not impossible, to measure experimentally. The goal of the present research is to utilize atomistic simulations to compute these key quantities.

Accomplishment: Three materials parameters are required to perform a continuum level (phase field) simulation of solidification: the liquid state diffusion coefficient, the solid-liquid interfacial free energy, and a kinetic coefficient which relates the velocity of a planar interface to the undercooling. Furthermore, it is well known that the shape and velocity of the growing dendrite depends critically on the small anisotropy of the latter two quantities. To date, we have had considerable success in computing all three parameters through molecular dynamics (MD) simulations.

As an example, consider the kinetic coefficient (μ) or, equivalently, the rate of crystallization as a function of undercooling. We have developed three MD methods for extracting μ. A free solidification technique tracks the position of the solid-liquid boundary vs. time for systems maintained at a temperature below the equilibrium melting point, an imposed pressure method uses an applied pressure to drive the solidification process and a fluctuation scheme measures the decay rate of equilibrium interface fluctuations for systems held at the melting point. Fig. 1 shows the interface velocity vs. undercooling for pure Ni using all three techniques. Within numerical uncertainty the three methods are in agreement.

Despite the technological and scientific importance of solidification, an accurate theory for the rate of crystallization has not been established. In 1991 Mikheev and Chernov (MC) formulated a model of crystal growth based on ideas from density functional theory. Unlike earlier treatments, the MC description involves no adjustable parameters and explicitly accounts for the dependence of μ on the crystallographic growth direction. Fig. 2 shows a comparison of μ obtained from several MD simulations vs. the predictions of the model. The good agreement shown in Fig. 2 confirms for the first time the validity of the MC model of crystal growth in simple metal systems.

Significance: The ability to accurately predict various thermodynamic and kinetic properties of solid-liquid interfaces means that realistic continuum level modeling of solidification is now possible in several important alloy systems. It is hoped that modeling of dendritic microstructures will lead to important insights into the processes of soldering, welding and brazing.

Contact: Jeff Hoyt, Materials & Process Modeling & Computation Dept., 1834
Phone: (505) 284-5391
Fax: (505) 844-9781
Email: jjhoyt@sandia.gov

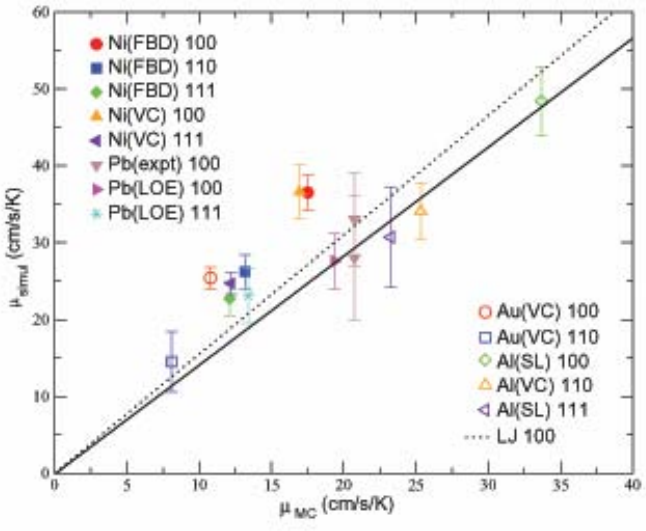

Figure 1. Solid-liquid interface velocities vs. undercooling for pure Ni obtained from three separate MD simulation techniques. Pure Ni was modeled using the embedded atom method (EAM). Negative velocities and undercoolings indicate melting.

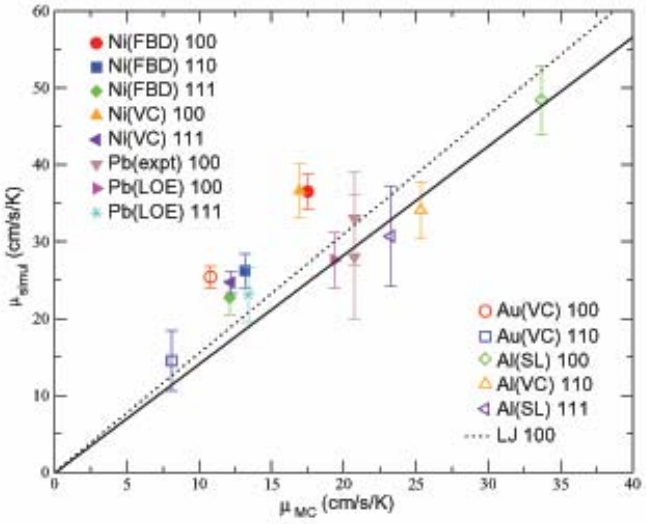

Figure 2. The kinetic coefficient obtained from MD simulation vs. that predicted by the theory of Mikheev-Chernov. Results for several EAM metals as well as the Lennard-Jones (LJ) system are plotted.

The μ-Molding of Ceramic, Metallic and Magnetic Materials

T. J. Garino, D. J. Zschiesche

Motivation: Components for μ-systems are currently produced by either silicon μ-machining techniques or by the LIGA process. Silicon μ-machining, although ideal for many applications, can only produce microstructures a few □m thick and is limited to silicon and a few other materials. The LIGA process can fabricate high-aspect ratio thick parts out of metals that can be electroplated but requires expensive x-ray lithography, is slow and cannot produce ceramics and more complex metals such as rare-earth transition-metal magnets (NdFeB) or stainless steels. Therefore, μ-molding has been developed to complement these techniques for certain applications.

Accomplishment: In the LIGA process, a poly-methyl methacrylate (PMMA) mold is created using an x-ray mask and collimated, high intensity x-rays from a synchrotron. Molds with cavities up to several mm deep with straight sidewalls and a resolution of several μm can be made after exposure and development of the PMMA. The μ-molding process involves filling the cavities in such a mold with a powder/polymeric binder mixture instead of the standard process of electroplating. The individual parts can then be removed from the mold by dissolution of the PMMA in a solvent. In the simplest form, the μ-parts can then be used as-is, as in the case of the epoxy-bonded NdFeB permanent magnets for μ-motors shown in Figure 1.

For applications where dense ceramic and metal parts are desired, the demolded binder-containing parts can be thermally treated to first pyrolize the binder and then to higher temperature to sinter the ceramic or metal particles to remove the porosity and achieve high strength. In this case, the use of nano-particles is desirable to facilitate sintering and also to decrease the minimum feature size and surface roughness. Figure 2 shows a sintered gear wheel of μ-molded 316L nano-powder that has 15μm teeth. Tensile test specimens of the same material processed the same way have a UTS of >900 MPa, much higher than usual for 316L SS, with 12% elongation. Because ~15 to 25% linear shrinkage takes place during sintering, the molds must be designed oversized and specific for a given material. The shape distortion caused during sintering was measured on these SS gears to be quite low, ~3 μm.

To make the μ-molding process faster and cheaper, we, collaborating with Sandia CA researchers, have developed replicated molds that are either PMMA injection molded from LIGA-made masters (Figure 3) or silicone rubber cast on LIGA-made masters. These allow the high aspect ratio, vertical sidewalls and high dimensional tolerance of x-ray lithography at much lower cost. An yttria-stabilized zirconia ceramic part made using a replicated PMMA mold is shown in Figure 4.

Significance: The μ-molding process has been demonstrated to be capable of producing μ-components with features in the 10 μm range out of a wide range of materials with impressive dimensional tolerance, excellent mechanical properties and with low cost. These results allow component designers more freedom in designing new components and opens up more possibilities for the commercial mass-production of μ-systems.

Contact: Terry Garino, Ceramic Materials Dept., 1843
Phone: (505) 845-8762
Fax: (505) 844-9781
Email: tjgarin@sandia.gov

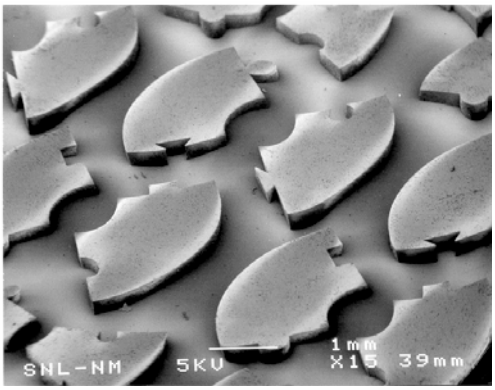

Figure 1. Micro-molded bonded NdFeB permanent magnets.

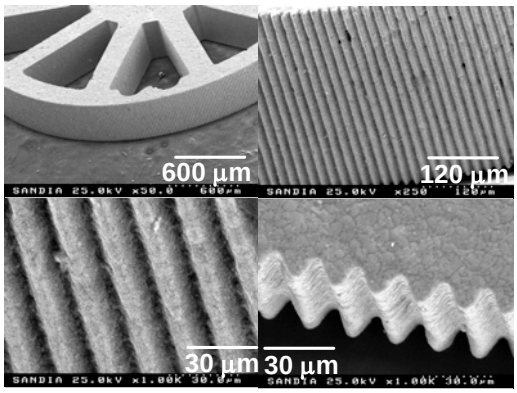

Figure 2. A micro-molded sintered 316L stainless steel gear with 15 micron teeth.

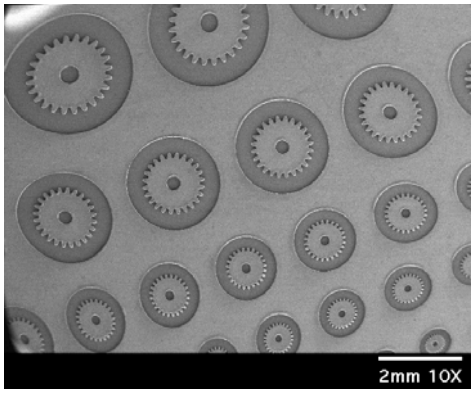

Figure 3. An injection molded PMMA replicated micro-mold.

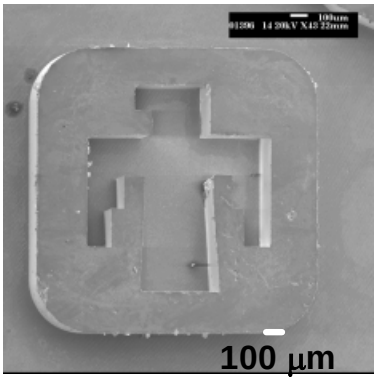

Figure 4. A sintered, micro-molded YSZ part.

Utilizing Robocasting for Advanced Manufacturing and Precision Printing

J. Cesarano, J. Stuecker, H. Denham, D. Sankel

Motivation: Freeform Fabrication is the near-net-shape processing of materials by sequentially stacking thin layers. The operation is computer controlled and requires no mold. This exciting new field of technology provides engineers with the ability to rapidly produce prototype parts directly from CAD drawings. Techniques for freeform fabrication with plastics and metals are quite advanced and include stereolithography, fused deposition modeling, LENS, etc. However, freeform fabrication of ceramics and multimaterial components is not well developed.

The motivation for this work is to develop a binderless freeform fabrication technique that is capable of building ceramic and multimaterial components that are unique in their structure can not be made with traditional methods, and yield improved performance.

Accomplishment: A manufacturing tool, called robocasting, has been developed at Sandia National Laboratories. Robocasting is a solid freeform fabrication technique, for fine particles, that uses computer controlled layer-wise extrusion of colloidal slurries. A robot precisely controls the deposition of pastes while printing (or "drawing") in 3-D. The result is analogous to automated cake icing and extremely complicated structures may be built that contain internal hidden features. Because the deposition orifice may be less than 50 microns, the robocaster may also be used as a precision printing apparatus. Some of the materials already demonstrated include ceramics, metals, electronic inks and functionally graded composites.

Successful robocasting relies upon the development of pastes that contain high concentrations of solid particles and exhibit a plastic consistency suitable for extrusion. Particle sizes are typically 0.1 to 5 μm and the paste particle content ranges between 40 and 60 volume percent solids, depending on the particle size distribution and morphology. The liquid carrier is usually water. Manipulation of the colloidal interparticle forces provides a means to control the paste rheology. This is accomplished with minor additions of dispersants and chemical modifiers. With a suitable yield stress built into the paste, self-supporting lattice structures may be directly fabricated with out the aid of a support material. Examples of these lattices are shown in Figures 1-3. The "layer by layer" robocasting process provides the means to build these lattices. It's difficult to imagine how traditional manufacturing techniques could be used to build such a structure. With the incorporation of in-situ laser profilometry it is now possible to build structures or print patterns conformally on non-planar substrates. The data from the profilometer is used to modify hardware instructions (see Figure 3).

Significance: The Robocasting technique has evolved into a versatile manufacturing tool that enables freeform fabrication of three-dimensional components and/or precise conformal printing

Robocasting technology is the basis for the development of catalyst supports with enhanced reaction efficiency (see Figure 1). A bio-medical application for customized fabrication of bone implants is also being developed. Figure 2 shows an implant that was made to fit into a patient with a deteriorated mandible. A human patient was temporarily fitted with the implant in a case study completed with the University of Illinois and Carle hospital.

Additionally, robocasting may be able to play a role in defense applications and remote battlefield manufacturing. With this tool designers may have unforeseen versatility to build components with unique structure and functionality.

Contact: Joe Cesarano, Ceramic Materials Dept., 1843
Phone: (505) 272-7624
Fax: (505) 272-7336
Email: jcesara@sandia.gov

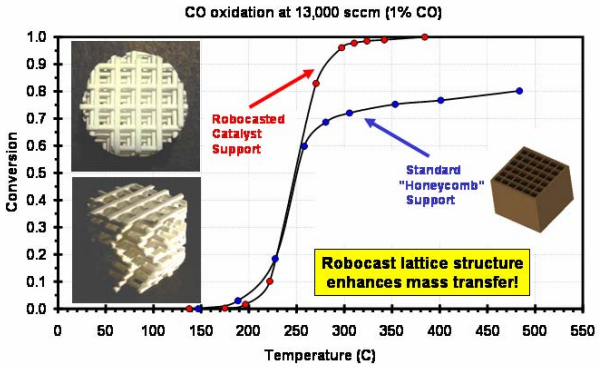

Figure 1. Robocasted lattices used as catalyst supports enhance the catalytic oxidation of carbon monoxide when compared to the traditionally used honeycomb supports.

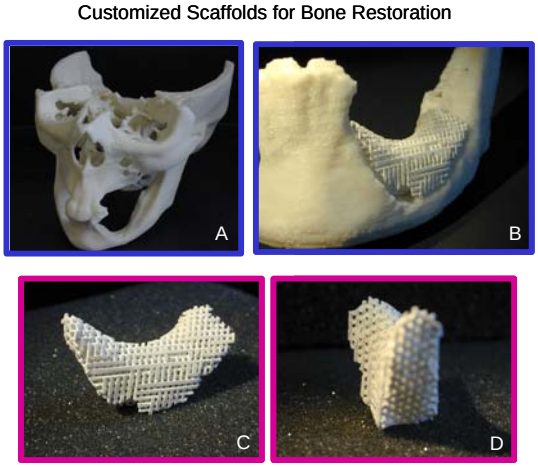

Figure 2. Robocasted lattices of hydroxyapatite can be fashioned into bone scaffolds that are customized for a particular patient. A) Replica of a patient's skull showing the deterioration of the mandible (i.e., jawbone). B) The customized scaffold (including a clearance groove for a nerve) fits nicely into the damaged mandible. C&D) Two views of the scaffold showing the intricate porous structure that promotes the in-growth of natural bone.

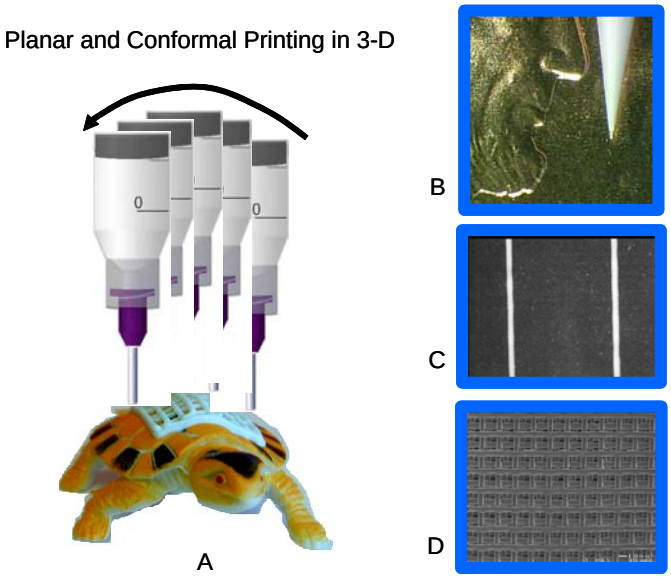

Figure 3. A) A schematic showing how conformal robocasting may be used to build a structure in 3-D onto a non-planar substrate. B) Precision printing may be accomplished with a 50-micron orifice shown in relation to Lincoln's nose on a penny. C) 60-micron lines deposited on a planar substrate. D) A three-dimensional lattice robocasted with 60-micron struts.

DISTRIBUTION

	MS&T External Advisory Panel: 1 copy each				
	Dr. William A. Baeslack III Dean, School of Engineering Jonsson Engineering Center – 3004 Rensselaer Polytechnic Institute 110 Eighth St. Troy, NY 12180-3590			Dr. David J. Bishop Vice President of Nanotechnology Bell Laboratories Lucent Technologies 700 Mountain Ave. – Rm 1A-264 Murray Hill, NJ 07974	
	Dr. Thomas Zacharia Oak Ridge National Laboratory PO Box 2008 MS-6163 Oak Ridge, TN 37831-6163			Dr. Alan Taub, Executive Director – Science General Motors R&D Center 30500 Mound Rd. MC 480-106-EX1 Warren, MI 48090-9055	
	Dr. Steven Wax, Deputy Director Defense Sciences Office DARPA/DSO 3701 N. Fairfax Dr. Arlington, VA 22203-1714			Professor John H. Weaver, Department Head Materials Science & Engineering University of Illinois 1304 W. Green Urbana, IL 61801	
	Dr. Harry Saxton 11257 Golden Chestnut Place Las Vegas, NV 89135				
1	MS 0102	J. Woodard, 2	1	MS 0130	J. Polito, 2800
1	MS 0513	J. P. Vandevender, 1000	1	MS 9005	R. G. Miller, 2820
1	MS 0323	H. Westrich, 1011	1	MS 0469	L. Shephard, 2900
1	MS 0511	D. Dimos, 1020	1	MS 0186	D. Blanton, 3000
1	MS 1427	J. Phillips, 1100	1	MS 0143	R. Detry, 4000
1	MS 0121	C. Hart, 1200	1	MS 1231	A. D. Romig, 5000
1	MS 0185	D. Goldheim, 1300	1	MS 1202	A. Campbell, 5900
1	MS 1190	J. Quintenz, 1600	1	MS 0724	R. Eagan, 6000
1	MS 1079	M. Scott, 1700	1	MS 0701	P. Davies, 6100
5	MS 0887	M. Cieslak, 1800	1	MS 0918	M. Jones, 7000
5	MS 0885	D. Salzbrenner, 1801	1	MS 9405	J. Hruby, 8700
5	MS 0885	G. Heffelfinger, 1802	1	MS 8750	G. Kubiak, 8750
20	MS 0885	C. Porter	1	MS 9161	W. Even, 8760
2	MS 0888	R. Clough, 1811	1	MS 9405	K. Wilson, 8770
2	MS 0886	N. Jackson, 1812	1	MS 0151	T. Hunter, 9000
2	MS 0886	R. Goehner, 1822	1	MS 0134	J. Rice, 9700
2	MS 0889	J. Braithwaite, 1832	1	MS 0139	M. Vahle, 9900
2	MS 0889	M. F. Smith, 1833	1	MS 0139	P. Wilson, 9902
2	MS 1411	H. E. Fang, 1834	1	MS -112	F. Figueroa, 10000
2	MS 1349	W. Hammetter, 1843	1	MS 0132	J. Martinez, 14000
2	MS 1411	J. Liu, 1846	1	MS 0960	G. Herrera, 14100
2	MS 0889	J. Custer, 1851	1	MS 0868	K. McCaughey, 14400
1	MS 0865	D. Cook, 1900	1	MS 1221	J. Tegnelia, 15000
1	MS 0457	J. Stichman, 2000			
1	MS 0429	J. Rottler, 2100			
1	MS 0437	C. Knapp, 2120			
1	MS 0509	M. Callahan, 2300			
1	MS 0503	D. Plummer, 2330			
1	MS 512	T. Blejwas, 2500			
1	MS 0521	W. Cieslak, 2501	1	MS9018	Central Technical Files, 8945-1
1	MS 0507	B. Walker, 2600	2	MS0899	Technical Library, 9616